Unveiling wide-orbit companions to K-type stars in Sco-Cen with Gaia EDR3

Bohn, A.J.; Ginski, C.; Kenworthy, M.A.; Mamajek, E.E.; Meshkat, T.; Pecaut, M.J.; ... ; Ségransan, D.

Astronomy & Astrophysics manuscript no. ajbohn_gaia_wide_orbit_companions
September 21, 2021

Unveiling wide-orbit companions to K-type stars in Sco-Cen with *Gaia* EDR3⋆

Alexander J. Bohn[1], Christian Ginski[2], Matthew A. Kenworthy[1], Eric E. Mamajek[3,4], Tiffany Meshkat[5], Mark J. Pecaut[6], Maddalena Reggiani[7], Christopher R. Seay[1], Anthony G. A. Brown[1], Gabriele Cugno[8], Thomas Henning[9], Ralf Launhardt[9], Andreas Quirrenbach[10], Emily L. Rickman[11,12], and Damien Ségransan[11]

(Affiliations can be found after the references)

Received November 15, 2020 / Accepted <date>

ABSTRACT

Context. Detection of low-mass companions to stellar hosts is important to test formation scenarios of these systems. Companions at wide separations are particularly intriguing objects as they are easily accessible for variability studies of rotational dynamics and cloud coverage of these brown dwarfs or planetary-mass objects.

Aims. We aim to identify new low-mass companions to young stars using the astrometric measurements provided by the *Gaia* space mission. When possible, high-contrast imaging data collected with VLT/SPHERE is used for confirmation.

Methods. We identify companion candidates from a sample of K-type, pre-main sequence stars in the Scorpius Centaurus association using the early version of the third data release of the *Gaia* space mission. Based on the provided positions, proper motions, and magnitudes, we identify all objects within a predefined radius whose differential proper motions are consistent with a gravitationally bound system. As the ages of our systems are known, we derive companion masses through comparison with evolutionary tracks. For seven identified companion candidates we use additional data collected with VLT/SPHERE and VLT/NACO to assess the accuracy of the properties of the companions based on *Gaia* photometry alone.

Results. We identify 110 comoving companions that have a companionship likelihood of more than 95%. Further color-magnitude analysis confirms their Sco-Cen membership. We identify ten especially intriguing companions that have masses in the brown dwarf regime down to 20 $M_{\rm Jup}$. Our high-contrast imaging data confirm both astrometry and photometric masses derived from *Gaia* alone. We discover a new brown dwarf companion, TYC 8252-533-1 B, with a projected separation of approximately 570 au from its Sun-like primary. It is likely to be located outside the debris disk around its primary star and SED modeling of *Gaia*, SPHERE, and NACO photometry provides a companion mass of 52^{+17}_{-11} $M_{\rm Jup}$.

Conclusions. We show that the *Gaia* database can identify low-mass companions at wide separations from their host stars. For K-type Sco-Cen members *Gaia* can detect sub-stellar objects at projected separations larger than 300 au and is sensitivity limited beyond 1,000 au with a lower mass limit down to 20 $M_{\rm Jup}$. A similar analysis of other star-forming regions could significantly enlarge the sample size of such objects and test formation and evolution theories of planetary systems.

Key words. binaries — brown dwarfs — astrometry — open clusters and associations: individual: Sco-Cen — stars: individual: TYC 8252-533-1

1. Introduction

Whereas direct, adaptive optics (AO)-assisted imaging is the best tool to detect and characterize faint companions close to the diffraction limits of current 10 m-class telescopes, these instruments usually cannot identify comoving objects at separations that are larger than several arcseconds. The Gemini Planet Imager (GPI; Macintosh et al. 2014) and the Spectro-Polarimetric High-contrast Exoplanet REsearch instrument (SPHERE; Beuzit et al. 2019) has a field of view with a radial extent of approximately 1.″4 and 5.″5 with respect to the primary star. Even though several remarkable discoveries have been made with these instruments (e.g., Macintosh et al. 2015; Chauvin et al. 2017; Keppler et al. 2018), it is reasonable to assume that a non-negligible fraction of wide-orbit companions remain undiscovered as they are located outside the field of view of the respective detectors.

Studying this unexplored population of wide-orbit objects is crucial for obtaining a complete census of the occurrence rates of sub-stellar companions. Dynamical and spectroscopic monitoring of these companions will help significantly in understanding the underlying formation mechanisms and test the efficiency of several proposed formation channels. Due to the low amount of flux contamination from the primary star, spectroscopic analysis of these widely separated companions is relatively easy and can be conducted with non-AO instruments. Constraining elemental abundances of the atmospheres and comparison to the stellar properties provides important clues as to whether the companion has formed in situ (e.g., Kroupa 2001; Chabrier 2003), inside a protoplanetary disk closer to the star (e.g., Pollack et al. 1996; Boss 1997), or was even captured (e.g., Kouwenhoven et al. 2010; Malmberg et al. 2011). Even transiting exomoons could be detected around these low-mass companions by monitoring their light curves.

Due to limits of the field of view of high-contrast imagers, comoving objects at these larger separations need to be identified using other techniques. The *Gaia* mission (Gaia Collaboration et al. 2016) of the European Space Agency and especially its early version of the third data release (*Gaia* EDR3; Gaia Collaboration et al. 2021) are best suited to identify this population of low-mass companions at wide orbital separations. Future data

⋆ Based on observations collected at the European Organisation for Astronomical Research in the Southern Hemisphere under ESO programs 099.C-0698(A), 0101.C-0341(A), 1101.C-0092(E), and 0104.C-0265(A).

releases of the *Gaia* mission might even provide partial orbital solutions for some of the identified companions.

In Sect. 2 of this article we describe how we use *Gaia* EDR3 to search for comoving objects at wide separations and in to K-type stars in the Scorpius-Centaurus association (Sco-Cen; de Zeeuw et al. 1999). Sco-Cen is composed of the three subgroups Upper Scorpius (US), Upper Centaurus-Lupus (UCL), and Lower Centaurus Crux (LCC) with mean distances of 145 pc, 140 pc, and 118 pc, respectively (de Zeeuw et al. 1999). Its youth – with average ages of 10 Myr, 16 Myr, and 15 Myr for the US, UCL, and LCC subgroups respectively (Pecaut & Mamajek 2016) – and its proximity made this association subject to several studies for young, directly imaged exoplanets (Rameau et al. 2013; Chauvin et al. 2017; Keppler et al. 2018; Haffert et al. 2019). The solar-type stars that are observed within the Young Suns Exoplanet Survey (YSES; Bohn et al. 2020a) constitute a subsample of the larger selection of K-type Sco-Cen members, which is studied in this article. We further analyze this sample of preselected companion candidates, derive object masses and companionship probabilities in Sect. 3. In Sect. 4 we present the results from complementary imaging data that were collected for seven of our preselected candidate companions. These data can be used to assess the quality of our strictly *Gaia*-based results. Lastly, we discuss our findings in Sect. 5 and present our conclusions and further implications of this work in Sect. 6.

2. Data and methods

We introduce the sample of K-type pre-main sequence stars that is objective to our analysis in Sect. 2.1 and we reassess their membership status in light of *Gaia* EDR3 astrometric measurements. The selection algorithm that we apply to identify comoving companion candidates to the stars of our sample in the *Gaia* catalogue is presented in Sect. 2.2. As several of the companion candidates were also imaged within the scope of YSES, we have additional near infrared imaging data to assess the properties of these companions. Our high-contrast observations and data reduction methods are described in Sect. 2.3.

2.1. Sample selection

Our analyses are based on a sample of 493 K-type pre-main sequence stars located in Sco-Cen.[1] The subsample of solar-type stars ($0.8\,M_\odot < M < 1.2\,M_\odot$) in the LCC sub-group of Sco-Cen is used within YSES to search for planetary-mass companions. These targets and their selection are extensively described in Pecaut & Mamajek (2016). As their criteria for Sco-Cen membership are amongst other parameters based on kinematically constrained parallaxes, we assessed if the trigonometric *Gaia* parallaxes confirm the membership status of these stars. We applied the same thresholds for Sco-Cen membership as presented in de Zeeuw et al. (1999) and Pecaut & Mamajek (2016), which are given by $4\,\mathrm{mas} < \varpi < 20\,\mathrm{mas}$, $\mu < 55\,\mathrm{mas\,yr^{-1}}$, $\mu_{\alpha*} < 10\,\mathrm{mas\,yr^{-1}}$, $\mu_\delta < 30\,\mathrm{mas\,yr^{-1}}$. This analysis indicated that only ten targets (2.0%) from the initial catalog do not comply with these astrometric requirements for Sco-Cen membership (see Table 1). Whilst this hypothesis needs to be confirmed by further measurements, we removed the corresponding targets from the full sample for the scope of this work. Furthermore, no astrometric measurements were available in the *Gaia* database for 24 additional stars from the initial catalogue (see Table 1). As our identification of comoving companion candidates relies on precise astrometric measurements for all stars from the input sample, we discarded these insufficiently characterized objects as well. The final input catalogue of stars used in this study is comprised of 459 K-type Sco-Cen members. The positions and distances of these targets are visualized in Fig. 1.

[1] Compiled from Table 7 of Pecaut & Mamajek (2016).

Table 1. Targets that were excluded from our analysis.

2MASS ID	Reason
11143442-4418240	$\varpi = (1.94 \pm 0.01)$ mas < 4 mas
11472064-4953042	No astrometric measurements
12063292-4247508	$\mu = (56.5 \pm 0.1)\,\mathrm{mas\,yr^{-1}} > 55\,\mathrm{mas\,yr^{-1}}$
12124890-6230317	No astrometric measurements
12253370-7227480	No astrometric measurements
13010856-5901533	No astrometric measurements
13032904-4723160	No astrometric measurements
13405585-4244505	No astrometric measurements
15151856-4146354	$\sigma_\varpi = 0.55$ mas > 0.50 mas
15250358-3604455	$\sigma_\varpi = 0.57$ mas > 0.50 mas
15272286-3604087	No astrometric measurements
15280322-2600034	$\varpi = (1.76 \pm 0.06)$ mas < 4 mas
15364094-2923574[a]	Optical triple
15374917-1840449	$\varpi = (0.76 \pm 0.03)$ mas < 4 mas
15455225-4222163	No astrometric measurements
15463111-5216580	No astrometric measurements
15494499-3925089	No astrometric measurements
15550624-2521102	No astrometric measurements
15564402-4242301	No astrometric measurements
16003134-2027050	No astrometric measurements
16015149-2445249	No astrometric measurements
16021045-2241280	No astrometric measurements
16025243-2402226	$\varpi = (0.82 \pm 0.02)$ mas < 4 mas
16025396-2022480	No astrometric measurements
16034536-4355492	No astrometric measurements
16062196-1928445	No astrometric measurements
16070356-2036264	No astrometric measurements
16120140-3840276	No astrometric measurements
16131738-2922198	No astrometric measurements
16141107-2305362	$\varpi = (0.50 \pm 0.11)$ mas < 4 mas
16195068-2154355	No astrometric measurements
16240632-2456468	No astrometric measurements
16271951-2441403	No astrometric measurements
16384946-2735294	$\varpi = (3.73 \pm 0.72)$ mas < 4 mas

Notes. The targets in the table were excluded from the analysis, either because these are not consistent with Sco-Cen membership according to the criteria listed in de Zeeuw et al. (1999) and Pecaut & Mamajek (2016) or the *Gaia* database contained insufficient or uncertain astrometric information. [(a)] 2MASS J15364094-2923574 is resolved by *Gaia* into an optical triple, comprised of a foreground ($\varpi \simeq 16$ mas), high proper motion, physical binary (Gaia EDR3 6209195913018942976 & Gaia EDR3 6209195913018942720) and a third background interloper (Gaia EDR3 6209195913015396608).

2.2. preselection of companion candidates in Gaia EDR3

Our preliminary companionship assessment is based on the data products provided by *Gaia* EDR3. We corrected the parallax measurements for the zero point bias as discussed in Lindegren

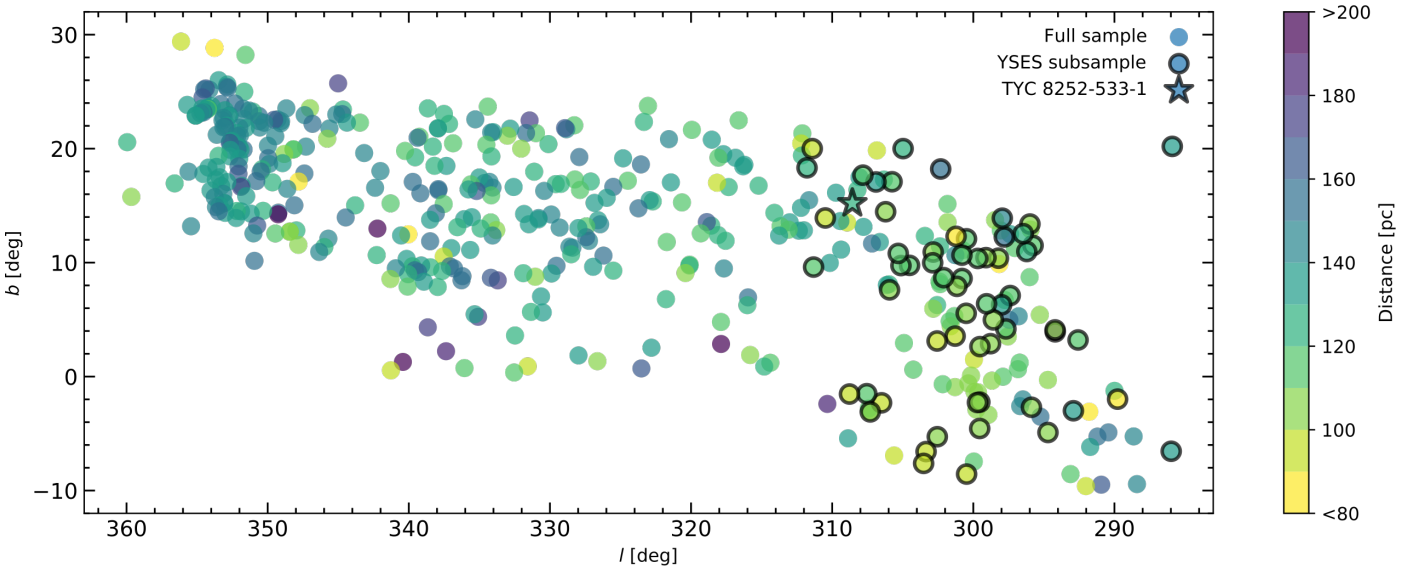

Fig. 1. Input sample of K-type pre-main sequence stars in Sco-Cen. We show the sky positions of the targets in galactic coordinates and the color of the markers indicates the distance to the objects. Members of the YSES subsample are highlighted by the black outlines around the markers. The star highlights TYC 8252-533-1, whose brown dwarf companion is analyzed in Sect. 4.1.

et al. (2021a)[2] and performed the correction of the G band magnitudes of sources with 6-parameter astrometric solutions as described by Riello et al. (2021).[3] We compiled a first list of potential companions in four steps. For each target from our input catalogue

1. we found all targets within a projected physical separation of $\rho_{\rm cutoff} = 10\,000$ au,
2. we dismissed data without any parallax measurements or a measurement with an uncertainty larger than 0.5 mas,
3. we checked for the remaining objects, if the parallaxes deviated by less than 20% from that of the host,
4. and we required the proper motions in right ascension and declination to be consistent within a 10 km s^{-1} interval.

Similar selection methods are used by Fontanive et al. (2019), Fontanive & Bardalez Gagliuffi (2021), and within the scope of the COol Companions ON Ultrawide orbiTS (COCONUTS; Zhang et al. 2020, 2021) program. A detailed discussion of these preselection criteria can be found in Sect. 5.1. As we are predominantly interested in the identification of sub-stellar companions, we do not require a radial velocity (RV) measurement, since brown dwarf members of Sco-Cen are too distant and thus too faint to allow an RV measurement in the *Gaia* database. The radial velocity measurements reported in *Gaia* EDR3 are not newly derived for this catalogue, but adopted from the second data release of the *Gaia* mission (Gaia DR2; Gaia Collaboration et al. 2018), for which an average limiting magnitude to facilitate RV measurements of ∼13 mag is reported (Cropper et al. 2018).

After applying the four selection criteria as described before, we identified 172 companion candidates to 148 stars of our sample (for a detailed list see Table B.1 in Appendix B) within a cutoff separation of 10,000 au. When studying the list of identified companion candidates we realized that twelve of the identified companion candidates were part of the input catalog. These six pairs of potential stellar multiples that were directly obtained from the list of K-type Sco-Cen members in Pecaut & Mamajek (2016) are listed in Table 2. Three of these candidate multiple systems from the input catalog even host a third potential companion that was identified by our preselection for both of the respective Sco-Cen K-type stars: these are Gaia EDR3 5863747462890662144, Gaia EDR3 6208136396122878976, and Gaia EDR3 6037784004457597568 that are preselected as candidate companions to the potential stellar multiples composed of Gaia EDR3 5863747467220735744 (2MASS J13335329-6536473) and Gaia EDR3 5863747467220738432 (2MASS J13335481-6536414), Gaia EDR3 6208136391829015936 (2MASS J15241147-3030582) and Gaia EDR3 6208136396126956928 (2MASS J15241303-3030572), and Gaia EDR3

Table 2. Duplications amongst our list of preselected candidate companions.

2MASS ID	*Gaia* EDR3 ID
13335329-6536473	5863747467220735744
13335481-6536414	5863747467220738432
15241147-3030582	6208136391829015936
15241303-3030572	6208136396126956928
16023814-2541389	6235806323497438592
16023910-2542078	6235806259081172736
16123916-1859284	6245821092014031616
16124051-1859282	6245821126373768832
16265700-3032232	6037784004457590528
16265763-3032279	6037784008760031872
16320058-2530287	6045791575844270208
16320160-2530253	6045791953801392128

Notes. We show targets that were both listed in the input catalog and the full selection of candidate companions presented in Appendix B. The horizontal lines separate individual pairs of potential candidate companions.

[2] The applied correction formula for the parallactic zero point bias is available at https://gitlab.com/icc-ub/public/gaiadr3_zeropoint.

[3] The applied correction formula for the G band magnitudes is available at https://github.com/agabrown/gaiaedr3-6p-gband-correction.

Table 3. Candidate triple systems to K-type stars in Sco-Cen. The list originates from our preselected candidates companions presented in Appendix B.

Primary		Secondary		Tertiary	
2MASS ID	*Gaia* EDR3 ID	2MASS ID	*Gaia* EDR3 ID	2MASS ID	*Gaia* EDR3 ID
11554295-5637314	5343603288120259072	-	5343603288130858112	-	5343603180734334592
12094184-5854450	6071087597518919040	-	6071087597518919808	-	6071087597497876480
12123577-5520273	6075815841096386816	-	6075816592695096576	-	6075816596995760640
12474824-5431308	6073980172067600640	-	6073980240787079680	-	6073980172067600000
13071310-5952108	6056115131031531264	-	6056115135337482496	-	6056115169731484288
13335481-6536414	5863674467220738432	13335329-6536473	5863674467220735744	-	5863674462890662144
13540743-6733449	5850443307764629376	-	5850443303440130816	-	5850443303446183040
15113968-3248560	6207460471351260160	-	6207460436991521280	-	6207460471351260928
-	6200310514738629504	15171083-3434194	6200310519037175040	-	6200310484677437184
15241147-3030582	6208136391829015936	15241303-3030572	6208136396126956928	-	6208136396122878976
15370214-3136398	6208381582919629568	-	6208381587215253504	-	6208381587220236160
15451286-3417305	6014696841553696768	-	6014696841553696896	-	6014696875913435520
16065795-2743094	6042124910722287744	-	6042124915024285440	-	6042124807643059968
16085427-3906057	5997035351934438784	-	5997035317574700544	-	5997035416337166976
16114387-2526350	6049537165279381632	-	6049532737170518016	-	6049537169580902272
16135801-3618133	6022499010422921088	-	6022499006128860928	-	6022499010440068864
16161423-2643148	6042418858284146688	-	6042418862581174016	-	6042418828224074752
16204468-2431384	6049266036882633856	-	6049266002522895232	-	6049266414839756416
-	6024816059387932416	-	6024816020718366464	16235484-3312370	6024816025017339392
16265763-3032279	6037784008760031872	16265700-3032232	6037784004457590528	-	037784004457597568
16345314-2518167	6047289699098449920	-	6047289699098450944	-	6047289733458188032

Notes. The targets are classified as potential primary, secondary or tertiary of the system by increasing G band magnitudes. Only for targets from our input catalog we list the corresponding 2MASS identifiers.

6037784004457590528 (2MASS J16265700-3032232) and Gaia EDR3 6037784008760031872 (2MASS J16265763-3032279), respectively. After removing these duplicates from our list of preselected companions, 163 potential companions to 142 Sco-Cen members remained.[4]

Amongst these newly identified candidate binary systems we found 21 potential systems of even higher multiplicity. In addition to the three previously mentioned candidate triples comprising two stars from our input catalog each, we found 18 further targets that were associated with two individual candidate companions according to our preselection. All of these potential triple systems are listed in Table 3.

In addition, we identify HD 98363 (2MASS J11175813-6402333, Gaia EDR3 5240643988513309952) among this sample of preselected candidate companions. Bohn et al. (2019) showed that HD 98363 is the 1.9 $M_{\odot}$ primary to the solar-mass star Wray 15-788 (2MASSJ11175186-6402056, Gaia EDR3 5240643988513310592) from our target stars. This demonstrates that the input stars of the algorithm do not necessarily have to be the primary of the system, as the detected companions can be equal or even higher mass. Furthermore, we identify seven candidate companions that were also observed with SPHERE as part of YSES. The identifiers of all primary stars with companion candidates from our preselection that have been imaged within the scope of YSES are listed in Table 4. A detailed analysis of these objects that combines *Gaia* and high-contrast imaging data is performed in Sect. 4.

[4] To report the full output of our algorithm, we did not remove these duplications from the table presented in Appendix B. All further analysis, however, is performed on the cleaned sample of 163 individual companion candidates.

Table 4. Candidate companion systems with complementary SPHERE data from YSES.

2MASS ID	*Gaia* EDR3 ID
12195938-5018404	6126648698878768384
12391404-5454469	6074374346993398144
12505143-5156353	6075310478057303936
12560830-6926539	5844909156504879360
13130714-4537438	6088027047281877120
13233587-4718467	6083750638577673088
13335481-6536414	5863674467220738432

The planetary-mass companions that Bohn et al. (2020a,b, 2021) detected for YSES 1 (TYC 8998-760-1, 2MASS J13251211-6456207, Gaia EDR3 5864061893213196032) and YSES 2 (TYC 8984-2245-1, 2MASS J11275535-6626046, Gaia EDR3 5236792880333011968), however, are not listed in the *Gaia* archive. This is explained by the large contrast of all three companions that are found at angular separations of less than 3.″5, which places them directly inside the red dashed exclusion zone highlighted in Fig. 3.

We further compared the astrometric and photometric properties of the targets from our input sample to the preselection of candidate companions. The parallaxes, proper motions, and magnitudes among both groups and their corresponding uncertainties are presented in Fig 2. The distributions of parallaxes and proper motions are very similar among our input sample and the detected candidate companions. We derive median parallaxes of $7.55^{+1.59}_{-0.90}$ mas and $7.68^{+1.39}_{-1.04}$ mas and proper motions of $32.06^{+6.90}_{-6.68}$ mas yr^{-1} and $31.83^{+6.15}_{-6.38}$ mas yr^{-1} for the former and

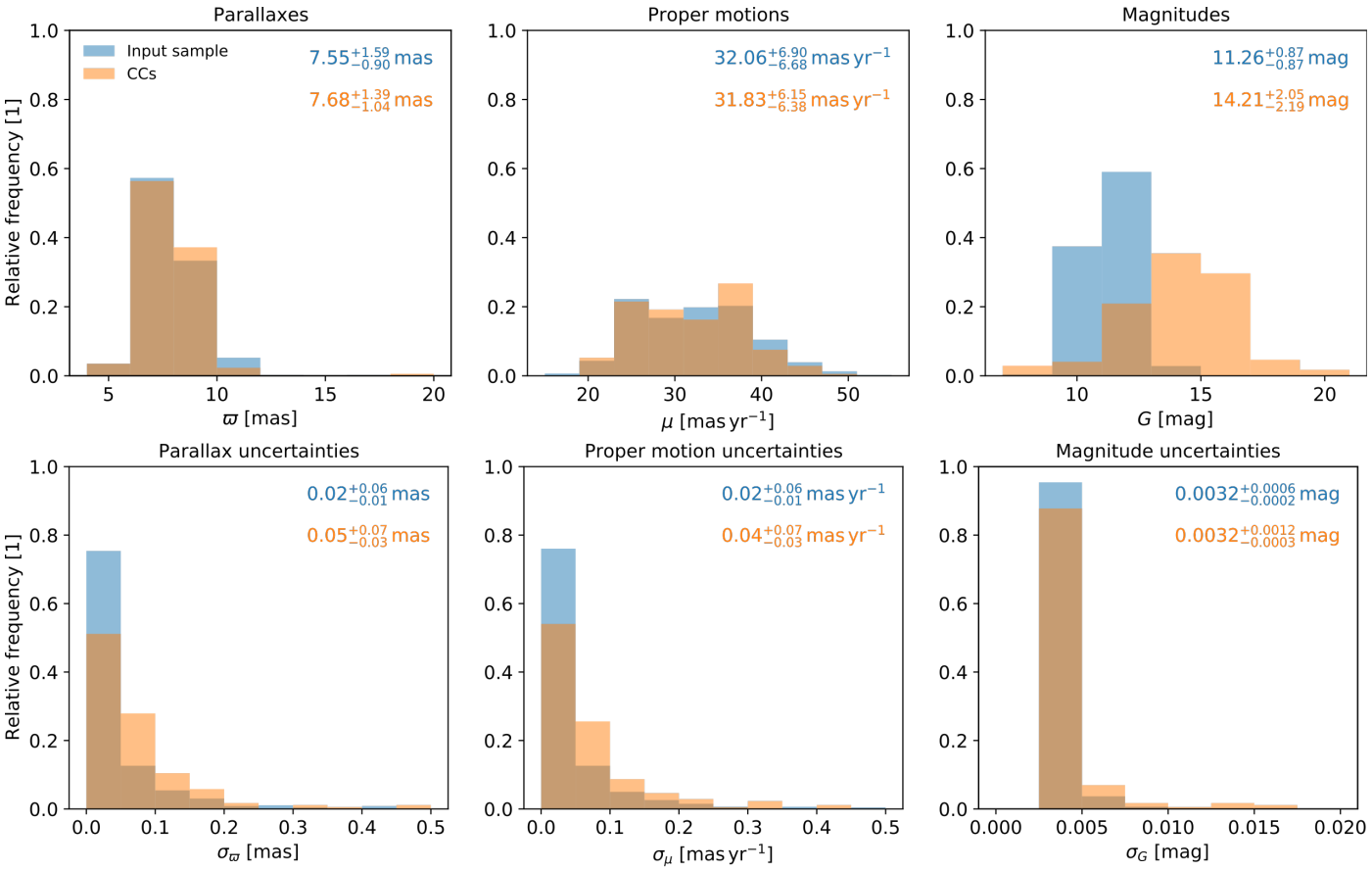

Fig. 2. Astrometric and photometric properties of the input sample and the preselected list of candidate companions (CCs). In the top panel we present the distributions of the object parallaxes, proper motions, and mangitudes from both samples. In the lower panel the uncertainties are shown. The colored values in the upper right of each panel indicate the median and the 68% confidence intervals of the associated distributions.

latter sample, respectively.[5] This is not surprising as our preselection criteria are supposed to identify objects with astrometric properties that are similar to those of the K-type Sco-Cen members from Pecaut & Mamajek (2016). The G band magnitude distributions of our input catalog and identified candidate companions are distinct, with median values of 11.26 ± 0.87 mag and $14.21^{+2.05}_{-2.19}$ mag, respectively. This is also expected, as the input catalog contains only stars of the same spectral type that are all members of the same association; hence no large range of the stellar magnitudes is covered by this sample. The companion candidates, however, exhibit fainter magnitudes that extend down to the *Gaia* limiting magnitude of $G \approx 21$ mag. Due to the fainter nature of our candidate companions, their astrometric uncertainties are on average larger by a factor of 2 than those of the stars from our input catalog (see bottom left and middle panel of Fig. 2). The median magnitude uncertainties among both samples are comparable though, yet there are a few objects with magnitude uncertainties as large as 0.02 mag in our candidate companion sample. These outliers are associated to the faintest targets from our preselection algorithm.

This preselected sample can be refined by comparing the differential projected velocity of a candidate companion to the maximum allowed speed for a gravitationally bound orbit based on the masses of both bodies and their separation. A detailed application of this refinement procedure is described in Sect. 3.4.

[5] The uncertainties represent the 68% confidence intervals of the distributions.

2.3. High-contrast imaging observations

Seven of our preselected companion candidates were also imaged with SPHERE as part of YSES. The identifiers of these systems are listed in Table 4. For a potential brown dwarf companion around TYC 8252-533-1 we collected additional data with NACO (Lenzen et al. 2003; Rousset et al. 2003) at ESO's Very Large Telescope. A detailed overview of all observations and the weather conditions is provided in Table A.1 in Appendix A. The reduction is detailed in Bohn et al. (2020a) with a custom processing pipeline that is based on version 0.8.1 of the `PynPoint` package (Stolker et al. 2019). As the companions are reasonably bright and widely separated from the star, we did not perform any PSF subtraction when evaluating their astrometry and photometry.

3. Gaia results and analysis

In this Section we analyze the results that were derived from our preselection described in Sect. 2.1. In Sect. 3.1 we show the object magnitudes of identified candidate companions as a function of angular separation with respect to the primary star. As we know the ages of all our targets, we can convert these flux measurements to mass estimates for the companion candidates. This analysis is detailed in Sect. 3.2. We further assess the colors of our candidate companions and evaluate whether these are consistent with the proposed Sco-Cen membership in Sect. 3.3. We analyze the relative motions of all identified objects and probe if these are in agreement with a gravitationally bound orbit around

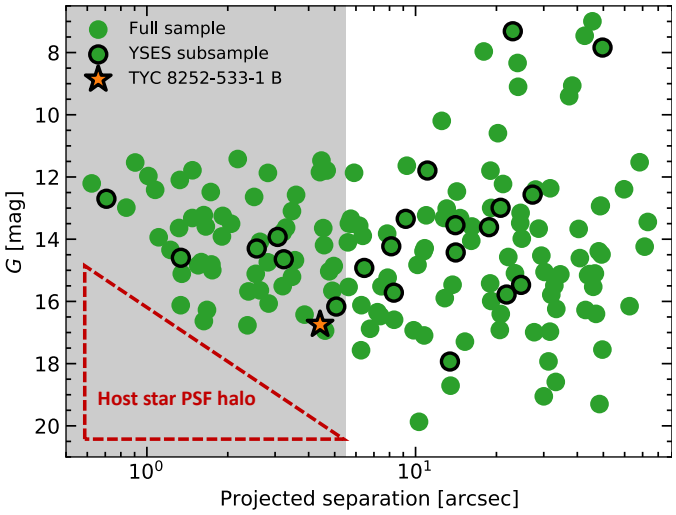

Fig. 3. Identified companion candidates to K-type Sco-Cen members. Members of the YSES subsample are highlighted by the black outline around the marker. The orange star highlights the brown dwarf companion TYC 8252-533-1 B that is analyzed in Sect. 4.1. The apparent *Gaia* G band magnitude is presented as a function of projected separation in arcseconds. Due to the PSF halo of the primary, the detectable magnitude threshold increases with larger separations from the host. This area of reduced sensitivity is indicated by the red, dashed triangle. The gray-shaded region represents the field of view of the SPHERE/IRDIS detector.

the primary star. This assessment is presented in Sect. 3.4. In Sect. 3.5 we present the properties of the candidates that exhibit the highest likelihoods to be bound companions.

3.1. Raw Gaia astrometry and photometry

In Fig. 3 we present the apparent G band magnitudes of the identified companion candidates as a function of projected separation. The detection sensitivity improves with increasing separation from the target, which can be attributed to the PSF halo of the host star. There is a clear exclusion zone (as indicated by the red, dashed triangle in Fig. 3) in which the presented technique is not able to detect any low mass comoving objects. This region is however highly complementary to the parameter space that is covered by the field of view of current generation of high-contrast imaging instruments. The gray-colored background of Fig. 3 shows the field of view of the SPHERE/IRDIS camera with a radial extent of $\leq 5\farcs5$. The seven companions that were observed within the scope of YSES are located in this part of the parameter space. For separations that are larger than approximately 10 arcseconds the *Gaia* contrast to the primary becomes background limited and we are sensitive to objects with an apparent G band magnitude down to 20 mag. This is in good agreement with the limiting magnitude of $G = 21$ mag that is required for objects to appear with a five-parameter astrometric solution in the EDR3 catalog (Gaia Collaboration et al. 2021).

3.2. Mass estimation

To characterize the identified companion candidates in further detail, we determined the absolute magnitudes of the objects using the parallax measurement provided by *Gaia* EDR3. In many cases, the parallaxes of the identified companion candidates have larger uncertainties than the parallax measurements of the stars from our input catalog, which have a median error of only 0.02 mas (see Fig. 2). We therefore used the latter parallax values to estimate the distances to the detected objects. Even though this requires true companionship between both objects, this estimate is a reasonable assumption as all candidate companions are Sco-Cen members according to the astrometric membership criteria from de Zeeuw et al. (1999) and Pecaut & Mamajek (2016) (see Sect. 2.1). As Pecaut & Mamajek (2016) provide age estimates[6] for all systems but one, we converted the absolute magnitudes of the companions to object masses by evaluation of BT-Settl models (Allard et al. 2012; Baraffe et al. 2015) at the corresponding system age. The remaining system without an age measurement, SZ 65 (2MASS J15392776-3446171, Gaia EDR3 6013399894569703040), is a member of the Lupus star forming region, so we assigned it an age of 2 Myr in accordance with the average age of this cloud complex (Comerón 2008; Alcalá et al. 2014). For all ages we assumed an uncertainty of 2 Myr with a youngest possible age of 1 Myr. The BT-Settl models we used are valid for objects with masses smaller than 1.2 $M_\odot$, which is equivalent to an apparent G band magnitude of approximately 11 mag at the average distance of Sco-Cen and at an age of 15 Myr. For the brightest objects from Fig. 3, which were outside the magnitude range supported by the BT-Settl models, we used MIST isochrones (Dotter 2016; Choi et al. 2016) to convert their G band photometry to a stellar mass. As the object masses strongly depend on the underlying system age and only a single photometric measurement is used for the derivation, we do not claim that the provided mass estimates are very precise, but instead indicate whether it is a brown dwarf or a stellar companion. The derived mass estimates for the companion candidates are listed in Table B.1 in Appendix B.

We present the companion masses as a function of projected physical separation in Fig. 4. The conversion from projected angular separations to projected physical separations was performed using the distance estimate based on the parallax measurement of the primary. We do not include the difference in *Gaia* parallaxes between primary and companion to determine a three-dimensional separation, as these measurements have typical errors of 0.02 mas and 0.05 mas for stars from our input catalog and companion candidates, respectively (see Fig. 2). For two average Sco-Cen members with parallaxes of 7.5 mas, Gaussian error propagation provides an uncertainty for the radial separation in the order of 1 pc or approximately 200,000 au. This uncertainty is much larger than our measured projected separations and would dominate the uncertainty of the derived parameter. We proceed using projected separations as a lower limit for the three-dimensional distances.

In Fig. 4 the region of limited sensitivity due to the PSF halo of the primary is still clearly visible and it implies that for separations closer than approximately 300 au we are only sensitive to stellar-mass companions. Farther away from the host, however, we can detect comoving brown dwarf companions with masses smaller than 80 $M_{\rm Jup}$. The lower mass threshold is reached for separations larger than approximately 1000 au and we are sensitive to objects masses as low as 20 $M_{\rm Jup}$. Exoplanets at Sco-Cen distance and age and with masses below the deuterium burning limit of approximately 13 $M_{\rm Jup}$ are thus marginally too faint to be confidently detected with *Gaia* EDR3.

[6] We note that these age estimates rely on pre-*Gaia* parallaxes that were derived kinematically and which might differ from the value reported in *Gaia* EDR3. A reassessment of these parameters – especially for the identified systems with low-mass companions – is advisable, but beyond the scope of this work.

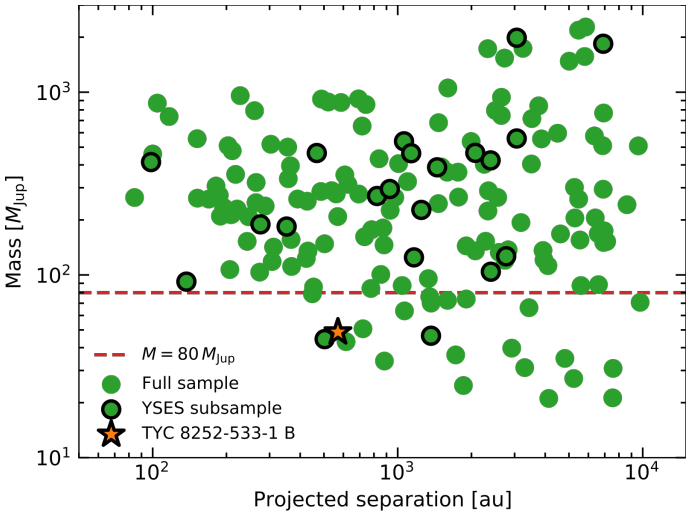

Fig. 4. Identified companion candidates to K-type Sco-Cen members II. Members of the YSES subsample are highlighted by the black outline around the marker. The orange star highlights TYC 8252-533-1 B analyzed in Sect. 4.1. The companion mass is presented as a function of projected separation in Astronomical Units. Mass conversion was performed by comparison to BT-Settl and MIST models evaluated at the system age. The dashed red line at 80 M_{Jup} indicates the threshold between brown dwarfs and stellar mass companions.

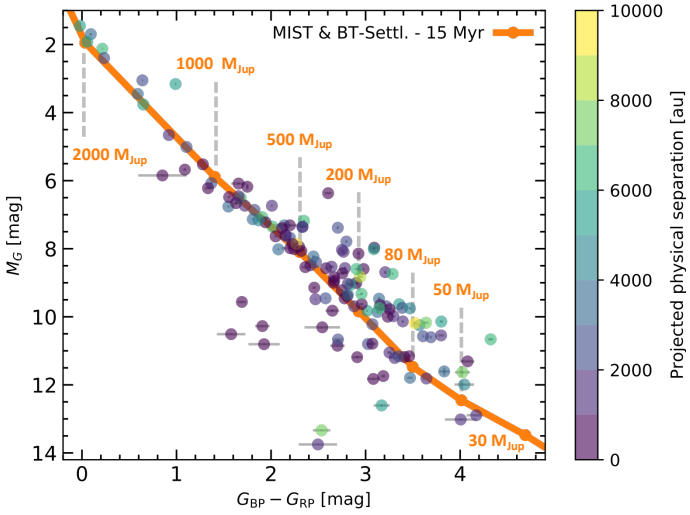

Fig. 5. Color-magnitude diagram of identified companion candidates to K-type stars in Sco-Cen. The colors of the markers indicate the projected separation between host and companion. The orange line represents a combination of MIST and BT-Settl isochrones for an age of 15 Myr.

3.3. Color-magnitude analysis

To confirm the young and (sub-)stellar nature of the detected objects, we evaluated all candidate companions in a color-magnitude diagram as presented in Fig. 5. The color is estimated using the *Gaia* filters for the blue (G_{BP}) and red part (G_{RP}) of the G band continuum. As visualized in Fig 5, most of the candidate companions have colors that are in very good agreement with synthetic MIST and BT-Settl models for young objects of 15 Myr, which is a reasonable average for the presented Sco-Cen sample (Pecaut & Mamajek 2016). This corroborates the Sco-Cen membership of the analyzed candidates and each of these is very likely to be a young member of the association, even if it turns out not to be a companion to any of the stars from our input catalog. There are two outliers at the faint end of the sequence that appear to be bluer than predicted by the evolutionary models. This is, however, not a contradiction with Sco-Cen membership of these objects. The corresponding objects, Gaia EDR3 5232514298301348864 and Gaia EDR3 5997035416337166976, are the faintest among our full sample of identified companion candidates with a G band magnitude of 19.9 mag and 19.3 mag, respectively. Their G_{BP} and G_{RP} photometric measurements exhibit a corrected flux excess factor C^* of 0.62 and 0.28, respectively, which is different from $C^* = 0$ that is associated with trustworthy photometry (Riello et al. 2021). This large uncertainty most likely originates from the faint G_{BP} flux of the objects, whose true value might be below *Gaia*'s sensitivity limits in this channel. Hence it is certainly possible that Gaia EDR3 5232514298301348864 and Gaia EDR3 5997035416337166976 are much redder than indicated in Fig. 5 and consistent with the colors that are predicted for a low-mass brown dwarf companion at Sco-Cen age. This conclusion is corroborated by the better-constrained $G - G_{RP}$ colors of both objects. These values of 1.5 mag and 1.3 mag are in good agreement with late M spectral types.

It should be noted that not all of our identified companion candidates have G_{BP} and G_{RP} flux measurements, as can be seen in Table B.1 in Appendix B. These 27 targets without any color information are not included in the plot shown in Fig. 5 and their photometric Sco-Cen membership compatibility thus cannot be assessed properly. For 23 of these insufficiently characterized companions the lack of precise color measurements is explained by their proximity and contrast with respect to the target star. All of these objects exhibit angular separations of less than 3″. The remaining four candidates without any color information are at larger separations from the target star, but in all cases these have an additional *Gaia* source of equal or higher brightness at very close separations (< 2″); these are most likely affecting the flux measurements. For Gaia EDR3 6022499010440068864 and Gaia EDR3 6208381587215253504 these close contaminants are members of the same candidate multiple systems that we have preselected.

3.4. Companionship assessment

We further analyzed whether the identified companion candidates are gravitationally bound multiple systems based on the available astrometric data. In the general description of the gravitational two-body problem, a system is considered bound when its total kinetic energy

$$T = \frac{\mu}{2}\left(\dot{r}^2 + r^2\dot{\phi}^2\right) \tag{1}$$

is smaller than the potential energy

$$V = \frac{1}{r}GM\mu\,, \tag{2}$$

of both bodies. In this formalism r denotes the separation of the two bodies; $\dot{r}$ and $\dot{\phi}$ are the radial and azimuthal velocities with respect to the center of mass. The sum of both individual object masses M_1 and M_2 is M and we define the reduced mass as

$$\mu = \frac{M_1 M_2}{M_1 + M_2} = \frac{M_1 M_2}{M}\,. \tag{3}$$

These conditions imply that a gravitationally bound system requires

$$\left(\dot{r}^2 + r^2\dot{\phi}^2\right) < \frac{2GM}{r}\,. \tag{4}$$

Even though we do not know the objects' true three-dimensional separations and differential velocities, equation (4) allows us to assess which systems cannot be bound. This is possible because our projected differential velocity $v_{\rm proj}$ is strictly smaller or equal to the amplitude of the true differential velocity $\sqrt{\dot{r}^2 + r^2\dot{\phi}^2}$. Likewise, the right-hand side of equation (4) is bounded above by substituting r in the expression with our measured projected separation $\rho \leq r$ as

$$\frac{2GM}{r} \leq \frac{2GM}{\rho} =: v_{\rm max}^2 \,, \tag{5}$$

where we defined this new expression as the maximum allowed differential velocity for a system to be bound.

Hence we evaluated the ratio of our measured projected velocity difference $v_{\rm proj}$ and $v_{\rm max}$ to assess which systems are most likely not bound as per

$$\frac{v_{\rm proj}}{v_{\rm max}} = v_{\rm proj}\sqrt{\frac{\rho}{2GM}} = \begin{cases} < 1 & \text{System can be gravitationally bound or} \\ \geq 1 & \text{System most likely not gravitationally bound.} \end{cases} \tag{6}$$

This expression is completely symmetric in M_1 and M_2, so within this formalism it does not matter which star is considered to be the primary of the system. Whereas a ratio greater than or equal to one is a good indicator that the studied system cannot be physically bound, a value smaller than unity does not necessarily indicate that the opposite scenario is true, due to the unknown contributions to separation and differential velocity along our line of sight. This metric is valid for regular binary systems but it is not suitable to assess systems with higher orders of multiplicity, such as the potential triple systems we have found around some of our targets. A proper treatment for these special cases, however, is not straightforward and will thus be neglected in our further analysis. The fraction of triple or higher-order multiple systems is assumed to be approximately 25 % among solar-type multiple systems (e.g., Mayor & Mazeh 1987; Eggleton & Tokovinin 2008; Duchêne & Kraus 2013). It is thus not surprising that we have identified 21 candidate triple systems out of 142 candidate multiples from our preselection. This smaller fraction of ≈15 % does not violate these statistical constraints as some triple systems will certainly be missed either due to the cutoff separation or additional components below the resolution limit of *Gaia*.

We calculated the differential proper motions between target and companion from the values listed in the *Gaia* EDR3 database (see Appendix B). To convert this angular movement to a differential projected velocity $v_{\rm proj}$ in km s^{-1} we used the inverted parallax of the star from our input catalog. For the derivation of $v_{\rm max}$ we adopted the mass measurements for the stars of our sample from Pecaut & Mamajek (2016). For SZ 65, which was missing this quantity in Pecaut & Mamajek (2016), we used a mass of 0.7 $M_\odot$ based on previous work by Alcalá et al. (2017). The masses of the identified companions were estimated as previously determined by *Gaia* photometry and for the objects that were heavier than the maximum valid mass from our BT-Settl models we used MIST isochrones to derive a stellar mass.

The resulting ratios of $v_{\rm proj}$ to $v_{\rm max}$ that we derived for all objects are listed in Table B.1 in Appendix B. The error budget in the calculation of these quantities is dominated by the uncertainty of the differential velocities of both objects. The uncertainties of $v_{\rm proj}/v_{\rm max}$ were propagated by a bootstrapping approach. We repeated the velocity calculation 10,000 times, drawing the initial proper motions of both objects from Gaussian distributions that are centered around the *Gaia* EDR3 values, and their corresponding uncertainties served as standard deviation for these initial normal distributions. The derived $v_{\rm proj}$ to $v_{\rm max}$ ratios represent the median of the corresponding posterior distribution and the surrounding 68% confidence interval as an estimate of the uncertainties. We visualize these derived parameters as a function of angular separation and companion mass in Fig. 6.

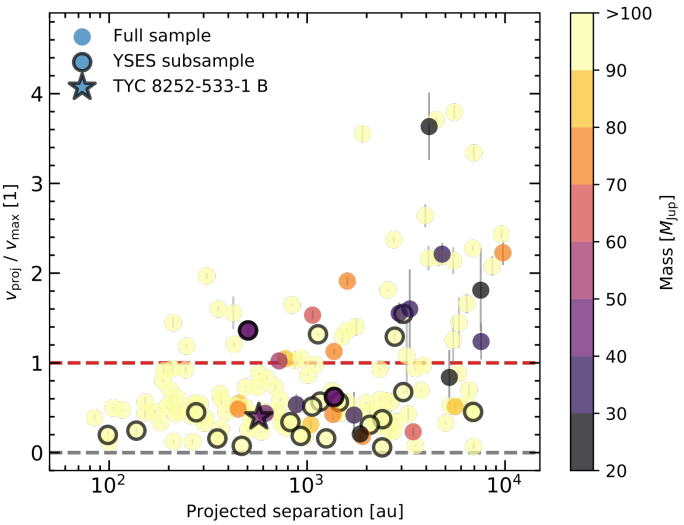

Fig. 6. Relative velocities of identified companions of a sample of K-type Sco-Cen members. We show the ratio of the differential projected velocities $v_{\rm proj}$ to the maximum velocity that allows a gravitationally bound system $v_{\rm max}$ as defined in equation (6). This parameter is a measure of whether our preselected candidate companions are part of a binary system; a value greater than unity renders this scenario as unlikely. These two different regimes are separated by the dashed red line. The colors of the markers indicate the mass of the corresponding candidate companion. To focus primarily on the sub-stellar objects in our sample the color bar is cut off at masses that are higher than 100 $M_{\rm Jup}$. Markers with a black outline refer to members of the YSES subsample and TYC 8252-533-1 B is highlighted by the star.

Most of the identified companion candidates are consistent with $v_{\rm proj}/v_{\rm max} < 1$, which indicates that for these objects a gravitationally bound orbit is not ruled out by *Gaia* EDR3 data. To quantify the likelihood of these objects to be a real companion to the target of our sample, we derive the probability of a $v_{\rm proj}$ to $v_{\rm max}$ ratio that is smaller than unity, based on our 10,000 samples for each posterior distribution. This value $p_{\rm dyn}^{\rm C}$ represents an upper limit for the dynamical companionship probability as the complete three dimensional astrometry of all objects is not available.

As this value does not account for comoving Sco-Cen members that might have similar projected velocities as a target from our input catalog despite not being gravitationally associated, we further derived a statistical companionship likelihood $p_{\rm stat}^{\rm C}$. For each companion candidate we checked how many sources were found by our preselection algorithm, when choosing a cutoff separation that is twenty times as large as the projected separation of the candidate (see e.g., Fontanive & Bardalez Gagliuffi 2021). This number provides an estimate of how many other Sco-Cen objects with similar parallaxes and proper motions are in the immediate surroundings of the stars from our input catalog. We obtained the adjusted number of objects, N_{20}, by counting the objects within the twenty times larger reference region while excluding the originally enclosed companion candidates. Based on this number we derived a statistical probability to have one of

these sources in the 400 times smaller search region. The statistical companionship likelihood is then calculated as

$$p^{\rm C}_{\rm stat} = 1 - \frac{N_{20}}{400} \, . \tag{7}$$

Our final companionship probability considers both these dynamical and statistical terms and is derived as

$$p^{\rm C} = p^{\rm C}_{\rm dyn} p^{\rm C}_{\rm stat} \, . \tag{8}$$

These values are provided in Table B.1 in Appendix B.

We find that only 27%, 31%, and 33% of our identified companion candidates have a $p^{\rm C}$ value that is smaller than 0.1, 0.5, and 0.95, respectively. Even though the true membership probabilities might be lower than the values we have derived here, this test strongly suggests that our preselection based on *Gaia* astrometry is a viable method to detect comoving companions to stars that are listed with position and proper motion measurements in *Gaia* EDR3.

We do not detect any trends of objects without any color measurement having significantly higher likelihoods to be unbound. This is expected as the missing color information does not arise from the companion candidates but by the proximity to another object of equal or higher brightness. The majority of the aforementioned 23 companions without color data that are closer than 3″ to the target star from our input catalog exhibits $p^{\rm C} > 0.5$ and 19 out of these even $p^{\rm C} > 0.95$. As expected due to their small projected separations of less than 300 au, these are very likely gravitationally bound stellar binaries. Only three objects without color measurements at separations that are smaller than 3″are found to have $p^{\rm C} < 0.1$

3.5. high confidence companions

When applying a conservative cutoff of $p^{\rm C} > 0.95$ to the full list of preselected companion candidates, 110 objects around 104 targets have a high probability to be gravitationally associated to the star from the input catalog. A detailed list of these high confidence companions and their main parameters is presented in Table 5. For each system we designated the object with the brightest G band magnitude to be the primary. The six remaining triple systems in this list are represented by two individual entries each and we derived all properties with respect to the primary.

The masses and separations of these high confidence binaries are presented in Fig. 7. The majority of the companions exhibit projected separations that are smaller than 1000 au. We find a median separation of 763^{+1933}_{-539} au and no companion is farther separated than 7 000 au. The peak of the separation distribution is located at approximately 50 au, which is in good agreement with general binary statistics (e.g., Duchêne & Kraus 2013). For the masses of the companions we derived a median value of 277^{+505}_{-172} $M_{\rm Jup}$, well in the M dwarf regime. More massive and less massive objects are less frequent among the high confidence companions. As shown in Fig. 3, this statistical evaluation does not consider close-in, low-mass companions that are below the sensitivity of our detection method. The derived median mass might thus be biased for these missing objects. Nevertheless, our results agree well with the findings of Duquennoy & Mayor (1991) and Raghavan et al. (2010), who established a peak in the companion mass ratio distributions to solar-type primaries at $q \approx 0.3$ and $q \approx 0.1$, respectively.

We identified ten sub-stellar objects with masses below 80 $M_{\rm Jup}$ that are very likely to be comoving with $p^{\rm C} > 0.95$. The identifiers and mass estimates for these brown dwarf companions are listed in Table 6. Especially intriguing are Gaia EDR3 5232514298301348864, Gaia EDR3 6039427503765943040, and Gaia EDR3 6043486655875354112 that exhibit masses below 40 $M_{\rm Jup}$. The latter is not too far away from the planetary mass regime with a photometric mass estimate of 24.8 ± 1.0 $M_{\rm Jup}$. Except for Gaia EDR3 5860803696599969280, which was reported in Goldman et al. (2018), these are all newly identified brown dwarf members of Sco-Cen. Their likely companionship to K-type stellar members of this association makes these especially intriguing laboratories not only for spectroscopic follow-up observations but also to study the dynamical evolution of multiple systems in a densely populated stellar birth environment. Whereas the former will allow us to understand the atmospheric architectures and compositions of these sub-stellar objects, the latter will provide important implications for companion migration and ejection mechanisms caused by close stellar encounters.

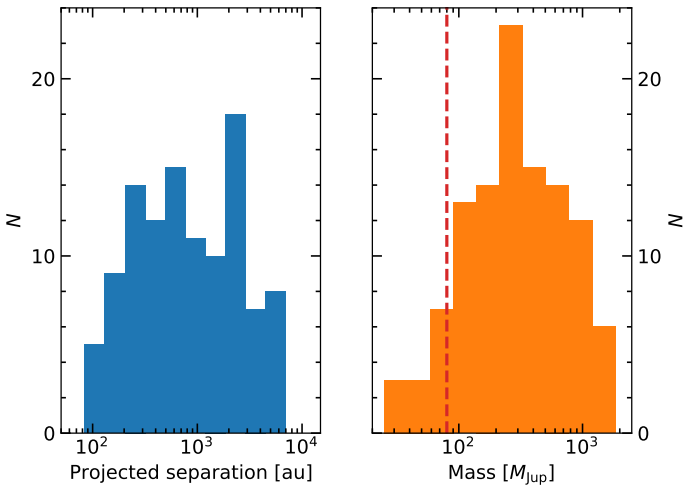

Fig. 7. Properties of high confidence companions to K type Sco-Cen members. *Left panel*: Distribution of separations amongst our high confidence sample. *Right panel*: Mass distribution among this sample. The red dashed line indicates the threshold of brown dwarf and stellar-mass companions at 80 $M_{\rm Jup}$.

4. High-contrast imaging results

In this section we present the results from our high-contrast imaging observations with SPHERE and NACO that were obtained within the scope of YSES. Sect. 4.1 contains a detailed analysis of a brown dwarf companion that we detected to TYC 8252-533-1. We briefly assess the astrometry and photometry of other companions in the SPHERE field of view detected to other YSES targets from our input catalog in Sect. 4.2.

4.1. A brown dwarf companion to TYC 8252-533-1

Our previous analysis revealed that the YSES target TYC 8252-533-1 (2MASS J13233587-4718467; Gaia EDR3 6083750638577673088) harbors a companion with a projected separation of 4.″4 and at a position angle of 204°. As *Gaia* photometry suggests that the companion is of sub-stellar mass and likely a brown dwarf companion, we will refer to it as TYC 8252-533-1 B henceforth. Due to the small angular separation of the binary, both objects were located within the SPHERE field of view during our regular YSES observations. This object is thus an ideal test case to assess the quality of the parameters

Table 5. *Gaia* companion candidates with $p^C > 0.95$ that were identified to K-type Sco-Cen members. In the last column we report whether these systems have been mentioned in previous literature. A full version of the table that is including the parameter uncertainties is available online.

Gaia EDR3 ID		Coordinates[c]		ρ[d]	PA[e]	$\mu_{\alpha*}$[f]		μ_δ		G		References
Prim.[a]	Sec.[b]	Prim. (hh:mm:ss.s ±dd:mm:ss.s)	Sec. (hh:mm:ss.s ±dd:mm:ss.s)	($''$)	(°)	Prim. (mas yr^{-1})	Sec. (mas yr^{-1})	Prim. (mas yr^{-1})	Sec. (mas yr^{-1})	Prim. (mag)	Sec. (mag)	
5232514298297802880	5232514298301348864	10:31:37.1 -69:01:58.7	10:31:36.4 -69:01:49.1	10.3	338.4	-19.27	-19.09	8.46	8.66	11.6	19.9	
5240643988513309952	5240643988513310592	11:17:58.1 -64:02:33.4	11:17:51.8 -64:02:05.6	49.6	304.0	-28.59	-28.64	-0.63	-1.23	7.8	11.4	B19,D19,G18
5332922112460126976	5332922116810986880	11:51:50.4 -64:07:27.7	11:51:50.7 -64:07:27.4	1.6	78.8	-22.80	-22.99	4.70	8.47	11.8	16.6	
5343603288120259072	5343603288130858112	11:55:42.9 -56:37:31.7	11:55:42.8 -56:37:31.2	0.8	304.9	-39.46	-38.91	-7.41	-10.59	11.2	13.0	
6124952431621117056	6124952431621118848	12:05:12.5 -53:31:23.6	12:05:12.2 -53:31:16.7	7.4	339.2	-33.79	-34.33	-9.84	-10.52	12.4	16.5	D19,G18
6057456092878899072	6057456092897714816	12:07:42.3 -62:27:28.2	12:07:42.1 -62:27:29.3	1.6	230.1	-36.37	-37.43	-8.11	-10.30	10.5	13.2	
6071087597518919040	6071087597497876480	12:09:41.8 -58:54:45.2	12:09:40.2 -58:54:41.0	12.8	289.4	-37.47	-37.52	-10.68	-9.54	10.0	15.9	
6071087597518919040	6071087597518919808	12:09:41.8 -58:54:45.2	12:09:41.7 -58:54:41.8	3.5	350.7	-37.47	-34.48	-10.68	-8.39	10.0	13.1	
6129878999619301120	6129879755533544832	12:10:10.6 -48:55:47.8	12:10:09.2 -48:55:44.0	14.1	285.3	-37.49	-36.09	-12.36	-11.87	10.8	13.5	D19,G18
5860803662284763392	5860803696599969280	12:12:08.0 -65:54:55.1	12:12:13.0 -65:54:49.3	31.6	79.4	-37.22	-37.03	-8.27	-8.53	11.1	17.0	G18
6129584364863667840	6129584364863668096	12:12:11.1 -49:50:08.4	12:12:11.0 -49:50:02.0	6.4	352.1	-31.04	-30.20	-9.80	-10.20	11.0	14.9	D19,G18
6075815841096386816	6075816592695096576	12:12:35.7 -55:20:27.5	12:12:36.1 -55:20:00.5	27.3	8.1	-34.08	-33.77	-11.10	-9.86	10.2	12.6	D19,G18
6126585034583698944	6126585034581064192	12:14:34.0 -51:10:12.7	12:14:31.8 -51:10:15.9	21.2	261.4	-34.14	-33.66	-11.78	-10.70	10.3	12.2	D19,G18
6075548419252906368	6075548419252913152	12:14:50.7 -55:47:23.7	12:14:52.2 -55:47:03.8	24.0	33.9	-35.76	-35.21	-10.96	-11.21	8.3	9.6	D19,G18
5855198832989286400	5855198828676205696	12:16:40.1 -70:07:36.3	12:16:39.5 -70:07:35.8	3.2	279.2	-36.10	-36.39	-8.53	-7.80	10.4	13.8	D19,G18
6126648698878768384	6126648703176939392	12:19:59.4 -50:18:40.8	12:19:59.3 -50:18:37.7	3.1	355.5	-25.80	-25.56	-9.31	-9.28	12.3	13.9	
6077461328965244160	6077461328965240576	12:21:08.0 -52:12:22.9	12:21:06.8 -52:12:41.4	21.8	211.9	-35.11	-34.68	-12.80	-13.28	11.4	15.8	D19,G18
6127110188823860480	6127110188823860864	12:22:04.3 -48:41:25.1	12:22:03.9 -48:41:17.7	8.3	333.0	-28.63	-27.60	-10.63	-9.90	10.4	15.7	D19,G18
6078760195785278208	6078760195785506048	12:30:29.5 -52:22:27.2	12:30:30.5 -52:22:28.9	9.2	100.6	-33.60	-34.67	-13.31	-14.35	11.3	13.3	D19,G18
6073105991611649024	6073106193460538240	12:33:33.7 -57:14:06.8	12:33:32.1 -57:14:10.3	13.4	254.6	-37.85	-36.63	-13.91	-14.76	10.5	17.9	
6074563978391541888	6074563978391541504	12:36:58.9 -54:12:18.2	12:36:56.5 -54:12:17.5	20.7	272.0	-35.02	-35.13	-13.13	-13.17	10.1	13.0	D19,G18
6074374346993398144	6074374346993397760	12:39:14.0 -54:54:47.0	12:39:13.8 -54:54:49.1	2.6	216.1	-35.60	-34.44	-14.18	-16.07	11.5	14.3	
6078074169253752064	6078074237969848960	12:40:46.6 -52:11:04.8	12:40:46.1 -52:11:04.3	4.8	276.4	-26.63	-25.89	-11.36	-10.35	11.6	15.0	D19,G18
6079389185156706944	6079389253876183808	12:40:54.5 -50:31:55.4	12:40:53.3 -50:31:47.6	14.1	303.8	-43.33	-43.35	-19.41	-19.86	11.4	14.4	
6060864815105080064	6060864819427739904	12:42:00.5 -57:59:48.8	12:42:00.4 -57:59:49.0	1.3	261.0	-35.42	-32.62	-14.79	-13.70	12.8	13.6	
5862876928853591040	5862876928853590144	12:44:34.7 -63:31:46.5	12:44:35.8 -63:31:49.9	7.9	116.1	-36.13	-37.35	-13.72	-14.82	10.3	15.2	
6074796250199371648	6074796245904371968	12:45:48.8 -54:10:58.7	12:45:49.6 -54:10:41.4	18.8	22.9	-34.84	-34.46	-13.91	-13.38	11.0	13.6	D19,G18
6061376298490107520	6061376298480880512	12:48:48.1 -56:35:38.0	12:48:47.8 -56:35:39.2	2.8	245.8	-29.55	-28.67	-12.13	-12.81	10.1	16.1	
6061310052916532096	6061310052892185088	12:50:44.8 -56:54:48.3	12:50:44.9 -56:54:49.6	1.7	138.2	-37.56	-34.54	-15.76	-13.30	12.4	12.5	
6075310478057303936	6075310478050174592	12:50:51.4 -51:56:35.6	12:50:51.7 -51:56:35.1	3.2	81.1	-34.36	-34.25	-16.59	-15.89	11.5	14.6	D19,G18
6080364825623490688	6080364791268622336	13:06:40.1 -51:59:38.9	13:06:39.5 -51:59:44.7	8.1	224.3	-32.16	-32.35	-17.24	-17.78	10.3	14.2	D19,G18
6056115131031531264	6056115135337482496	13:07:13.0 -59:52:11.3	13:07:13.0 -59:52:09.4	1.9	354.9	-30.46	-29.90	-12.80	-16.47	9.9	13.9	
6067650970822132224	6067650970822131584	13:12:18.0 -54:38:54.2	13:12:18.6 -54:39:05.7	12.5	157.2	-28.59	-29.09	-11.91	-13.20	10.2	11.3	
6088027047281877120	6088027051573430400	13:13:07.1 -45:37:43.9	13:13:07.1 -45:37:44.6	0.7	157.5	-28.26	-29.62	-16.57	-16.34	11.3	12.7	
6083750638577673088	6083750638540951552	13:23:35.8 -47:18:46.9	13:23:35.7 -47:18:51.0	4.4	204.2	-31.18	-32.38	-20.10	-19.69	10.8	16.8	
6082617587508723200	6082617591804976512	13:27:05.9 -48:56:18.5	13:27:06.5 -48:56:18.2	5.8	86.6	-38.26	-38.05	-25.86	-22.45	10.4	13.5	D19,G18
5863747467220738432	5863747462890662144	13:33:54.7 -65:36:41.9	13:33:54.8 -65:36:40.6	1.3	8.3	-34.02	-35.47	-20.78	-19.88	10.7	14.6	
6113000942074857216	6113000946373209216	13:36:40.9 -40:43:36.3	13:36:41.1 -40:43:40.1	4.6	146.2	-30.16	-28.98	-21.69	-20.90	12.0	14.2	
6094572719180018432	6094572753539758976	13:45:41.9 -49:04:59.3	13:45:44.2 -49:04:50.2	24.1	68.0	-24.23	-23.82	-17.62	-18.36	9.1	10.3	
6094529696485204864	6094529696485204736	13:47:50.5 -49:02:05.8	13:47:51.4 -49:01:49.0	19.0	27.4	-23.40	-23.76	-15.39	-16.28	10.6	11.8	D19,G18

Notes. [(a)] Primary of the binary system (i.e. the heavier mass star of the pair). [(b)] Secondary of the binary system (i.e. the lower mass object of the pair). [(c)] Coordinates are given at *Gaia* EDR3 epoch J2016.0. [(d)] ρ denotes the projected separation of the binary. [(e)] PA denotes the position angle (east of north) of the secondary with respect to the primary. [(f)] $\mu_{\alpha*}$ and μ_δ denote the proper motions in RA and Dec, respectively.

References. B19: Bohn et al. (2019); D19: Damiani et al. (2019); G18: Goldman et al. (2018)

Table 5. (continued).

Gaia EDR3 ID		Coordinates[c]		ρ[d]	PA[e]	$\mu_{\alpha*}$[f]		μ_δ		G		References
Prim.[a]	Sec.[b]	Prim.	Sec.			Prim.	Sec.	Prim.	Sec.	Prim.	Sec.	
		(hh:mm:ss.s ±dd:mm:ss.s)	(hh:mm:ss.s ±dd:mm:ss.s)	($''$)	(°)	(mas yr^{-1})	(mas yr^{-1})	(mas yr^{-1})	(mas yr^{-1})	(mag)	(mag)	
5850443307764629376	5850443303440130816	13:54:07.3 -67:33:45.0	13:54:03.1 -67:33:30.7	28.0	300.7	-29.23	-30.18	-5.06	-4.66	10.8	12.4	
5850443307764629376	5850443303446183040	13:54:07.3 -67:33:45.0	13:54:03.4 -67:33:27.3	28.7	308.0	-29.23	-30.50	-5.06	-5.43	10.8	13.7	
6095161370216796928	6095162843384927744	13:55:25.5 -47:06:56.8	13:55:27.6 -47:07:04.8	23.4	110.0	-27.42	-27.88	-22.30	-22.49	10.8	15.1	D19,G18
6114536929757358592	6114536929755100544	13:56:29.6 -38:39:13.0	13:56:29.6 -38:39:13.9	1.0	204.4	-30.41	-29.84	-18.68	-23.20	11.0	12.0	
6109646679996671360	6109646679996673024	14:00:49.7 -42:36:57.3	14:00:50.2 -42:36:48.0	11.0	32.7	-24.53	-25.37	-20.76	-21.39	10.7	13.2	
6116680904413813504	6116680908709624448	14:21:30.5 -38:45:25.1	14:21:30.5 -38:45:26.0	1.1	150.7	-20.59	-19.77	-18.68	-21.01	12.3	12.4	
6092201450556437632	6092201450556434944	14:27:05.5 -47:14:22.1	14:27:04.4 -47:14:37.8	19.1	215.0	-28.17	-28.52	-24.70	-24.30	10.4	16.0	
5894194318558985984	5894194348576228992	14:37:50.2 -54:57:41.6	14:37:52.0 -54:56:44.0	59.7	15.0	-24.67	-25.06	-25.60	-25.97	10.3	12.4	D19,G18
5905886387736675840	5905886215936891008	14:41:35.0 -47:00:29.2	14:41:39.3 -47:00:15.2	46.5	72.4	-27.29	-27.62	-26.57	-26.00	9.8	15.1	
6101758336902846208	6101758332601667712	14:42:15.9 -41:00:18.9	14:42:15.6 -41:00:15.7	4.4	316.5	-27.60	-29.13	-25.83	-26.06	11.1	11.8	
6204234706098895104	6204234706096290688	14:58:45.7 -33:15:10.7	14:58:45.9 -33:15:11.2	2.8	100.3	-13.82	-12.22	-19.70	-18.21	11.8	11.9	
6203845650778424960	6203845655074564864	14:59:44.7 -34:25:47.2	14:59:44.7 -34:25:47.1	0.9	87.1	-25.02	-29.59	-28.70	-31.21	11.1	11.5	
6203959484592343936	6203959488887357824	15:02:26.0 -34:05:13.7	15:02:25.9 -34:05:12.6	1.8	310.4	-18.09	-17.62	-19.78	-19.91	11.9	15.0	
6003698873422956928	6003698907782693248	15:08:51.4 -43:03:22.9	15:08:54.7 -43:03:14.2	37.3	76.6	-19.91	-20.40	-26.14	-26.20	9.4	11.0	
6201456107071825536	6201456107071825792	15:11:04.5 -32:51:30.8	15:11:04.7 -32:51:27.8	4.5	48.8	-20.49	-22.22	-23.31	-22.08	11.5	13.6	
6210702308369949952	6210702415745896192	15:12:44.5 -31:16:48.6	15:12:46.1 -31:17:02.2	24.9	123.2	-17.28	-16.54	-22.64	-21.62	11.3	14.0	
5903894175757504128	5903894175757506176	15:13:58.1 -46:29:14.9	15:13:57.2 -46:29:06.5	12.8	311.2	-17.96	-18.11	-23.52	-24.19	12.1	13.3	
5886747291936159104	5886747291923626240	15:15:22.9 -54:41:09.3	15:15:22.8 -54:41:09.1	1.5	280.0	-21.33	-18.11	-22.89	-25.03	11.9	13.3	
6200310519037175040	6200310484677437184	15:17:10.8 -34:34:20.0	15:17:14.3 -34:33:57.6	48.9	62.8	-21.88	-21.72	-24.59	-24.01	10.9	12.9	
6200310514738629504	6200310519037175040	15:17:10.7 -34:34:37.8	15:17:10.8 -34:34:20.0	17.9	5.1	-20.73	-21.88	-22.73	-24.59	8.0	10.9	
6000349589207590016	6000349657912636928	15:18:01.2 -44:44:27.5	15:18:01.0 -44:44:27.7	2.4	265.1	-27.72	-28.31	-31.99	-34.30	11.4	15.7	
6004331775495542656	6004331779800414464	15:19:16.0 -40:56:08.0	15:19:15.9 -40:56:11.8	3.9	190.2	-21.74	-20.92	-27.20	-27.21	11.0	16.4	
6213042069112745856	6213042073410590464	15:21:52.4 -28:42:38.7	15:21:52.4 -28:42:40.2	1.6	177.0	-19.74	-17.66	-27.32	-25.19	11.3	14.8	
6208136391829015936	6208136396126956928	15:24:11.4 -30:30:58.6	15:24:13.0 -30:30:57.6	20.3	87.2	-22.09	-22.11	-25.07	-24.57	10.6	12.9	
6208136396126956928	6208136396122878976	15:24:13.0 -30:30:57.6	15:24:12.8 -30:30:55.9	3.5	300.1	-22.11	-21.99	-24.57	-25.79	12.9	15.2	
6013649964744749184	6013649969039127552	15:29:38.5 -35:46:51.9	15:29:38.4 -35:46:50.6	2.6	299.1	-23.95	-21.95	-30.37	-29.91	10.7	15.7	
6013480055841212416	6013480060137095296	15:29:47.2 -36:28:37.7	15:29:47.2 -36:28:39.4	1.7	192.7	-14.75	-12.66	-19.66	-20.17	11.4	16.3	
6209492506280547200	6209492506275602816	15:31:29.6 -30:21:54.4	15:31:29.6 -30:21:53.2	1.2	19.1	-14.45	-13.24	-17.99	-20.95	12.4	14.3	
6014539542668216832	6014539645747431680	15:34:23.1 -33:00:09.2	15:34:26.3 -32:59:50.1	43.9	64.2	-20.36	-20.45	-27.60	-27.25	12.1	15.2	
6208381582919629568	6208381587215253504	15:37:02.1 -31:36:40.3	15:37:01.8 -31:36:39.5	4.7	279.8	-20.59	-21.49	-27.87	-28.36	9.8	11.8	
6208381582919629568	6208381587220236160	15:37:02.1 -31:36:40.3	15:37:01.7 -31:36:38.5	5.9	287.5	-20.59	-19.47	-27.87	-27.25	9.8	11.9	
6013399894569703040	6013399830146943104	15:39:27.8 -34:46:17.6	15:39:28.3 -34:46:18.4	6.4	97.8	-13.22	-13.12	-22.12	-21.81	11.7	13.9	
6013398451460692992	6013351520350805632	15:39:46.4 -34:51:02.9	15:39:46.4 -34:51:04.0	1.1	182.6	-15.35	-13.82	-22.28	-20.73	11.9	13.9	
6234377340635038848	6234377718592160384	15:41:06.8 -26:56:26.7	15:41:07.2 -26:56:25.9	6.3	82.1	-18.07	-17.87	-26.64	-24.87	11.0	16.1	
6014696841553696768	6014696841553696896	15:45:12.8 -34:17:31.0	15:45:12.6 -34:17:29.7	2.8	297.2	-14.24	-15.43	-21.78	-20.27	9.8	14.7	
5885915442658792576	5885915442658792448	15:46:29.6 -52:17:24.2	15:46:29.5 -52:17:25.8	1.6	183.3	-21.95	-24.04	-22.60	-21.96	11.1	14.7	
6236477064249469312	6236477064249562624	15:51:45.3 -24:56:51.7	15:51:45.5 -24:56:50.1	2.4	47.4	-9.15	-9.99	-21.77	-23.42	12.0	16.8	
6039427503765943936	6039427503765943040	15:54:51.4 -31:54:46.8	15:54:51.9 -31:54:47.6	6.3	97.7	-9.75	-10.71	-27.23	-27.27	11.6	17.6	
6248340348034690688	6248340343736161664	15:58:20.5 -18:37:25.5	15:58:20.5 -18:37:19.9	5.6	351.8	-17.08	-17.33	-23.43	-24.20	9.9	15.5	
6247571617610119808	6247571583249729280	15:59:11.0 -18:50:44.6	15:59:11.0 -18:50:59.2	14.6	183.0	-10.28	-10.21	-20.89	-21.31	12.6	13.3	
5984404849554176896	5984404849554176256	16:01:10.7 -48:04:44.3	16:01:12.1 -48:04:49.3	15.3	109.1	-20.74	-20.54	-30.67	-30.45	11.4	17.3	
6235806259081172736	6235806323497438592	16:02:39.1 -25:42:08.4	16:02:38.1 -25:41:39.5	31.7	335.8	-20.03	-20.08	-32.57	-32.68	11.6	12.4	
6236273895118889472	6236273895118890112	16:02:51.2 -24:01:57.8	16:02:51.2 -24:01:50.7	7.2	353.2	-11.80	-12.39	-23.99	-24.18	11.9	16.3	
6243393817024157184	6243393817024156288	16:04:21.6 -21:30:28.9	16:04:21.0 -21:30:42.1	16.2	215.7	-12.45	-12.64	-23.81	-24.75	11.7	13.6	
6249074718717359744	6249074718725644288	16:06:23.5 -18:14:19.5	16:06:23.5 -18:14:18.9	0.6	328.8	-8.81	-8.97	-20.67	-21.26	12.1	12.2	

Table 5. (continued).

Gaia EDR3 ID		Coordinates[c]		ρ[d]	PA[e]	$\mu_{\alpha*}$[f]		μ_δ		G		References
Prim.[a]	Sec.[b]	Prim.	Sec.			Prim.	Sec.	Prim.	Sec.	Prim.	Sec.	
		(hh:mm:ss.s ±dd:mm:ss.s)	(hh:mm:ss.s ±dd:mm:ss.s)	($''$)	(°)	(mas yr^{-1})	(mas yr^{-1})	(mas yr^{-1})	(mas yr^{-1})	(mag)	(mag)	
6042124910722287744	6042124915024285440	16:06:57.9 -27:43:10.1	16:06:57.9 -27:43:08.7	1.5	6.1	-12.84	-9.82	-24.24	-24.14	8.1	11.8	
5998266426996208384	5998266426996209408	16:07:33.7 -37:59:24.7	16:07:33.5 -37:59:21.4	3.6	339.2	-17.53	-16.34	-28.33	-29.33	12.4	14.7	
5983063479721274880	5983063479721275520	16:08:07.7 -50:41:56.2	16:08:07.1 -50:41:52.9	6.2	302.0	-22.03	-21.01	-36.43	-37.88	11.5	13.6	
6043486660173351552	6043486655875354112	16:08:43.4 -26:02:17.2	16:08:44.4 -26:02:14.2	13.5	77.4	-10.72	-10.86	-25.18	-24.95	10.0	18.7	
6245777283349430912	6245777283349431552	16:09:00.7 -19:08:53.1	16:09:00.0 -19:08:37.3	19.0	326.6	-9.37	-9.44	-25.12	-24.89	12.9	15.4	
6035794030167079808	6035794030168507264	16:10:11.7 -32:26:36.1	16:10:11.7 -32:26:36.9	1.3	131.9	-9.65	-9.13	-23.03	-23.02	11.8	12.1	
6245781097280740864	6245781131640479360	16:10:21.7 -19:04:07.0	16:10:21.8 -19:04:02.4	4.6	6.6	-9.05	-8.60	-24.05	-24.78	13.6	16.9	
6042235793900264448	6042235725180784768	16:10:26.5 -27:56:30.0	16:10:28.2 -27:56:40.1	24.6	114.3	-9.61	-8.61	-34.54	-36.19	13.1	13.2	
6243833724749589632	6243833724749589760	16:10:42.0 -21:01:32.4	16:10:41.8 -21:01:30.6	3.2	305.7	-9.88	-10.09	-23.34	-24.59	11.8	15.5	
6242176653347275136	6242176829446854656	16:12:55.3 -23:19:46.1	16:12:52.6 -23:19:56.4	38.3	254.4	-9.55	-8.48	-23.71	-23.94	9.1	11.8	
6022499010422921088	6022499006128860928	16:13:58.0 -36:18:13.9	16:13:58.0 -36:18:19.6	5.7	178.8	-16.14	-17.36	-30.32	-31.12	10.8	13.3	
6243089247998315264	6243089217937775360	16:14:00.3 -21:08:44.3	16:13:58.1 -21:09:17.6	45.8	223.3	-9.90	-9.60	-20.96	-20.56	13.0	15.5	
5935099415271699072	5935099415267651328	16:14:52.0 -50:26:19.0	16:14:52.2 -50:26:19.9	2.2	114.4	-20.08	-16.52	-31.57	-32.12	10.2	11.4	
6242598526515737728	6242598526515738112	16:15:34.6 -22:42:43.1	16:15:34.5 -22:42:41.3	1.9	339.3	-7.90	-9.54	-25.97	-26.33	12.3	13.3	
6042418858284146688	6042418862581174016	16:16:14.2 -26:43:15.5	16:16:14.1 -26:43:14.2	2.5	300.5	-17.79	-17.25	-26.92	-28.46	11.7	12.6	
6050056478369804288	6050056482664014976	16:18:37.2 -24:05:23.0	16:18:37.2 -24:05:18.5	4.5	0.1	-11.86	-10.28	-20.04	-21.53	11.0	11.5	
6048571072519663872	6048571076818643968	16:19:12.2 -25:50:38.5	16:19:12.2 -25:50:39.8	1.3	175.5	-11.38	-10.81	-23.39	-25.84	12.5	16.1	
6037784008760031872	6037784004457590528	16:26:57.6 -30:32:28.4	16:26:57.0 -30:32:23.9	9.3	298.8	-20.31	-18.66	-32.99	-34.28	11.1	11.6	
6037784008760031872	6037784004457597568	16:26:57.6 -30:32:28.4	16:26:57.5 -30:32:31.8	3.6	197.1	-20.31	-18.70	-32.99	-33.03	11.1	12.6	
6031823178275372800	6031823173966757120	16:30:37.9 -29:54:22.9	16:30:37.8 -29:54:18.4	5.0	333.2	-17.35	-20.53	-31.34	-30.66	10.6	14.9	
6045791575844270208	6045791953801392128	16:32:00.6 -25:30:29.2	16:32:01.6 -25:30:25.8	14.2	76.2	-11.52	-10.65	-23.08	-22.83	12.5	12.7	
6047289699098449920	6047289699098450944	16:34:53.1 -25:18:17.4	16:34:53.2 -25:18:07.3	10.2	6.0	-13.21	-12.96	-23.18	-24.05	10.0	14.8	
5967552634824947456	5967552634824945152	16:43:01.4 -44:05:27.9	16:43:02.3 -44:05:33.2	10.8	119.1	-8.89	-8.60	-19.79	-19.36	11.6	17.1	
6046749289143173504	6046749319188591104	16:45:26.1 -25:03:17.0	16:45:29.0 -25:02:48.0	48.1	52.8	-4.04	-4.00	-23.47	-23.49	10.6	14.4	
4130416623473262720	4130416726552477440	16:47:37.1 -20:14:27.3	16:47:38.4 -20:14:15.8	22.1	58.6	-8.10	-8.50	-21.94	-21.26	11.8	14.6	

Table 6. Brown dwarf companions companions with $p^C > 0.95$.

Gaia EDR3 ID	G band photometric mass (M_{Jup})
5232514298301348864	36.5 ± 2.4
6071087597497876480	76.0 ± 16.7
5860803696599969280	66.2 ± 4.5
6073106193460538240	46.5 ± 3.3
6083750638540951552	48.7 ± 11.1
6039427503765943040	33.8 ± 3.6
5984404849554176256	73.8 ± 4.4
6043486655875354112	24.8 ± 1.0
6245781131640479360	43.1 ± 5.8
6243833724749589760	78.9 ± 12.5

that were derived from the *Gaia* catalog by comparison to independent photometry and astrometry acquired with SPHERE. To characterize this companion independently from the *Gaia* measurements, we acquired SPHERE dual-band measurements ranging from Y to K band and additional NACO L' data as described in Sect. 2.3. The final images for several SPHERE filters and our NACO data are presented in Appendix A.

4.1.1. Stellar parameters

A summary of the basic stellar parameters of TYC 8252-533-1 is presented in Table 7. To convert the photometric contrasts measured in the SPHERE and NACO data into absolute fluxes, it was necessary to characterize the primary star first. We analyzed its spectral energy distribution (SED) with VOSA (Bayo et al. 2008) using flux measurements from Tycho (Høg et al. 2000), APASS (Henden et al. 2012), *Gaia* EDR3 (Gaia Collaboration et al. 2021), DENIS (DENIS Consortium 2005), 2MASS (Skrutskie et al. 2006; Cutri et al. 2003), and WISE (Cutri et al. 2012b). Pecaut & Mamajek (2016) measured an extinction of $A_V = 0.16$ mag and reported that the star is likely to host a debris disk based on the infrared excess that was observed in WISE $W3$ and $W4$ filters. The STILISM reddening map (Lallement et al. 2014) provides a total visual extinction of $A_V = (0.05 \pm 0.05)$ mag at the position and distance of our target. We therefore allowed extinctions in the range $0\,\text{mag} < A_V < 0.2\,\text{mag}$ and excluded the $W3$ and $W4$ measurements from the fit of the stellar SED.

As the stellar flux measurements of the primary might be affected by flux from the close companion we briefly assessed the extent of this potential contamination. The fractional contribution from the secondary to the measured flux of the primary is maximized for the longest wavelengths of the analyzed SED[7]. Equation (2) of Bohn et al. (2020c) yields a contribution of 0.04 mag to the stellar magnitude in L' band if the binary was unresolved in the photometric data. This contribution is significantly smaller for shorter wavelengths where the contrast between both objects is larger. We therefore do not perform any correction of the flux measurements for the primary, as the contribution from the secondary is below 5% and thus already considered in the larger uncertainties of the magnitude contrast values as presented in Table 9, when deriving the fluxes of the companion.

[7] This statement is verified by the lowest magnitude contrast ΔMag between primary and secondary that is measured in the L' band (see Table 9).

Table 7. Properties of TYC 8252-533-1.

Parameter	Value	Reference(s)
Main identifier	TYC 8252-533-1	(1)
2MASS identifier	J13233587-4718467	(2)
Gaia EDR3 ID	6083750638577673088	(3)
Right Ascension[a]	13:23:35.8	(3)
Declination[a]	-47:18:46.9	(3)
Spectral Type	K3Ve	(4,5)
Mass [$M_\odot$]	1.2	(5)
$T_{\rm eff}$ [K]	$4,500 \pm 50$	(6)
$\log(L_*/L_\odot)$	-0.06 ± 0.02	(6)
Age [Myr]	5	(5)
Parallax [mas]	7.71 ± 0.09	(3)
Distance [pc]	129.5 ± 1.4	(3,7)
$\mu_{\alpha*}$ [mas / yr]	-31.183 ± 0.085	(3)
μ_δ [mas / yr]	-20.105 ± 0.078	(3)
B [mag]	11.96	(1)
V [mag]	11.20	(1)
$G_{\rm BP}$ [mag]	11.43	(3)
G [mag]	10.80	(3)
$G_{\rm RP}$ [mag]	10.04	(3)
J [mag]	9.03	(2)
H [mag]	8.40	(2)
K_s [mag]	8.31	(2)
$W1$ [mag]	8.17	(8)
$W2$ [mag]	8.13	(8)
$W3$ [mag]	7.94	(8)
$W4$ [mag]	7.10	(8)

Notes. [(a)] Coordinates are given at *Gaia* EDR3 epoch J2016.0.

References. (1) Høg et al. (2000); (2) Cutri et al. (2012a); (3) Gaia Collaboration et al. (2021); (4) Torres et al. (2006); (5) Pecaut & Mamajek (2016); (6) this work; (7) Bailer-Jones et al. (2021); (8) Cutri et al. (2012b).

The stellar distance was fixed to 130 pc using the estimate from Bailer-Jones et al. (2021) based on *Gaia* EDR3 parallaxes, and we assumed a solar-like metallicity of the primary. We fitted a grid of BT-Settl models (Allard et al. 2012; Baraffe et al. 2015) in a χ^2 minimizing approach, and the best fit of the data was provided by a model with an effective temperature of $T_{\rm eff} = 4500 \pm 50\,K$, a surface gravity of $\log(g) = 2.6 \pm 0.3$ dex, a stellar luminosity of $\log(L_*/L_\odot) = -0.06 \pm 0.02$, and a visual extinction parameter of $A_V = 0.13 \pm 0.06$ mag. These values are in good agreement with the properties that Pecaut & Mamajek (2016) derived for TYC 8252-533-1.

4.1.2. Brown dwarf astrometry

To assess whether our high-contrast data confirm a bound orbit of TYC 8252-533-1 B, we extracted the relative astrometry with respect to the primary star for all of our observations. For SPHERE we used the general astrometric solution presented in Maire et al. (2016) with a true north correction of $-1.^\circ75 \pm 0.^\circ08$ and plate scales of 12.255 mas px^{-1}, 12.251 mas px^{-1}, and 12.265 mas px^{-1} for $H2$, H, and K_s band images, respectively. The NACO data were calibrated with a plate scale of 27.193 ± 0.059 mas px^{-1} (Launhardt et al. 2020) but no true north correction was applied as discussed in Bohn et al. (2020a). The derived separations and position angles are presented in Ta-

Table 8. Relative astrometry of TYC 8252-533-1 B with respect to the primary.

Epoch	Filter	Separation ($''$)	PA ($^\circ$)
J2015.5	G	4.4115 ± 0.0001	204.230 ± 0.002
J2016.0	G	4.4119 ± 0.0001	204.241 ± 0.001
2017-04-02	H	4.414 ± 0.005	204.09 ± 0.09
2019-04-07	K_s	4.437 ± 0.005	204.11 ± 0.09
2019-04-15	L'	4.426 ± 0.011	204.34 ± 0.11
2020-02-19	$H2$	4.424 ± 0.005	204.13 ± 0.09

Notes. The G band astrometric data originate from the *Gaia* DR2 (epoch J2015.5) and EDR3 (epoch J2016.0) catalogs. These filters have different pass bands.

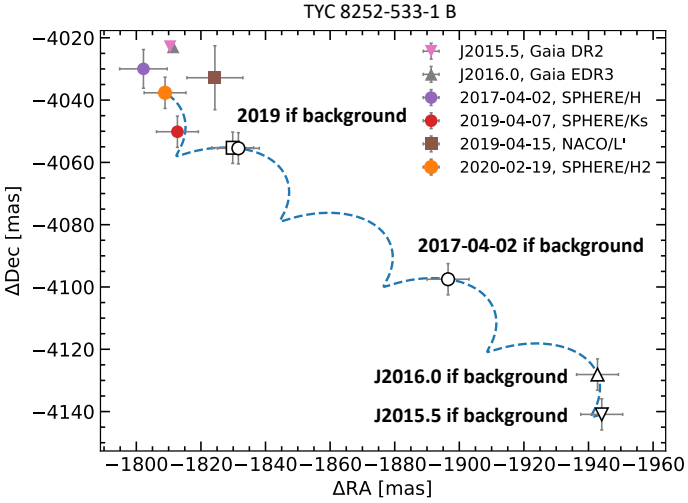

Fig. 8. Proper motion analysis of TYC 8252-533-1 B. The colored markers represent the relative offsets in RA and Dec with respect to the primary that we measured in SPHERE and NACO imaging data or derived from the *Gaia* DR2 and EDR3 catalogs. The blue dashed line illustrates the trajectory of a static background object at infinity and the white markers along the curve represent the hypothetical positions of such an object at the epoch of the corresponding observation.

ble 8 and visualized in Fig. 8. The measurements clearly confirm that the path of TYC 8252-533-1 B is highly inconsistent with the simulated trajectory of a static background object. Instead, the relative astrometric offsets with respect to the primary are in good agreement with the small relative velocity that is expected from an orbit with a projected angular separation of approximately 570 au. Even though there remain some systematic sources of uncertainties between the astrometric measurements that originate from different instruments or filters, the high-contrast imaging data clearly confirm the hypothesis, based on the *Gaia* data, that TYC 8252-533-1 B is a bound companion to the solar-type primary TYC 8252-533-1.

4.1.3. Brown dwarf photometry

The de-reddened photometry of TYC 8252-533-1 B and its host star are presented in Table 9. The listed *Gaia* photometry is directly obtained from the EDR3 catalog and the infrared photometry originates from our high-contrast imaging data. We applied the previously determined extinction of $A_V = 0.13$ mag

Table 9. De-reddened photometry of TYC 8252-533-1 and its brown dwarf companion.

Filter	Magnitude star (mag)	ΔMag (mag)	Flux companion (erg s^{-1} cm^{-2} μm^{-1})
G_{BP}	11.43	6.73 ± 0.05	$(0.22 \pm 0.01) \times 10^{-11}$
G	10.80	5.94 ± 0.01	$(0.503 \pm 0.002) \times 10^{-11}$
G_{RP}	10.04	5.20 ± 0.02	$(1.02 \pm 0.02) \times 10^{-11}$
$Y2$	9.34	5.84 ± 0.96	$(0.50 \pm 0.44) \times 10^{-11}$
$Y3$	9.25	5.59 ± 0.93	$(0.58 \pm 0.49) \times 10^{-11}$
$J2$	9.06	4.79 ± 0.17	$(1.05 \pm 0.16) \times 10^{-11}$
$J3$	8.86	4.68 ± 0.15	$(1.07 \pm 0.15) \times 10^{-11}$
$H2$	8.34	4.47 ± 0.09	$(0.96 \pm 0.08) \times 10^{-11}$
$H3$	8.26	4.37 ± 0.09	$(0.96 \pm 0.08) \times 10^{-11}$
$K1$	8.22	4.25 ± 0.05	$(0.49 \pm 0.02) \times 10^{-11}$
K	8.22	4.20 ± 0.05	$(0.44 \pm 0.02) \times 10^{-11}$
$K2$	8.22	4.04 ± 0.04	$(0.46 \pm 0.02) \times 10^{-11}$
L'	8.16	3.62 ± 0.31	$(0.10 \pm 0.03) \times 10^{-11}$

Notes. The G band values originate directly from *Gaia* EDR3 whereas the infrared measurements of the companion are based on our SPHERE and NACO data. The stellar magnitudes at infrared wavelengths are derived from SED modeling as described in Sect. 4.1.1.

to correct the presented fluxes. As the SPHERE H band data from 2017-04-02 were collected in poor atmospheric conditions and with a very unstable AO performance, we disregarded the photometry that was extracted from these observations in our further analysis. We fitted the full optical and infrared SED of the companion utilizing the MCMC approach described in Bohn et al. (2020b). We used a linearly interpolated grid of BT-Settl models (Allard et al. 2012; Baraffe et al. 2015) with effective temperatures $T_{\rm eff}$ between 1500 K and 4000 K, surface gravity in the range of $0 < \log(g) < 6$, and solar metallicity. We further allowed object radii R from 0.5 $R_{\rm Jup}$ to 5 $R_{\rm Jup}$. The MCMC sampler was implemented in the `emcee` framework (Foreman-Mackey et al. 2013) and we used 100 walkers with 10,000 steps to sample the posterior distribution. In accordance with the computed autocorrelation time of approximately 200 steps, the first 1000 samples of each chain were discarded as burn-in phase and we further continued using each twentieth step of the remaining chains. This provided 45,000 samples for our posterior distribution in ($T_{\rm eff}$, $\log(g)$, R), which are visualized in Fig. C.1 of Appendix C. From these distributions we derived an effective temperature of $T_{\rm eff} = 3092^{+186}_{-91}$ K, a surface gravity of $\log(g) = 3.41^{+1.07}_{-0.31}$ dex, and a radius of $R = 3.5^{+0.3}_{-0.4}$ $R_{\rm Jup}$ for TYC 8252-533-1 B. These values were obtained as the 95 % confidence intervals around the medians of the posterior distributions. From these three parameters we derived the object luminosity as $\log(L_*/L_\odot) = -1.99^{+0.01}_{-0.02}$. The results of this SED fit are presented in Fig. 9. Interestingly, the derived object radius is markedly larger than usual radii of field brown dwarfs of this mass, which are in the order of 1 $R_{\rm Jup}$ (e.g., Chabrier et al. 2009). This inflated photometric radius, however, is nothing unusual for sub-stellar companions at this young age, and similarly large values have been reported for various planetary-mass objects (e.g., Schmidt et al. 2008; Bohn et al. 2019; Stolker et al. 2020).

To convert the results of this analysis to a mass estimate for the companion, we assumed a system age of 5 ± 2 Myr (Pecaut & Mamajek 2016). The kinematic parallax that Pecaut & Mamajek (2016) used for this target (7.83 mas) is not far from the

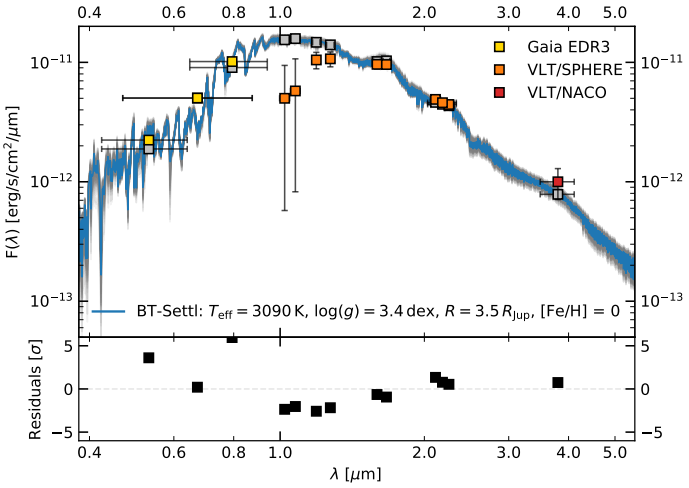

Fig. 9. SED of TYC 8252-533-1 B. The yellow, orange, and red squares indicate the photometry we measured for *Gaia*, SPHERE, and NACO filters, respectively. The bars in x direction indicate the width of the filter transmission curves. The blue curve presents the median model from our posterior distribution of the SED fit as shown in Fig. C.1 of Appendix C. We present the integrated flux of this median model in the applied filters with the grey squares and we visualize 100 randomly selected models from our posterior distribution as grey curves. In the bottom panel we present the residuals of the fit.

Gaia EDR3 value of 7.71 mas. The difference in age due to the different adopted distances should therefore be considered in our assigned uncertainties. Evaluation of BT-Settl isochrones at this age and with our derived luminosity yielded a mass of $52^{+17}_{-11}\,M_{\rm Jup}$ for TYC 8252-533-1 B, which makes it likely a brown dwarf companion to the solar-type primary. This value is in good agreement with the photometric mass estimate of $48.7 \pm 11.1\,M_{\rm Jup}$ derived from the *Gaia* G band flux.

4.1.4. System architecture

Based on the observed infrared excess in the W3 and W4 filters the primary star likely hosts a debris disk (Pecaut & Mamajek 2016, and Sect. 4.1.1). Our direct imaging data do not reveal any scattered light flux of this postulated debris ring, which is most likely below the detection sensitivity of our total intensity observations. Nevertheless, we assessed the relative location of this newly identified brown dwarf companion with respect to the circumstellar material. As our photometric data cover only wavelengths shorter than 22 μm (W4), we most likely do not sample the peak of the infrared excess emission; hence we could only derive an upper limit for the temperature of the dust grains in the disk. We assumed a single species of dust grains that is located at a radial separation $r_{\rm dust}$ from the central star, and modeled the thermal dust emission by a single blackbody with a dust temperature $T_{\rm dust}$. As the peak of this emission is detected either in W4 or at longer wavelengths, we could constrain a maximum dust temperature of $T_{\rm dust} \leq 130$ K. We converted this dust temperature to a minimum disk radius of $r_{\rm dust} \geq 4$ au, utilizing a temperature-radius relation as presented by Backman & Paresce (1993) with

$$\frac{r_{\rm dust}}{1\,{\rm au}} = \left(\frac{L_*}{L_\odot}\right)^{0.5} \left(\frac{278\,{\rm K}}{T_{\rm dust}}\right)^2 , \quad (9)$$

where L_* denotes our previously determined stellar luminosity. Even though this lower limit does not rule out that the debris disk around the primary might extend up to a separation in the order of the projected separation of 570 au that we measure for TYC 8252-533-1 B, this scenario is expected to be extremely unlikely, as it would require dust temperatures as low as 10 K. In agreement with temperature and radius measurements from other debris disk studies that rely on either SED modeling (e.g., Moór et al. 2011) or spatially resolved imaging of these environments (e.g., Pawellek et al. 2014), we conclude that TYC 8252-533-1 B is thus very likely located outside the debris disk of its primary star.

TYC 8252-533-1 B is a new data point to the catalog of debris-disk systems that are harboring giant exoplanets or brown dwarf companions such as HR 8799 (Marois et al. 2008, 2010), β Pictoris (Lagrange et al. 2009, 2010), HD 95086 (Rameau et al. 2013), HD 106906 (Bailey et al. 2014), HR 3549 (Mawet et al. 2015), HR 2562 (Konopacky et al. 2016), or HR 206893 (Milli et al. 2017). While the giant companions HR 8799 bcde, β Pic b, HD 95086 b, HR 2562 B, and HR 206893 B are located inside the debris disks of their host stars, HD 106906 b, HR 3549 B, and TYC 8252-533-1 B are residing beyond these. Whereas the objects in the former category might have formed via core accretion (Pollack et al. 1996; Alibert et al. 2005; Dodson-Robinson et al. 2009; Lambrechts & Johansen 2012) or gravitational instabilities in the protoplanetary disk (Boss 1997; Rafikov 2005; Durisen et al. 2007; Kratter et al. 2010; Boss 2011), similar formation mechanisms are unlikely for the objects that are found outside the circumstellar disks of their hosts, as *in situ* formation at these large separations is not supported by these mechanisms, and migration from within the current disk is unlikely without disrupting the circumstellar environment (Raymond et al. 2012). As concluded by Bailey et al. (2014) for HD 106906, it is thus likely that TYC 8252-533-1 B rather formed via a star-like pathway by fragmentation processes in the collapsing protostellar cloud (Kroupa 2001; Chabrier 2003). Future astrometric observations to constrain the orbital parameters of this brown dwarf and spectroscopic analysis of its atmospheric composition are required to confirm this suggested formation scenario.

4.2. Stellar companions in the SPHERE field of view

Six additional companion candidates from the *Gaia* preselection were also identified in the SPHERE observations that were collected within the scope of YSES. Contrary to TYC 8252-533-1 B, most of these companions seem to exhibit masses that are in good agreement with stellar nature of these objects. In this section we briefly assess the combined SPHERE and *Gaia* astrometry and photometry of these objects. The numerical values are presented in Table 10. We used 2MASS JHK photometry of the systems to derive the absolute magnitudes for the companion candidates. For 2MASS J12195938-5018404, 2MASS J12505143-5156353, and 2MASS J12560830-6926539 the *Gaia* companion candidates are spatially resolved by 2MASS, so they should not pollute the flux measurement of the primary. This is not the case for 2MASS J12391404-5454469, 2MASS J13130714-4537438, and 2MASS J13335481-6536414, for which the fluxes of both sources are blended. Furthermore, we identified an additional companion candidate at a separation of approximately 0.″2 to 2MASS J12560830-6926539, which is resolved neither by 2MASS nor *Gaia*. To obtain an unbiased estimate for the flux of the primary star, we corrected the 2MASS magnitudes of these unresolved pairs for the additional contribution, utilizing Eq. (2) from Bohn et al. (2020c). These revised values are reported in Table 10. As for the Gaia fluxes, the SPHERE photometric measurements were converted to ob-

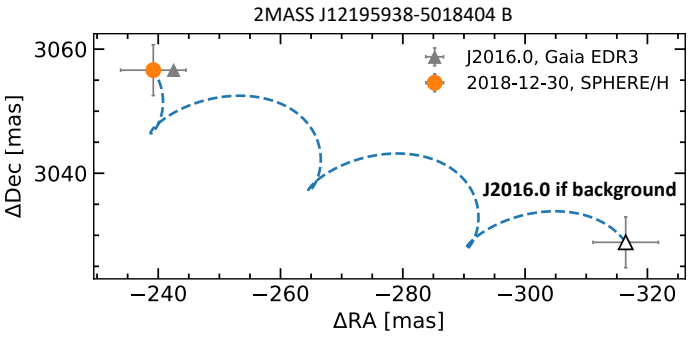

Fig. 10. Proper motion analysis of 2MASS J12195938-5018404 B. See Fig. 8 for a detailed description of the plot elements.

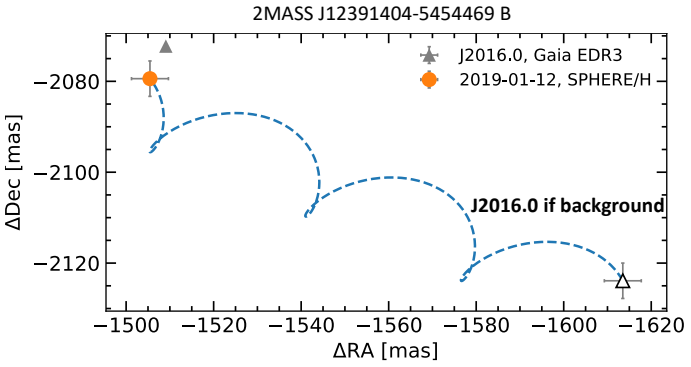

Fig. 11. Proper motion analysis of 2MASS J12391404-5454469 B. See Fig. 8 for a detailed description of the plot elements.

ject masses by BT-Settl models that were evaluated at the system age. The corresponding imagery of these additional companions is shown in Fig. A.2 in Appendix A.

4.2.1. 2MASS J12195938-5018404

The candidate companion detected to 2MASS J12195938-5018404 clearly seems to be stellar in nature. Whereas the Gaia G band photometry indicates an object mass of 464.7±29.3 $M_{\rm Jup}$, the SPHERE near infrared photometry favors slightly lower masses of approximately 375 $M_{\rm Jup}$. Both measurements are consistent at 2σ level and the slightly higher Gaia value might originate from uncorrected flux contribution of the primary star. As visualized in Fig. 10, SPHERE and Gaia astrometry for the companion candidate are highly consistent. This is also supported by a companionship probability of $p^{\rm C} = 100\,\%$ as derived from *Gaia* astrometry alone. We thus conclude that 2MASS J12195938-5018404 B is a stellar secondary to its solar-mass primary. The binary has a projected separation of approximately 470 au.

4.2.2. 2MASS J12391404-5454469

The companion candidate to 2MASS J12391404-5454469 is supposedly of stellar mass. The *Gaia* photometry is consistent with a mass of $189.1 \pm 41.9\ M_{\rm Jup}$. Again, the SPHERE data favor a smaller object mass of approximately $110\ M_{\rm Jup}$. The proper motion analysis clearly supports that the companion candidate is gravitationally bound to the primary star, and has a projected separation of approximately 275 au (see Fig. 11). This combined astrometric analysis is confirmed by $p^{\rm C} = 100\,\%$ that was derived from *Gaia* data alone. We will thus refer to the object as 2MASS J12391404-5454469 B henceforth.

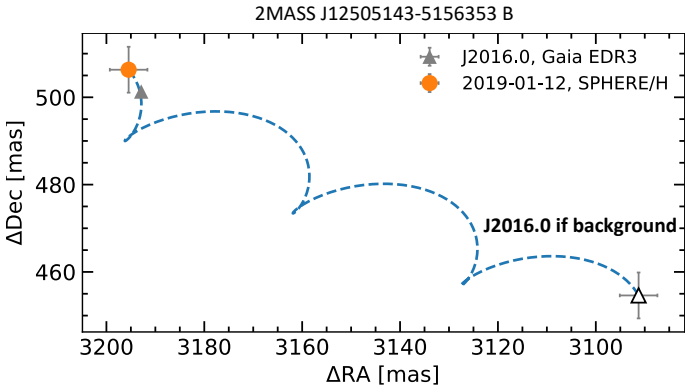

Fig. 12. Proper motion analysis of 2MASS J12505143-5156353 B. See Fig. 8 for a detailed description of the plot elements.

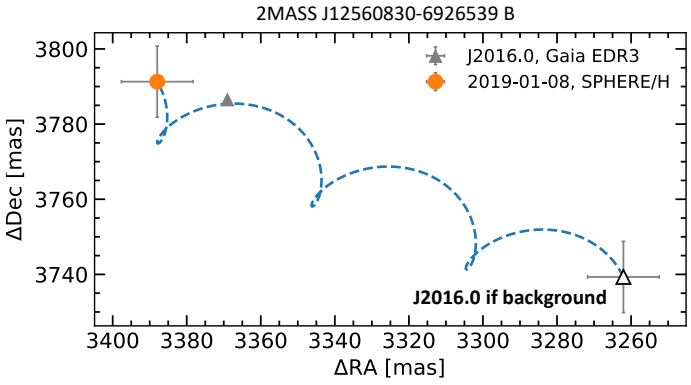

Fig. 13. Proper motion analysis of 2MASS J12560830-6926539 B. See Fig. 8 for a detailed description of the plot elements.

4.2.3. 2MASS J12505143-5156353

The three mass estimates derived from SPHERE H and K_s band and *Gaia* G band data agree particularly well for the candidate companion to 2MASS J12505143-5156353. As presented in Fig. 12, the object is clearly comoving with the primary star. The *Gaia* companionship probability of $p^{\rm C} = 100\,\%$ that we derived for this object strongly supports this conclusion. It should therefore be named 2MASS J12505143-5156353 B, a stellar companion with a mass of approximately $185\ M_{\rm Jup}$. The projected separation between primary and secondary is approximately 350 au.

4.2.4. 2MASS J12560830-6926539

As presented in Fig. 13 the astrometry from *Gaia* and SPHERE for the candidate companion to 2MASS J12560830-6926539 clearly disfavors a static background object. But the relative astrometric measurements for both epochs are too disjunct to allow a bound orbit within the measurement uncertainties. This conclusion seems to be supported by a velocity ratio of $v_{\rm proj}/v_{\rm max} = 1.36 \pm 0.06$ and a *Gaia* companionship probability of $p^{\rm C} = 0\,\%$.

The reason for this inconsistency can be identified in the high-contrast imaging data collected on 2MASS J12560830-6926539 (see Fig. A.2 in Appendix A). The primary star is resolved into a visual binary with an angular separation of

Table 10. SPHERE astrometric and photometric measurements of stellar companions identified by the *Gaia* search.

Target (2MASS ID)	Date (yyyy-mm-dd)	Filter	Sep. (mas)	PA (°)	$m_\star{}^a$ (mag)	Δm (mag)	$M_{\rm comp}$ (mag)	Phot. mass ($M_{\rm Jup}$)
12195938-5018404	2018-12-30	H	3066 ± 4	355.5 ± 0.1	9.86	1.162 ± 0.016	5.107 ± 0.016	$370.5^{+25.6}_{-38.7}$
12195938-5018404	2018-12-30	K_s	3067 ± 4	355.5 ± 0.1	9.65	1.086 ± 0.072	4.821 ± 0.072	$380.4^{+34.4}_{-42.8}$
12391404-5454469	2019-01-12	H	2567 ± 4	215.9 ± 0.1	9.07	1.976 ± 0.016	5.887 ± 0.016	$111.3^{+56.9}_{-40.6}$
12391404-5454469	2019-01-12	K_s	2568 ± 3	215.9 ± 0.1	8.96	1.835 ± 0.006	5.632 ± 0.008	$106.1^{+59.9}_{-37.7}$
12505143-5156353	2019-01-12	H	3235 ± 4	81.0 ± 0.1	8.71	2.157 ± 0.016	5.675 ± 0.016	$190.5^{+26.5}_{-51.3}$
12505143-5156353	2019-01-12	K_s	3240 ± 4	81.0 ± 0.1	8.63	2.061 ± 0.002	5.501 ± 0.006	$180.1^{+24.1}_{-56.6}$
12560830-6926539	2019-01-08	H	5085 ± 9	41.8 ± 0.1	8.54	3.740 ± 0.030	7.291 ± 0.053	$36.2^{+2.6}_{-6.9}$
12560830-6926539	2019-01-08	K_s	5086 ± 6	41.7 ± 0.1	8.30	3.388 ± 0.377	6.700 ± 0.379	$39.9^{+12.5}_{-8.9}$
13130714-4537438	2017-07-05	J	707 ± 3	157.5 ± 0.3	9.59	0.800 ± 0.003	4.669 ± 0.037	$312.4^{+181.0}_{-121.8}$
13130714-4537438	2017-07-05	H	706 ± 3	157.4 ± 0.3	8.99	0.659 ± 0.002	3.926 ± 0.036	$318.3^{+176.5}_{-121.7}$
13335481-6536414	2018-04-30	H	1340 ± 3	8.2 ± 0.2	8.14	2.517 ± 0.004	5.599 ± 0.005	$80.2^{+67.3}_{-3.2}$
13335481-6536414	2018-04-30	K_s	1341 ± 3	8.2 ± 0.1	7.91	2.529 ± 0.003	5.380 ± 0.004	$76.7^{+61.9}_{-3.1}$
13335481-6536414	2020-02-16	H	1341 ± 3	8.4 ± 0.1	8.23	2.585 ± 0.053	5.661 ± 0.053	$79.4^{+64.9}_{-5.1}$

Notes. [a] Stellar 2MASS magnitudes. For 2MASS J12391404-5454469, 2MASS J12560830-6926539, 2MASS J13130714-4537438, and 2MASS J13335481-6536414 we corrected the 2MASS magnitudes for the contribution of close, unresolved companions.

0.″218 ± 0.″006. The fainter of the two stars is detected at a position angle of 33.°8 ± 1.°6. The binarity of the source was identified within the scope of the Search for associations containing young stars (SACY; Torres et al. 2006; Elliott et al. 2015) and confirmed by Tokovinin et al. (2019). It also affects the accuracy of the provided *Gaia* astrometry. The *Gaia* measurements exhibit an astrometric excess noise of 2.3 mas (`astrometric_excess_noise` parameter) that is detected at a significance of approximately 6 820 (`astrometric_excess_noise_sig` parameter). This significance is much larger than the threshold of 2 that is required for a certain corruption of the astrometric measurements (see Lindegren et al. 2021b). This conclusion is also supported by a renormalised unit weight error (RUWE) of ∼ 13; for well-behaved sources RUWE ≈ 1 is expected. As parallaxes and proper motions for the binary and the *Gaia* companion candidate are highly consistent, it is very likely that these three objects form a gravitationally bound triple system. Further astrometric monitoring will help to confirm this hypothesis.

The companion candidate from *Gaia* has been spectroscopically analyzed by Riaz et al. (2006). The authors determined a spectral type of M1 and classified it as a stellar object. This is in stark contrast to the photometric mass estimates that we derived from both *Gaia* and SPHERE. The *Gaia* G band photometry is consistent with a mass of 44.5 ± 5.8 $M_{\rm Jup}$ and the SPHERE H and K_s band data indicate object masses of 36^{+3}_{-7} $M_{\rm Jup}$ and 40^{+13}_{-9} $M_{\rm Jup}$, respectively. These values are consistent within their uncertainties and suggest that Gaia EDR3 5844909156504880128 (2MASS J12560892-6926503) is a brown dwarf rather than a stellar companion. It is possible that Riaz et al. (2006) misclassified the companion, perhaps due to contaminating flux from the primary star that was leaking into the slit with a width of 1.″5. Further spectroscopic measurements will help to confirm the sub-stellar nature of this outer companion in a young triple system.

4.2.5. 2MASS J13130714-4537438

The *Gaia* and SPHERE astrometric measurements for the companion candidate to 2MASS J13130714-4537438 are highly consistent and indicate that this object is gravitationally bound to its Sun-like primary (see Fig. 14). This conclusion was also drawn from *Gaia* astrometry alone, for which we calculated $p^{\rm C}$ = 100 %. We derived photometric mass estimates of $312.4^{+181.0}_{-121.8}$ $M_{\rm Jup}$ and $318.3^{+176.5}_{-121.7}$ $M_{\rm Jup}$ from the SPHERE H and K_s band data, respectively. The corresponding *Gaia* mass of 414.4 ± 114.2 $M_{\rm Jup}$ is marginally higher, but well consistent within the uncertainties. These mass errors are relatively large for this object. Due the the young age of the system of 2^{+2}_{-1} Myr, the object mass can vary significantly when propagating the age uncertainties. 2MASS J13130714-4537438 B is likely a stellar-mass companion at a projected separation of approximately 100 au.

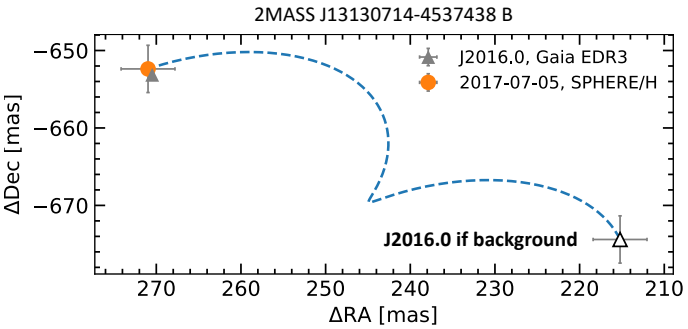

Fig. 14. Proper motion analysis of 2MASS J13130714-4537438 B. See Fig. 8 for a detailed description of the plot elements.

4.2.6. 2MASS J13335481-6536414

As visualized in Fig. 15, the three astrometric data points collected with SPHERE and *Gaia* are in very good agreement with each other. This analysis and the *Gaia* companionship probability of $p^{\rm C}$ = 100 % strongly support that 2MASS J13335481-6536414 B is a gravitationally bound companion with a projected separation of approximately 140 au. Both optical and near infrared photometric mass estimates for the secondary agree very well within their uncertainties. Whereas the photometric

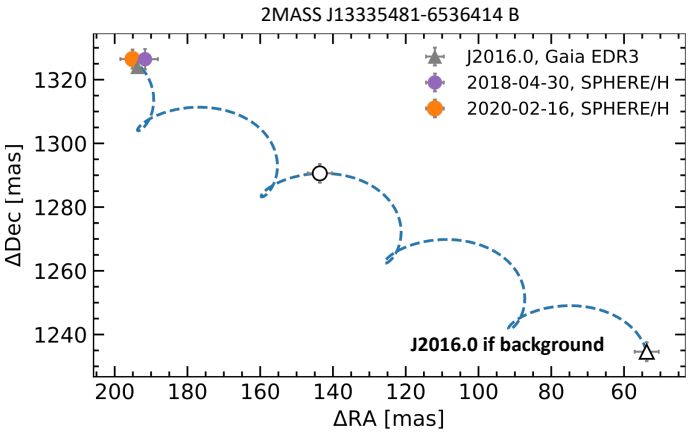

Fig. 15. Proper motion analysis of 2MASS J13335481-6536414 B. See Fig. 8 for a detailed description of the plot elements.

mass estimate from *Gaia* suggests that 2MASS J13335481-6536414 B is a low-mass stellar object with a mass of 91.9 ± 31.0 $M_{\rm Jup}$, the SPHERE data indicate that it might be of substellar nature with a mass of approximately 78 $M_{\rm Jup}$. But the upper boundaries of the SPHERE measurements also allow for stellar masses. Future data will be required to discern whether 2MASS J13335481-6536414 B is a high-mass brown dwarf or rather low-mass stellar companion.

An additional companion candidate to 2MASS J13335481-6536414 at a projected separation of more than 1000 au is detected by the *Gaia* preselection algorithm. For this object with the identifier Gaia EDR3 5863747467220738432 we derived $v_{\rm proj}/v_{\rm max} = 1.32 \pm 0.02$ and hence $p^{\rm C} = 0\,\%$. It is possible that the visual stellar binary of 2MASS J13335481-6536414 AB is corrupting the astrometric measurements for the primary. Further monitoring will be necessary to determine the orbital parameters of this binary. These data will be helpful to assess whether the additional companion candidate is consistent with a bound orbit after all and was just rejected due to the velocity contribution from the inner binary.

5. Discussion

5.1. preselection criteria

Even though we have detected several high confidence companions in *Gaia* EDR3, it is necessary to evaluate the quality of our preselection criteria as to whether *bona fide* binaries might be neglected or too many unbound objects are identified. Due to the nature of our companionship assessment, it is vital that our companion candidates must have a well constrained parallax measurement. It is thus justified to dismiss any data without or with loosely constrained parallaxes. Setting the maximum value of the parallax uncertainty to 0.5 mas defines a rather conservative threshold and considers larger uncertainties due to imprecise astrometry for small separation binaries or objects close to *Gaia*'s sensitivity limit. Of course, true companions with small angular separations can exhibit even larger uncertainties and might thus be rejected from our preselected sample (these are the companions that reside close to or within the red, dashed exclusion triangle presented in Fig. 3). Within the scope of this work, however, a rejection of these companions need not be considered as a drawback, because other techniques such as lucky imaging (e.g., Janson et al. 2012) speckle interferometry (e.g., Tokovinin et al. 2010) or AO-assisted high-contrast imaging (e.g., Wang et al. 2015; Bonavita et al. 2021) are much stronger in detecting these close, visual binaries.

The applied 20 % deviation in parallax measurements of the primary and companion candidate does not exclude any *bona fide* binaries either; again with the exception of very close pairs with corrupted astrometry. Given the median parallaxes of our target stars ($\varpi = 7.55$ mas, see Fig. 2), this criterion defines a potential radial separation of up to ~ 33 pc ($\approx 7 \times 10^6$ au), which is significantly larger than the average distance between stars in a young association (e.g., Kraus & Hillenbrand 2008). The same cutoff threshold is applied for similar searches presented by Fontanive et al. (2019) and Fontanive & Bardalez Gagliuffi (2021). The 10 km s^{-1} interval that we chose for the proper motions is justified in a similar manner. Close companions show a non-negligible amount of orbital motion with respect to the primary star. For a solar-mass primary, a BD companion of 40 $M_{\rm Jup}$ with a semi-major axis of 100 au would exhibit an orbital velocity of 3 km s^{-1}. For a Sun-like secondary with a semi-major axis of 50 au this velocity is even as large as 6 km s^{-1}. The 10 km s^{-1} interval is thus required to account for both potential scenarios and additional velocity uncertainties. Both parallax and proper motion criteria applied in our preselection are rather conservative choices. This ensures that no *bona fide* binaries get neglected by the algorithm. A refinement of the preselected sample as presented in Sect. 3 is necessary to reject clearly unbound objects afterwards.

The most important parameter for our selection is probably the cutoff radius of $\rho_{\rm cutoff} = 10\,000$ au in projected separation. The same threshold is also applied within the COCONUTS program that relies on a similar selection methodology (Zhang et al. 2020, 2021). Basic geometry demands that the larger one chooses this parameter, the more companions will be preselected by the algorithm, especially when applying it to a densely populated region on the sky. It is expected, however, that the fraction of high confidence candidates with $p^{\rm C} > 0.95$ among all preselected objects decreases with increasing $\rho_{\rm cutoff}$. To assess this correlation, we repeated our full analysis with a cutoff radius of $\rho_{\rm cutoff} = 200'000$ au ≈1 pc. This agrees with the 20 times larger cutoff radius that was previously applied in our companionship probability assessment (see Sect. 3.4). In Fig. 16 we show the fraction of high confidence companions to the total number of potential companions identified within a radius of $\rho_{\rm cutoff}$. A clear correlation between the chosen cutoff radius and the number of high confidence objects is visible and the ratio decreases continuously when increasing $\rho_{\rm cutoff}$. For large separations the allowed velocities are in the order of the uncertainties we derive from the differential proper motions, so it becomes hard to assess whether these are actually bound or not. Our chosen cutoff separation lies just before the steepest decrease of the fraction of high confidence companions. Increasing the cutoff separation would therefore also increase the number of preselected yet unbound companion candidates. We thus argue that $\rho_{\rm cutoff} = 10\,000$ au is a good choice that allows for the detection of several wide-orbit companions, without diluting the preselected sample by an abundance of unbound contaminants. This is supported by the non-detection of any high confidence companions with a projected angular separation that is larger than 7000 au (see Table 5 and Fig. 7).

5.2. Quality assessment of derived Gaia properties

As we detect seven companion candidates in both SPHERE and *Gaia* measurements, these systems provide ideal test cases to assess the quality of the companion properties that we derived

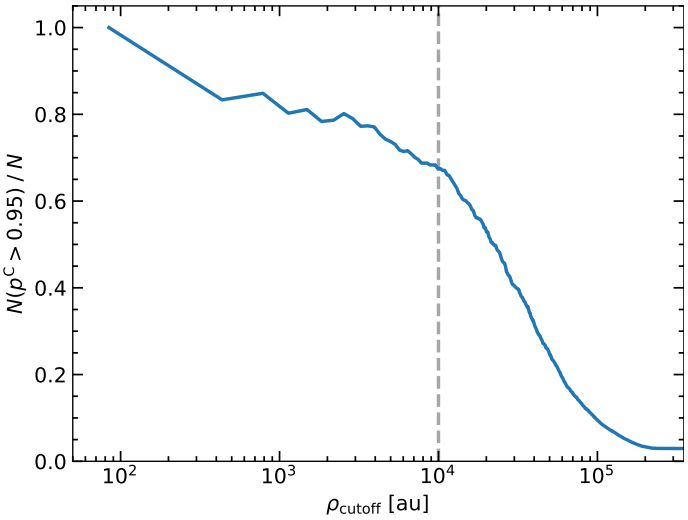

Fig. 16. Fraction of high confidence companions to the total number of identified companion candidates within a specified radius ρ_{cutoff}. We show the fractional amount of companions with $p^C > 0.95$ to the total number N of preselected objects interior to our cutoff radius ρ_{cutoff}. The grey, dashed line marks the chosen cutoff radius of $\rho_{cutoff} = 10\,000$ au.

for the remaining sample members. This analysis was focused on two important parameters that were extracted from our *Gaia* analysis as presented in Sect. 3: (i) the co-movement hypothesis of the companion and (ii) the companion mass estimate.

For all these companion candidates but the one detected to 2MASS J12560830-6926539 we derived a velocity ratio v_{proj}/v_{max} that is smaller than unity. This resulted in companionship probabilities $p^C > 0.95$, indicating that these are gravitationally bound companions. These hypotheses are confirmed for all cases, when analyzing the relative astrometric offsets between the SPHERE and *Gaia* epochs as presented in Sect. 4. SPHERE and *Gaia* astrometric measurements are highly consistent and prove the claimed companionship status. Even though the astrometric measurements from both instruments do not agree within their uncertainties for the companion candidate around 2MASS J12560830-6926539, this is no indication that our classification scheme does not work. As detailed in Sect. 4.2.4, the primary is a visual binary itself that is unresolved in the *Gaia* catalog. For that reason, the measured astrometry is corrupted and does not agree with our SPHERE data. Previous work however strongly indicated that the companion candidate is indeed gravitationally bound, and all three objects form a triple system.

We conclude that the differential velocities directly measured in the *Gaia* catalog are trustworthy, at least for companions that are as bright or brighter and at least as far separated from the primary as the benchmark targets with complementary SPHERE data. Due to the small angular separation of less than 5″.5, these are already quite challenging cases and for the majority of brighter and farther separated companions, a similar or better performance of the evaluation method can be expected. Further monitoring and reduction of the velocity uncertainties as presented in Fig. 6 is required to confirm co-movement for all the companion candidates that were detected during our search. Precise measurements of the RVs of the companions are necessary to obtain a complete three dimensional picture of the orbital dynamics and parameters.

For all seven companions the photometric masses determined by either SPHERE or *Gaia* are consistent within $2\,\sigma$ intervals. Especially the masses of the identified sub-stellar companions to TYC 8252-533-1, 2MASS J12560830-6926539, and 2MASS J13335481-6536414 are in exceptional agreement. It is thus likely that the mass estimates we derived for all identified companions are good estimates for the actual object masses. Given its rather close separation to the primary star and a G band contrast of $\Delta G \approx 6$ mag, TYC 8252-533-1 B is one of the more challenging cases for extraction of *Gaia* photometry (which is also visualized by the proximity of the object to the red exclusion zone that is highlighted in Fig. 3). It is therefore likely that the extraction of these relevant *Gaia* parameters could be performed at higher accuracy, leading to more trustworthy results for the objects that are farther away from the red-dashed triangle in Fig. 4. Of course this is not true for companions that are closely located to *Gaia*'s G band magnitude limit of approximately 21 mag, for which the small amount of received flux creates larger uncertainties in the measured parameters.

When inspecting the derived masses for the potential triple system comprising two of our targets from the input catalog (2MASS J15241147-3030582 and 2MASS J15241303-3030572) and a third lower-mass companion, it appears that our mass estimates for the stellar members of this trio are quite different from the input masses we adopted from Pecaut & Mamajek (2016). As listed in Table B.1, we derived the same mass estimate of approximately 0.7 $M_\odot$ for both stars, which should be very distinct with 1.1 $M_\odot$ and 0.4 $M_\odot$ for 2MASS J15241147-3030582 and 2MASS J15241303-3030572, respectively. This discrepancy is not caused by the marginally different parallaxes assumed for the corresponding primary, which only results in a magnitude difference of 0.05 mag. The main source of error stems from the two very different ages of 18 Myr and 1 Myr that Pecaut & Mamajek (2016) give for the two targets, which also results in the very different mass estimates of the third companion Gaia EDR3 6208136396122878976. Based on the same apparent G band magnitude of this object, we derived masses of 0.23 $M_\odot$ and 0.08 $M_\odot$, respectively, with the higher mass corresponding to the older system age. If the system is indeed a gravitationally bound stellar triple, which is strongly suggested by the derived values of $p^C \approx 1$, all three components should roughly be of the same age, which would also avoid the change in mass of more than 100% for the lightest member of the system. When trying to reproduce the stellar masses of the two targets from Pecaut & Mamajek (2016) based on the measured G band photometry and BT-Settl isochrones, we find best agreement with a system age of approximately 4 Myr, which provides masses of 1.13 $M_\odot$, 0.45 $M_\odot$, and 0.14 $M_\odot$ for 2MASS J15241147-3030582, 2MASS J15241303-3030572, and Gaia EDR3 6208136396122878976, respectively.

We see similar age and mass discrepancies for the other multiple systems that contain stars from our input catalog as identified companion candidates. This clearly shows that our derived object masses have to be used carefully as they are heavily affected by the underlying system age. Further refinements of the stellar age such as updated *Gaia* distances and coevality constraints for the identified multiple systems are thus required to properly constrain derived objects masses. Further spectral coverage of the SEDs of the detected companions is also necessary, to determine their properties with much higher accuracy than our results, which are based on a single photometric data point. As most of the identified objects are reasonably separated from the primary, spectroscopic follow-up measurements are easily possible and can in most cases even be performed without any AO-assisted instruments.

Further data releases of the *Gaia* mission might also improve the parameters derived in this study, and it should be straight-

forward to update the presented results in the future. The photometric uncertainties, especially of the very faint objects, will certainly be improved with more observational data points, even though the provided G band magnitudes were already precise enough so that these only had a marginal influence on the precision of the derived quantities. It is not clear if color measurements for all our companion candidates will be available in future releases as most of these incompletely characterized objects are very close to a source of equal or higher brightness, which will always be problematic for precise photometric measurements. Higher accuracy astrometry will certainly help to reject or confirm marginal cases from our current study and it will provide new candidate companions that were discarded by our present preselection, either due to non-existing proper motion measurements or too large astrometric uncertainties.

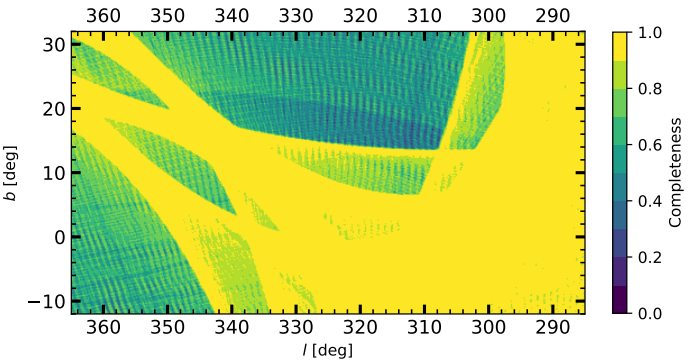

Fig. 17. Completeness of *Gaia* DR2 as a function of position on sky. The completeness is calculated for objects as faint as $G = 21$ mag.

5.3. Comparison to similar studies

There are two main studies that have utilized *Gaia* DR2 to reveal members of Sco-Cen. Goldman et al. (2018) identified additional *Gaia* members in the LCC, which is the Sco-Cen sub-group that YSES is focusing on. This moving group comprises several low-mass stellar and brown dwarf objects, whose membership had not been revealed before *Gaia* DR2. Damiani et al. (2019) focus on the stellar population of Sco-Cen and they identify almost 11,000 pre-main sequence members by *Gaia* astrometry and photometry. To assess whether any of our candidates have been picked up by either of these studies, we cross-matched our identified companions with the output catalogs of both surveys. We focused on the systems with a companionship probability $p^{\rm C} > 0.95$ as presented in Table 5 and we found that 20 of our detected companions were listed in both of the studied catalogs. One additional source was identified only by Goldman et al. (2018). Interestingly, only companions with a right ascension below 15h were picked up by either of these previous studies. This is not surprising for the work of Goldman et al. (2018), as these authors were explicitly targeting the LCC, which does not extend to a right ascension greater than 15h. However, none of these discussed surveys identified individual binary or multiple systems as part of their analysis.

5.4. Completeness

We assessed the completeness of our companion detection method based on the completeness of the *Gaia* DR2 catalog. Using the `selectionfunctions` introduced by Boubert et al. (2020) and Boubert & Everall (2020), we derived the completeness as a function of the position on sky for objects down to the *Gaia* magnitude threshold of $G = 21$ mag. The resulting completeness map is presented in Fig. 17. The map shows clear patterns that correspond to the scanning scheme of the *Gaia* satellite. For most of the coordinates of our Sco-Cen targets, the achieved completeness is higher than 80 % and the LCC, which is covering an area of approximately $290° < l < 310°$ and $-10° < b < 20°$, has a completeness coverage of almost 100 %. As the underlying code is relying on *Gaia* DR2 we expect the actual completeness of Gaia EDR3 to be even higher.

6. Conclusions

We present a method to find comoving companions utilizing the early version of the third data release of ESA's *Gaia* mission. We applied this preselection algorithm to a sample of 480 K-type pre-main sequence stars presented by Pecaut & Mamajek (2016) aiming to find new (sub-)stellar companions for them. With our selection criteria we identify 163 potential companions to 142 members of our input catalog, including 21 candidate triples systems. We could show that the sensitivity of *Gaia* to detect such companion candidates improves with increasing angular separation from the target star. For our K-type stars we reach the background limit of $G \approx 20$ mag for separations larger than $10''$. Utilizing age estimates from Pecaut & Mamajek (2016), we converted the measured photometry to mass estimates of the companion candidates using BT-Settl (Allard et al. 2012; Baraffe et al. 2015) and MIST (Dotter 2016; Choi et al. 2016) models for (sub-)stellar objects. The age and distance of our sample allows for detections of objects with masses as low as 20 $M_{\rm Jup}$.

To corroborate the companionship status of the preselected objects we performed tests based on the available photometry and relative astrometry. Color-magnitude analysis, which was accessible for the majority of our candidate companions, is in agreement with evolutionary models of young, (sub-)stellar objects. We further compared differential projected velocities $v_{\rm proj}$ of each potential binary to the maximum velocity that still permits bound orbits, $v_{\rm max}$. Based on the posterior distributions of the calculated $v_{\rm proj}$ to $v_{\rm max}$ ratios and the statistical constraints from the stellar density around the target star we derived likelihood estimates of a companion to be bound, $p^{\rm C}$. Only 27% from our identified companion candidates exhibited a companionship probability of less than 10%. Instead, 110 objects (67%) reside in the $p^{\rm C} > 0.95$ regime, which we designate as our high confidence targets henceforth. Amongst these we found ten candidate brown dwarf companions:

- Gaia EDR3 5232514298301348864, $M = 36.5 \pm 2.4\ M_{\rm Jup}$,
- Gaia EDR3 6071087597497876480, $M = 76.0 \pm 16.7\ M_{\rm Jup}$,
- Gaia EDR3 5860803696599969280, $M = 66.2 \pm 4.5\ M_{\rm Jup}$,
- Gaia EDR3 6073106193460538240, $M = 46.5 \pm 3.3\ M_{\rm Jup}$,
- Gaia EDR3 6083750638540951552, $M = 48.7 \pm 11.1\ M_{\rm Jup}$,
- Gaia EDR3 6039427503765943040, $M = 33.8 \pm 3.6\ M_{\rm Jup}$,
- Gaia EDR3 5984404849554176256, $M = 73.8 \pm 4.4\ M_{\rm Jup}$,
- Gaia EDR3 6043486655875354112, $M = 24.8 \pm 1.0\ M_{\rm Jup}$,
- Gaia EDR3 6245781131640479360, $M = 43.1 \pm 5.8\ M_{\rm Jup}$,
- Gaia EDR3 6243833724749589760, $M = 78.9 \pm 12.5\ M_{\rm Jup}$.

These ten brown dwarf companions are suitable for future follow-up observations with ground- and space-based telescopes, aiming to understand their atmospheric architectures and dynamical histories.

For seven of the detected candidate companions we used complementary high-contrast imaging data. These were collected with the SPHERE and NACO instruments as part of

YSES, a direct imaging search for sub-stellar companions around Sun-like stars (Bohn et al. 2020a). The astrometry that was extracted from this near infrared data was in excellent agreement with the *Gaia* measurements and confirmed the companionship of six candidates. The remaining target, 2MASS J12560830-6926539, was resolved into a visual binary that was corrupting the astrometric measurements. This system is likely to be a triple with a brown dwarf companion of about 40 $M_{\rm Jup}$.

Another interesting target that was observed with both instruments is TYC 8252-533-1. This solar-type star hosts a sub-stellar companion at a projected separation of 4.″4 that was picked up by *Gaia* and could be directly imaged within the scope of our survey. Complementary data collected with SPHERE and NACO covered the spectral energy distribution of the companion from 1 to 4 microns and we derived an effective temperature of $T_{\rm eff} = 3092^{+186}_{-91}$ K, a surface gravity of $\log(g) = 3.41^{+1.07}_{-0.31}$ dex, a radius of $R = 3.5^{+0.3}_{-0.4}$ $R_{\rm Jup}$, and a luminosity of $\log(L_*/L_\odot) = -1.99^{+0.01}_{-0.02}$. We converted the latter parameter to an object mass by evaluation of BT-Settl isochrones at the system age of 5 ± 2 Myr, which provided a mass of 52^{+17}_{-11} $M_{\rm Jup}$. With a projected physical separation of 570 au, this brown dwarf companion is likely to reside beyond the debris disk that is found around its host star based on an infrared excess in WISE W3 and W4 bands. As postulated for the widely separated planetary-mass companion HD 106906 b that was detected outside the circumstellar disk around its primary (Bailey et al. 2014), a star-like formation pathway for TYC 8252-533-1 B is favored over planetary formation channels such core accretion or gravitational instabilities in the protoplanetary disk.

The photometric mass estimates independently derived from SPHERE and *Gaia* data do also agree very well for the seven targets that were observed with both instruments. We conclude that *Gaia* can properly characterize all objects from our sample that are at lest equally bright and separated from their host stars. Nevertheless, one should treat the derived mass estimates for the remaining objects with some care, as these are based on a single photometric measurement, and that this parameter is very sensitive to the system age, which needs to be determined better in some cases.

We have shown that our proposed method is a viable tool to identify comoving companions to Sco-Cen members in *Gaia* data. It should be applicable to arbitrary samples of input stars, but some justified age and primary mass estimates are required to derive secondary masses and their companionship probability. The parameter space that is probed by this approach is highly complementary to the comparably small field of view of current high-contrast imaging instruments. To obtain a detailed understanding of the occurrence rates of giant, sub-stellar companions and their underlying formation mechanisms, it is important not to neglect this population of widely separated objects.

Acknowledgements. We would like to thank the anonymous referee for the detailed feedback they provided. Their comments helped the authors to improve the quality of the manuscript. We dedicate this article to the memory of France Allard, who passed away in October 2020. Her groundbreaking work on low-mass stars, brown dwarfs, and exoplanets strongly shaped our current understanding of their atmospheric physics; the models she (co-)developed – that were also used in this work and that were frequently accessed by a vast number of researchers – will remain as a crucial foundation to all future studies in this field and astronomy in general. The research of A.J.B. leading to these results has received funding from the European Research Council under ERC Starting Grant agreement 678194 (FALCONER). Part of this research was carried out at the Jet Propulsion Laboratory, California Institute of Technology, under a contract with the National Aeronautics and Space Administration (80NM0018D0004). G.C. thanks the Swiss National Science Foundation for financial support under grant number 200021_169131. This research has used the SIMBAD database, operated at CDS, Strasbourg, France (Wenger et al. 2000). This work has used data from the European Space Agency (ESA) mission *Gaia* (https://www.cosmos.esa.int/gaia), processed by the *Gaia* Data Processing and Analysis Consortium (DPAC, https://www.cosmos.esa.int/web/gaia/dpac/consortium). Funding for the DPAC has been provided by national institutions, in particular the institutions participating in the *Gaia* Multilateral Agreement. This publication makes use of VOSA, developed under the Spanish Virtual Observatory project supported by the Spanish MINECO through grant AyA2017-84089. To achieve the scientific results presented in this article we made use of the *Python* programming language[8], especially the *SciPy* (Virtanen et al. 2020), *NumPy* (Oliphant 2006), *Matplotlib* (Hunter 2007), *emcee* (Foreman-Mackey et al. 2013), *scikit-image* (Van der Walt et al. 2014), *scikit-learn* (Pedregosa et al. 2012), *photutils* (Bradley et al. 2016), and *astropy* (Astropy Collaboration et al. 2013, 2018) packages.

References

Alcalá, J. M., Manara, C. F., Natta, A., et al. 2017, A&A, 600, A20
Alcalá, J. M., Natta, A., Manara, C. F., et al. 2014, A&A, 561, A2
Alibert, Y., Mordasini, C., Benz, W., & Winisdoerffer, C. 2005, A&A, 434, 343
Allard, F., Homeier, D., & Freytag, B. 2012, Philosophical Transactions of the Royal Society of London Series A, 370, 2765
Astropy Collaboration, Price-Whelan, A. M., Sipőcz, B. M., et al. 2018, AJ, 156, 123
Astropy Collaboration, Robitaille, T. P., Tollerud, E. J., et al. 2013, A&A, 558, A33
Backman, D. E. & Paresce, F. 1993, in Protostars and Planets III, ed. E. H. Levy & J. I. Lunine, 1253
Bailer-Jones, C. A. L., Rybizki, J., Fouesneau, M., Demleitner, M., & Andrae, R. 2021, AJ, 161, 147
Bailey, V., Meshkat, T., Reiter, M., et al. 2014, ApJ, 780, L4
Baraffe, I., Homeier, D., Allard, F., & Chabrier, G. 2015, A&A, 577, A42
Bayo, A., Rodrigo, C., Barrado Y Navascués, D., et al. 2008, A&A, 492, 277
Beuzit, J. L., Vigan, A., Mouillet, D., et al. 2019, A&A, 631, A155
Bohn, A. J., Ginski, C., Kenworthy, M. A., et al. 2021, A&A, 648, A73
Bohn, A. J., Kenworthy, M. A., Ginski, C., et al. 2019, A&A, 624, A87
Bohn, A. J., Kenworthy, M. A., Ginski, C., et al. 2020a, MNRAS, 492, 431
Bohn, A. J., Kenworthy, M. A., Ginski, C., et al. 2020b, ApJ, 898, L16
Bohn, A. J., Southworth, J., Ginski, C., et al. 2020c, A&A, 635, A73
Bonavita, M., Gratton, R., Desidera, S., et al. 2021, arXiv e-prints, arXiv:2103.13706
Boss, A. P. 1997, Science, 276, 1836
Boss, A. P. 2011, ApJ, 731, 74
Boubert, D. & Everall, A. 2020, MNRAS, 497, 4246
Boubert, D., Everall, A., & Holl, B. 2020, MNRAS, 497, 1826
Bradley, L., Sipocz, B., Robitaille, T., et al. 2016, Photutils: Photometry tools
Chabrier, G. 2003, PASP, 115, 763
Chabrier, G., Baraffe, I., Leconte, J., Gallardo, J., & Barman, T. 2009, in American Institute of Physics Conference Series, Vol. 1094, 15th Cambridge Workshop on Cool Stars, Stellar Systems, and the Sun, ed. E. Stempels, 102–111
Chauvin, G., Desidera, S., Lagrange, A. M., et al. 2017, Astronomy and Astrophysics, 605, L9
Choi, J., Dotter, A., Conroy, C., et al. 2016, ApJ, 823, 102
Comerón, F. 2008, The Lupus Clouds, ed. B. Reipurth, Vol. 5, 295
Cropper, M., Katz, D., Sartoretti, P., et al. 2018, A&A, 616, A5
Cutri, R. M., Skrutskie, M. F., van Dyk, S., et al. 2012a, VizieR Online Data Catalog, II/281
Cutri, R. M., Skrutskie, M. F., van Dyk, S., et al. 2003, VizieR Online Data Catalog, II/246
Cutri, R. M. et al. 2012b, VizieR Online Data Catalog, II/311
Damiani, F., Prisinzano, L., Pillitteri, I., Micela, G., & Sciortino, S. 2019, A&A, 623, A112
de Zeeuw, P. T., Hoogerwerf, R., de Bruijne, J. H. J., Brown, A. G. A., & Blaauw, A. 1999, AJ, 117, 354
DENIS Consortium. 2005, VizieR Online Data Catalog, II/263
Dodson-Robinson, S. E., Veras, D., Ford, E. B., & Beichman, C. A. 2009, ApJ, 707, 79
Dotter, A. 2016, ApJS, 222, 8
Duchêne, G. & Kraus, A. 2013, ARA&A, 51, 269
Duquennoy, A. & Mayor, M. 1991, A&A, 500, 337
Durisen, R. H., Boss, A. P., Mayer, L., et al. 2007, in Protostars and Planets V, ed. B. Reipurth, D. Jewitt, & K. Keil, 607
Eggleton, P. P. & Tokovinin, A. A. 2008, MNRAS, 389, 869
Elliott, P., Huélamo, N., Bouy, H., et al. 2015, A&A, 580, A88
Fontanive, C. & Bardalez Gagliuffi, D. 2021, Frontiers in Astronomy and Space Sciences, 8, 16

[8] Python Software Foundation, https://www.python.org/

Fontanive, C., Rice, K., Bonavita, M., et al. 2019, MNRAS, 485, 4967
Foreman-Mackey, D., Hogg, D. W., Lang, D., & Goodman, J. 2013, PASP, 125, 306
Gaia Collaboration, Brown, A. G. A., Vallenari, A., et al. 2018, A&A, 616, A1
Gaia Collaboration, Brown, A. G. A., Vallenari, A., et al. 2021, A&A, 649, A1
Gaia Collaboration, Prusti, T., de Bruijne, J. H. J., et al. 2016, A&A, 595, A1
Goldman, B., Röser, S., Schilbach, E., Moór, A. C., & Henning, T. 2018, ApJ, 868, 32
Haffert, S. Y., Bohn, A. J., de Boer, J., et al. 2019, Nature Astronomy, 3, 749
Henden, A. A., Levine, S. E., Terrell, D., Smith, T. C., & Welch, D. 2012, Journal of the American Association of Variable Star Observers (JAAVSO), 40, 430
Høg, E., Fabricius, C., Makarov, V. V., et al. 2000, A&A, 355, L27
Hunter, J. D. 2007, Computing in Science and Engineering, 9, 90
Janson, M., Hormuth, F., Bergfors, C., et al. 2012, ApJ, 754, 44
Keppler, M., Benisty, M., Müller, A., et al. 2018, A&A, 617, A44
Konopacky, Q. M., Rameau, J., Duchêne, G., et al. 2016, ApJ, 829, L4
Kouwenhoven, M. B. N., Goodwin, S. P., Parker, R. J., et al. 2010, MNRAS, 404, 1835
Kratter, K. M., Murray-Clay, R. A., & Youdin, A. N. 2010, ApJ, 710, 1375
Kraus, A. L. & Hillenbrand, L. A. 2008, ApJ, 686, L111
Kroupa, P. 2001, MNRAS, 322, 231
Lagrange, A. M., Bonnefoy, M., Chauvin, G., et al. 2010, Science, 329, 57
Lagrange, A. M., Gratadour, D., Chauvin, G., et al. 2009, A&A, 493, L21
Lallement, R., Vergely, J. L., Valette, B., et al. 2014, A&A, 561, A91
Lambrechts, M. & Johansen, A. 2012, A&A, 544, A32
Launhardt, R., Henning, T., Quirrenbach, A., et al. 2020, A&A, 635, A162
Lenzen, R., Hartung, M., Brandner, W., et al. 2003, in Society of Photo-Optical Instrumentation Engineers (SPIE) Conference Series, Vol. 4841, Instrument Design and Performance for Optical/Infrared Ground-based Telescopes, ed. M. Iye & A. F. M. Moorwood, 944–952
Lindegren, L., Bastian, U., Biermann, M., et al. 2021a, A&A, 649, A4
Lindegren, L., Klioner, S. A., Hernández, J., et al. 2021b, A&A, 649, A2
Macintosh, B., Graham, J. R., Barman, T., et al. 2015, Science, 350, 64
Macintosh, B., Graham, J. R., Ingraham, P., et al. 2014, Proceedings of the National Academy of Science, 111, 12661
Maire, A.-L., Langlois, M., Dohlen, K., et al. 2016, in Ground-based and Airborne Instrumentation for Astronomy VI, Vol. 9908, 990834
Malmberg, D., Davies, M. B., & Heggie, D. C. 2011, MNRAS, 411, 859
Marois, C., Lafrenière, D., Doyon, R., Macintosh, B., & Nadeau, D. 2006, ApJ, 641, 556
Marois, C., Macintosh, B., Barman, T., et al. 2008, Science, 322, 1348
Marois, C., Zuckerman, B., Konopacky, Q. M., Macintosh, B., & Barman, T. 2010, Nature, 468, 1080
Mawet, D., David, T., Bottom, M., et al. 2015, ApJ, 811, 103
Mayor, M. & Mazeh, T. 1987, A&A, 171, 157
Milli, J., Hibon, P., Christiaens, V., et al. 2017, A&A, 597, L2
Moór, A., Pascucci, I., Kóspál, Á., et al. 2011, ApJS, 193, 4
Oliphant, T. E. 2006, A guide to NumPy, Vol. 1 (Trelgol Publishing USA)
Pawellek, N., Krivov, A. V., Marshall, J. P., et al. 2014, ApJ, 792, 65
Pecaut, M. J. & Mamajek, E. E. 2016, MNRAS, 461, 794
Pedregosa, F., Varoquaux, G., Gramfort, A., et al. 2012, arXiv e-prints, arXiv:1201.0490
Pollack, J. B., Hubickyj, O., Bodenheimer, P., et al. 1996, Icarus, 124, 62
Rafikov, R. R. 2005, ApJ, 621, L69
Raghavan, D., McAlister, H. A., Henry, T. J., et al. 2010, ApJS, 190, 1
Rameau, J., Chauvin, G., Lagrange, A. M., et al. 2013, The Astrophysical Journal, 772, L15
Raymond, S. N., Armitage, P. J., Moro-Martín, A., et al. 2012, A&A, 541, A11
Riaz, B., Gizis, J. E., & Harvin, J. 2006, AJ, 132, 866
Riello, M., De Angeli, F., Evans, D. W., et al. 2021, A&A, 649, A3
Rousset, G., Lacombe, F., Puget, P., et al. 2003, in Society of Photo-Optical Instrumentation Engineers (SPIE) Conference Series, Vol. 4839, Adaptive Optical System Technologies II, ed. P. L. Wizinowich & D. Bonaccini, 140–149
Schmidt, T. O. B., Neuhäuser, R., Seifahrt, A., et al. 2008, A&A, 491, 311
Skrutskie, M. F., Cutri, R. M., Stiening, R., et al. 2006, AJ, 131, 1163
Stolker, T., Bonse, M. J., Quanz, S. P., et al. 2019, A&A, 621, A59
Stolker, T., Marleau, G. D., Cugno, G., et al. 2020, A&A, 644, A13
Tokovinin, A., Mason, B. D., & Hartkopf, W. I. 2010, AJ, 139, 743
Tokovinin, A., Mason, B. D., Mendez, R. A., Horch, E. P., & Briceño, C. 2019, AJ, 158, 48
Torres, C. A. O., Quast, G. R., da Silva, L., et al. 2006, A&A, 460, 695
Van der Walt, S., Schönberger, J. L., Nunez-Iglesias, J., et al. 2014, PeerJ, 2, e453
Virtanen, P., Gommers, R., Oliphant, T. E., et al. 2020, Nature Methods, 17, 261
Wang, J., Fischer, D. A., Horch, E. P., & Xie, J.-W. 2015, ApJ, 806, 248
Wenger, M., Ochsenbein, F., Egret, D., et al. 2000, A&AS, 143, 9
Zhang, Z., Liu, M. C., Claytor, Z. R., et al. 2021, ApJ, 916, L11
Zhang, Z., Liu, M. C., Hermes, J. J., et al. 2020, ApJ, 891, 171

[1] Leiden Observatory, Leiden University, PO Box 9513, 2300 RA Leiden, The Netherlands
e-mail: ajbohn.astro@gmail.com
[2] Sterrenkundig Instituut Anton Pannekoek, Science Park 904, 1098 XH Amsterdam, The Netherlands
[3] Jet Propulsion Laboratory, California Institute of Technology, 4800 Oak Grove Drive, M/S 321-100, Pasadena CA 91109, USA
[4] Department of Physics & Astronomy, University of Rochester, Rochester NY 14627, USA
[5] IPAC, California Institute of Technology, M/C 100-22, 1200 East California Boulevard, Pasadena CA 91125, USA
[6] Rockhurst University, Department of Physics, 1100 Rockhurst Road, Kansas City MO 64110, USA
[7] Institute of Astronomy, KU Leuven, Celestijnenlaan 200D, B-3001 Leuven, Belgium
[8] ETH Zürich, Institute for Particle Physics and Astrophysics, Wolfgang-Pauli-Str. 27, 8093 Zürich, Switzerland
[9] Max-Planck-Institut für Astronomie, Königstuhl 17, 69117 Heidelberg, Germany
[10] Landessternwarte, Zentrum für Astronomie der Universität Heidelberg, Königstuhl 12, 69117 Heidelberg, Germany
[11] Observatoire Astronomique de l'Université de Genève, 51 Ch. des Maillettes, 1290 Versoix, Switzerland
[12] European Space Agency (ESA), ESA Office, Space Telescope Science Institute, 3700 San Martin Drive, Baltimore, MD 21218, USA

Appendix A: High-contrast imaging observations

We present the setup of our SPHERE and NACO observations and the atmospheric conditions during the data acquisition in Table A.1. The final images of our SPHERE and NACO data reductions on TYC 8252-533-1 are presented in Fig. A.1. In Fig. A.2 we show the remaining stellar companions to YSES targets as observed with SPHERE.

Appendix B: Identified companions

We present all identified candidate companions in Table B.1.

Appendix C: Posterior distribution of the MCMC analysis

In Fig. C.1 we present the posterior distribution of our MCMC-based SED fitting of TYC 8252-533-1 B. After discarding the burn-in phase and thinning the chains, the visualized 45,000 posterior samples remained. We additionally present the luminosities that are derived from the input parameters ($T_{\rm eff}$, $\log(g)$, R) as these quantity is used for the determination of the object's mass. We derived $T_{\rm eff} = 3092^{+186}_{-91}\,K$, $\log(g) = 3.41^{+1.07}_{-0.31}$ dex, $R = 3.5^{+0.3}_{-0.4}\,R_{\rm Jup}$, and $\log(L_*/L_\odot) = -1.99^{+0.01}_{-0.02}$ as the 95 % quantiles around the medians of the distributions.

Table A.1. High-contrast imaging observations of YSES targets.

Target (2MASS ID)	Observation date (yyyy-mm-dd)	Instrument	Mode[a]	Filter	NEXP×NDIT×DIT[b] (1×1×s)	$\Delta\pi$[c] (°)	$\langle X \rangle$[d]	$\langle \omega \rangle$[e] ($''$)	$\langle \tau_0 \rangle$[f] (ms)
12195938-5018404	2018-12-30	SPHERE	CI	H	4×1×32	0.4	1.6	0.5	8.0
12195938-5018404	2018-12-30	SPHERE	CI	K_s	4×1×32	0.4	1.6	0.6	9.0
12391404-5454469	2019-01-12	SPHERE	CI	H	4×1×32	0.5	1.4	1.0	4.3
12391404-5454469	2019-01-12	SPHERE	CI	K_s	4×1×32	0.5	1.4	0.9	4.2
12505143-5156353	2019-01-12	SPHERE	CI	H	4×1×32	0.5	1.3	1.1	3.8
12505143-5156353	2019-01-12	SPHERE	CI	K_s	4×1×32	0.5	1.3	1.0	4.1
12560830-6926539	2019-01-08	SPHERE	CI	H	4×1×32	0.5	1.5	1.2	2.2
12560830-6926539	2019-01-08	SPHERE	CI	K_s	4×1×32	0.5	1.5	1.1	2.0
13130714-4537438	2017-07-05	SPHERE	CI	J	4×2×32	0.3	1.8	0.7	4.1
13130714-4537438	2017-07-05	SPHERE	CI	H	4×1×32	0.8	1.8	0.7	3.7
13233587-4718467	2017-04-02	SPHERE	CI	H	4×1×32	0.7	1.2	1.7	1.4
13233587-4718467	2019-04-07	SPHERE	CI	K_s	60×2×32	40.5	1.1	0.5	8.9
13233587-4718467	2019-04-15	NACO	CI	L'	63×126×0.2	24.9	1.1	0.5	3.9
13233587-4718467	2020-02-19	SPHERE	DBI	$Y23$	4×2×32	2.6	1.1	0.8	5.6
13233587-4718467	2020-02-19	SPHERE	DBI	$J23$	4×2×32	2.5	1.1	0.8	5.3
13233587-4718467	2020-02-19	SPHERE	DBI	$H23$	4×2×32	2.4	1.1	0.6	6.8
13233587-4718467	2020-02-19	SPHERE	DBI	$K12$	4×2×32	2.3	1.1	0.6	6.5
13335481-6536414	2018-04-30	SPHERE	CI	H	4×2×32	1.4	1.3	0.5	8.4
13335481-6536414	2018-04-30	SPHERE	CI	K_s	4×2×32	1.4	1.3	0.5	8.0
13335481-6536414	2018-04-30	SPHERE	DPI	H	16×2×32	6.4	1.3	0.5	10.3

Notes. [a] The observation mode is either classical imaging (CI) with a broadband filter, dual-band imaging (DBI) with two intermediate band filters simultaneously, or dual-polarization imaging (DPI) with orthogonal linear polarization filters in the optical path. [b] NEXP describes the number of exposures, NDIT is the number of subintegrations per exposure and DIT is the detector integration time of an individual subintegration. [c] $\Delta\pi$ describes the amount of field rotation during the observation, if it is carried out in pupil-stabilized mode (only valid for CI observations). [d] $\langle X \rangle$ denotes the average airmass during the observation. [e] $\langle \omega \rangle$ denotes the average seeing conditions during the observation. [f] $\langle \tau_0 \rangle$ denotes the average coherence time during the observation.

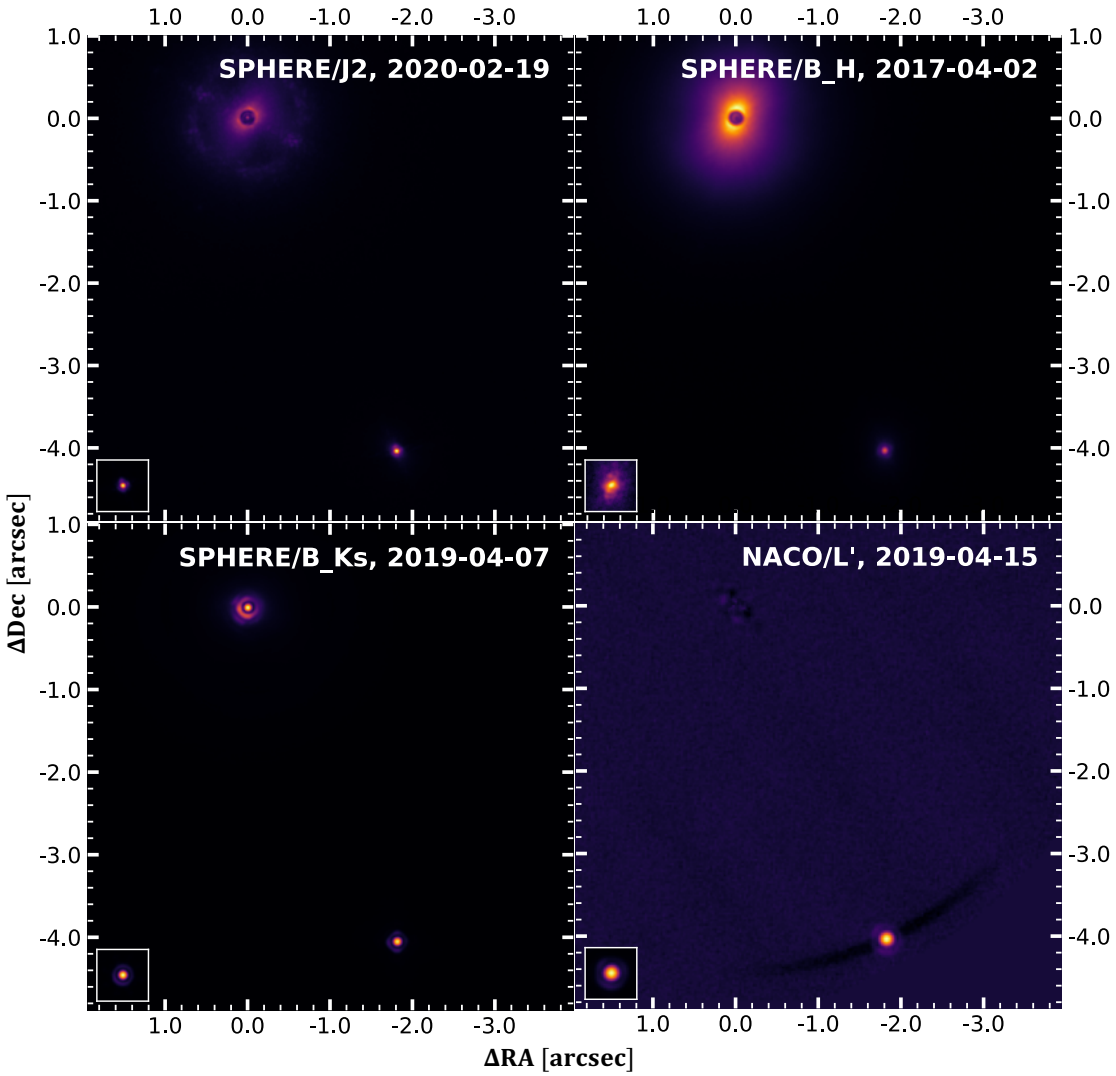

Fig. A.1. Reduced SPHERE and NACO data of TYC 8252-533-1 and its brown dwarf companion. For each of the presented filters we show the median of the full observing sequence. The images are derotated such that North points up and East towards the left. No PSF subtraction is applied for the SPHERE data – the star's intensity is attenuated by a coronagraphic mask, and it is located at the origin of the coordinate system that is representing the differential offsets in RA and Dec. No coronagraph was used for the NACO observing sequence and the stellar PSF is removed by classical ADI (Marois et al. 2006) to obtain the presented image; we did not perform any PSF subtraction for the extraction of the companion's photometry and astrometry. The companion is detected at a separation of $\sim 4\farcs4$ in south-western direction from the primary. In the lower left of each panel we present the non-coronagraphic stellar PSF as a reference. The images are shown with an arbitrary logarithmic color scale.

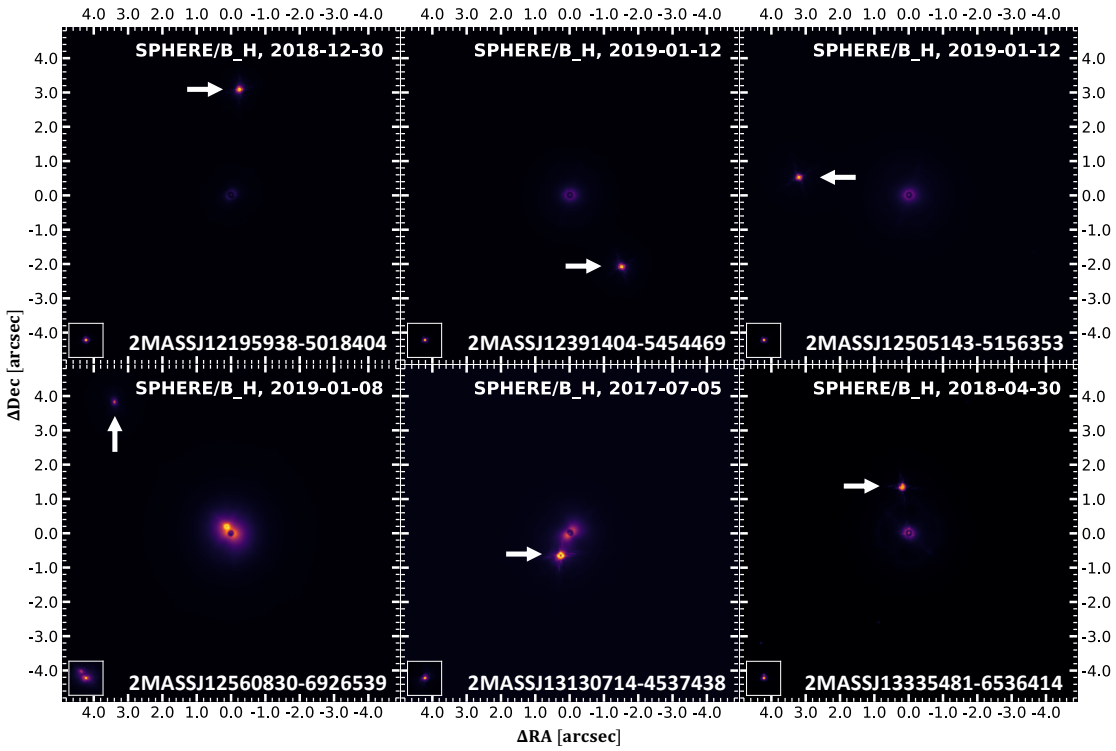

Fig. A.2. (Sub-)stellar companions identified in SPHERE data. We present the de-rotated and median combined coronagraphic images for the epochs and filters as indicated in the upper right of each panel. The star is located behind the coronagraphic mask at the center of each panel. The companions that were also identified by our *Gaia* selection algorithm are highlighted by the white arrows. As discussed in Sect. 4.2.4 there is an additional, very close companion to 2MASS J12560830-6926539. With a separation of merely 0.″2 this stellar companion is not identified by our *Gaia* selection method. In the lower left of each panel we present the non-coronagraphic flux PSFs of each target. In all frames north points up and east towards the left.

Table B.1. Identifiers and properties of all identified candidate companions to K type Sco-Cen members from Pecaut & Mamajek (2016).

Target					Companion									
2MASS ID	*Gaia* EDR3 ID	ϖ (mas)	Age (Myr)	Mass ($M_\odot$)	*Gaia* EDR3 ID	ρ ($''$)	ρ (au)	$\Delta\mu_{\alpha*}$ (mas yr^{-1})	$\Delta\mu_\delta$ (mas yr^{-1})	G (mag)	$G_{BP}-G_{RP}$ (mag)	Mass (M_{Jup})	v_{proj}/v_{max}	p^C (%)
10313710-6901587	5232514298297802880	5.97	21	0.9	5232514298301348864	10.3	1725	-0.18 ± 0.43	-0.20 ± 0.35	19.87	2.50	36.5 ± 2.4	$0.42^{+0.26}_{-0.21}$	98.23
10552886-6629147	5238609720201102080	7.57	15	1.1	5238609720201092736	20.8	2740	-2.29 ± 0.05	2.46 ± 0.05	16.40	3.03	120.2 ± 9.0	$2.37^{+0.04}_{-0.04}$	0.00
11175186-6402056	5240643988513310592	7.20	11	1.2	5240643988513309952	49.6	6899	-0.05 ± 0.03	-0.60 ± 0.02	7.84	0.22	1841.2 ± 54.6	$0.45^{+0.02}_{-0.02}$	99.75
11272881-3952572	5383924166203787648	7.52	6	1.2	5383924166203787904	23.0	3061	-0.69 ± 0.20	-3.20 ± 0.18	7.32	0.09	1985.8 ± 69.7	$1.55^{+0.08}_{-0.09}$	0.00
11515049-6407278	5332922112460126976	6.70	24	1.0	5332922116810986880	1.6	243	0.19 ± 0.17	-3.77 ± 0.16	16.63	-	152.7 ± 4.9	$0.92^{+0.04}_{-0.04}$	96.95
11554295-5637314	5343603288120259072	9.94	2	0.5	5343603180734334592	68.2	6865	-1.24 ± 0.03	2.07 ± 0.03	11.53	1.68	509.6 ± 129.9	$2.28^{+0.03}_{-0.03}$	0.00
11554295-5637314	5343603288120259072	9.94	2	0.5	5343603288130858112	0.8	84	-0.55 ± 0.23	3.18 ± 0.25	12.98	-	265.2 ± 77.3	$0.39^{+0.03}_{-0.03}$	100.00
12051254-5331233	6124952431621117056	8.67	17	0.9	6124952431621118848	7.4	853	0.54 ± 0.04	0.68 ± 0.05	16.47	3.46	100.6 ± 7.2	$0.33^{+0.02}_{-0.02}$	100.00
12074236-6227282	6057456092878899072	8.98	3	1.2	6057456092897714816	1.6	181	1.06 ± 0.06	2.19 ± 0.06	13.23	-	306.5 ± 89.6	$0.34^{+0.01}_{-0.01}$	100.00
12094184-5854450	6071087597518919040	9.50	6	1.3	6071087597497876480	12.8	1352	0.05 ± 0.09	-1.14 ± 0.16	15.89	-	76.0 ± 16.7	$0.43^{+0.06}_{-0.06}$	100.00
12094184-5854450	6071087597518919040	9.50	6	1.3	6071087597518919808	3.5	365	-2.99 ± 0.06	-2.29 ± 0.05	13.10	2.20	395.5 ± 47.3	$0.66^{+0.01}_{-0.01}$	99.75
12101065-4855476	6129878999619301120	9.72	12	1.0	6129879755533544832	14.1	1448	-1.40 ± 0.21	-0.50 ± 0.20	13.55	2.42	388.1 ± 26.9	$0.56^{+0.08}_{-0.08}$	100.00
12120804-6554549	5860803662284763392	9.21	14	1.0	5860803696599969280	31.6	3435	-0.19 ± 0.07	0.26 ± 0.07	16.97	3.47	66.2 ± 4.5	$0.23^{+0.05}_{-0.05}$	99.50
12121119-4950081	6129584364863667840	7.82	17	1.0	6129584364863668096	6.4	824	-0.83 ± 0.03	0.40 ± 0.03	14.92	2.80	270.4 ± 12.8	$0.34^{+0.01}_{-0.01}$	100.00
12123577-5520273	6075815841096386816	8.91	7	1.2	6075816592695096576	27.3	3060	-0.31 ± 0.03	-1.23 ± 0.03	12.57	2.14	558.1 ± 55.9	$0.67^{+0.02}_{-0.02}$	99.50
12123577-5520273	6075815841096386816	8.91	7	1.2	6075816596995760640	24.7	2772	2.04 ± 0.09	-0.90 ± 0.08	15.47	3.07	126.5 ± 20.9	$1.29^{+0.05}_{-0.05}$	0.00
12143410-5110124	6126585034583698944	8.45	14	1.1	6126585034581064192	21.2	2505	-0.48 ± 0.02	-1.08 ± 0.02	12.23	1.82	794.3 ± 17.4	$0.58^{+0.01}_{-0.01}$	100.00
12145229-5547037	6075548419252913152	8.78	10	1.4	6075548419252906368	24.0	2731	0.55 ± 0.02	-0.24 ± 0.02	8.33	0.64	1536.8 ± 82.2	$0.24^{+0.01}_{-0.01}$	100.00
12164023-7007361	5855198832989286400	8.96	8	1.1	5855198828676205696	3.2	358	0.29 ± 0.08	-0.73 ± 0.08	13.78	2.36	336.1 ± 30.8	$0.16^{+0.02}_{-0.02}$	100.00
12174048-5000266	6126715464151137792	7.17	14	0.7	6126715464149955968	10.8	1509	-0.86 ± 0.11	2.02 ± 0.10	14.29	2.78	389.5 ± 23.1	$1.29^{+0.06}_{-0.06}$	0.01
12195938-5018404	6126648698878768384	6.56	10	0.9	6126648703176939392	3.1	468	-0.23 ± 0.02	-0.03 ± 0.02	13.93	2.24	464.7 ± 29.3	$0.08^{+0.01}_{-0.01}$	100.00
12210808-5212226	6077461328965244160	9.09	8	1.0	6077461328965240576	21.8	2400	-0.43 ± 0.04	0.48 ± 0.04	15.78	3.61	104.1 ± 16.4	$0.37^{+0.02}_{-0.02}$	100.00
12220430-4841248	6127110188823860480	7.13	5	1.3	6127110188823860864	8.3	1165	-1.02 ± 0.05	-0.73 ± 0.04	15.72	3.29	124.8 ± 34.7	$0.57^{+0.02}_{-0.02}$	99.75
12302957-5222269	6078760195785278208	8.66	17	1.0	6078760195785506048	9.2	1061	1.07 ± 0.03	1.04 ± 0.03	13.35	2.75	538.6 ± 26.5	$0.51^{+0.01}_{-0.01}$	100.00
12333381-5714066	6073105991611649024	9.82	18	1.0	6073106193460538240	13.4	1368	-1.22 ± 0.10	0.85 ± 0.13	17.93	4.17	46.5 ± 3.3	$0.62^{+0.05}_{-0.05}$	100.00
12365895-5412178	6074563978391541888	8.66	5	1.3	6074563978391541504	20.7	2394	0.11 ± 0.01	0.04 ± 0.02	12.99	2.20	423.5 ± 61.7	$0.06^{+0.01}_{-0.01}$	100.00
12373737-5143113	6078883925202611968	8.83	5	0.7	6078885402671365504	34.6	3918	-5.43 ± 0.10	2.32 ± 0.08	15.13	3.13	136.1 ± 38.8	$5.18^{+0.08}_{-0.08}$	0.00
12391404-5454469	6074374346993398144	9.31	4	0.8	6074374346993397760	2.6	275	-1.16 ± 0.10	1.89 ± 0.11	14.30	2.46	189.1 ± 41.9	$0.45^{+0.02}_{-0.02}$	100.00
12404664-5211046	6078074169253752064	6.88	14	1.1	6078074237969848960	4.8	693	-0.74 ± 0.08	-1.02 ± 0.07	15.03	2.75	277.2 ± 15.9	$0.46^{+0.03}_{-0.03}$	100.00
12405458-5031550	6079389185156706944	11.30	17	0.8	6079389253876183808	14.1	1249	0.02 ± 0.03	0.45 ± 0.03	14.43	2.88	226.9 ± 13.2	$0.16^{+0.01}_{-0.01}$	100.00
12420050-5759486	6060864815105080064	8.65	3	0.5	6060864819427739904	1.3	152	-2.80 ± 0.28	-1.09 ± 0.51	13.64	-	263.1 ± 72.9	$0.56^{+0.06}_{-0.06}$	100.00
12443482-6331463	5862876928853591040	8.95	7	1.2	5862876928853590144	7.9	879	1.21 ± 0.09	1.10 ± 0.11	15.24	3.23	146.0 ± 21.2	$0.53^{+0.03}_{-0.03}$	100.00
12454884-5410583	6074796250199371648	9.05	18	1.0	6074796245904371968	18.8	2074	-0.38 ± 0.02	-0.53 ± 0.02	13.61	2.48	465.6 ± 23.8	$0.31^{+0.01}_{-0.01}$	100.00
12474824-5431308	6073980172067600640	8.47	1	0.5	6073980172067600000	2.6	311	-6.05 ± 0.13	2.86 ± 0.13	14.08	2.76	141.9 ± 38.9	$1.97^{+0.04}_{-0.04}$	0.00
12474824-5431308	6073980172067600640	8.47	1	0.5	6073980240787079680	16.1	1904	-4.89 ± 0.13	-0.03 ± 0.13	14.05	3.21	144.2 ± 40.0	$3.55^{+0.09}_{-0.10}$	0.00
12484818-5635378	6061376298490107520	7.73	18	1.2	6061376298480880512	2.8	367	-0.87 ± 0.07	0.69 ± 0.11	16.07	1.58	156.2 ± 8.4	$0.27^{+0.02}_{-0.02}$	100.00
12504491-5654485	6061310052916532096	9.25	1	0.4	6061310052892185088	1.7	187	-3.02 ± 0.06	-2.46 ± 0.07	12.48	2.20	273.1 ± 73.9	$0.80^{+0.01}_{-0.01}$	100.00
12505143-5156353	6075310478057303936	9.18	6	0.9	6075310478050174592	3.2	352	-0.11 ± 0.03	-0.70 ± 0.03	14.64	2.78	184.0 ± 21.6	$0.16^{+0.01}_{-0.01}$	100.00

Notes. With ϖ we denote the parallax of the target from our sample, ρ denotes the projected separation between the identified companion and our primary target, and $\Delta\mu_{\alpha*}$ and $\Delta\mu_\delta$ refer to the RA and Dec differences in proper motion between them. The ratio of v_{proj} and v_{max} is calculated as described in equation (6) (we present the 68% confidence interval around the median of the posterior distribution) and p^c is the upper limit we derive for the probability that the system is indeed gravitationally bound. All astrometric and photometric measurements are adopted or derived from *Gaia* EDR3 data products (Gaia Collaboration et al. 2021). With one exception, the age and mass estimates for the sources are adopted from Pecaut & Mamajek (2016) and we assume that the age of the primary is also valid for the identified companion. The age of the SZ 65 (2MASS J15392776-3446171, Gaia EDR3 6013399894569703040) system is based on Lupus membership (Comerón 2008; Alcalá et al. 2014) and the mass estimate is taken from Alcalá et al. (2017). The masses are calculated with BT-Settl isochrones (Allard et al. 2012; Baraffe et al. 2015).

Table B.1. (continued).

Target					Companion									
2MASS ID	*Gaia* EDR3 ID	ϖ (mas)	Age (Myr)	Mass ($M_\odot$)	*Gaia* EDR3 ID	ρ ($''$)	ρ (au)	$\Delta\mu_{\alpha*}$ (mas yr^{-1})	$\Delta\mu_\delta$ (mas yr^{-1})	G (mag)	$G_{BP}-G_{RP}$ (mag)	Mass (M_{Jup})	v_{proj}/v_{max}	p^C (%)
12560830-6926539	5844909156504879360	10.07	3	0.7	5844909156504880128	5.1	503	-4.46 ± 0.20	-1.41 ± 0.23	16.17	3.41	44.5 ± 5.8	$1.36^{+0.06}_{-0.06}$	0.00
13064012-5159386	6080364825623490688	8.75	10	1.2	6080364791268622336	8.1	929	0.19 ± 0.02	0.55 ± 0.02	14.23	2.67	295.2 ± 17.4	$0.19^{+0.01}_{-0.01}$	100.00
13071310-5952108	6056115131031531264	8.60	3	1.2	6056115135337482496	1.9	221	-0.56 ± 0.10	3.67 ± 0.12	13.91	-	229.4 ± 65.0	$0.61^{+0.02}_{-0.02}$	99.75
13071310-5952108	6056115131031531264	8.60	3	1.2	6056115169731484288	13.7	1597	1.56 ± 0.09	3.81 ± 0.12	15.46	3.39	72.6 ± 24.0	$1.91^{+0.05}_{-0.05}$	0.00
13121859-5439054	6067650970822131584	7.81	26	1.0	6067650970822132224	12.5	1602	-0.50 ± 0.02	-1.29 ± 0.02	10.20	0.92	1054.4 ± 14.4	$0.56^{+0.01}_{-0.01}$	99.25
13130714-4537438	6088027047281877120	7.18	2	0.8	6088027051573430400	0.7	98	1.36 ± 0.35	-0.22 ± 0.12	12.70	-	414.4 ± 114.2	$0.20^{+0.05}_{-0.05}$	100.00
13142382-5054018	6080820298315369088	7.19	8	1.5	6080820302618880896	9.8	1369	1.42 ± 0.08	1.97 ± 0.05	16.93	3.31	70.1 ± 11.3	$1.13^{+0.03}_{-0.03}$	0.00
13175314-5058481	6080854078239398016	6.36	3	0.8	6080854073939694592	33.3	5230	0.54 ± 0.23	-0.22 ± 0.13	18.59	3.17	27.1 ± 4.3	$0.84^{+0.31}_{-0.29}$	69.87
13233587-4718467	6083750638577673088	7.74	5	1.2	6083750638540951552	4.4	570	1.20 ± 0.16	-0.42 ± 0.13	16.74	2.91	48.7 ± 11.1	$0.40^{+0.05}_{-0.05}$	100.00
13270594-4856180	6082617587508723200	10.32	5	1.2	6082617591804976512	5.8	561	-0.22 ± 0.03	-3.41 ± 0.03	13.50	2.58	277.5 ± 41.8	$0.73^{+0.01}_{-0.01}$	100.00
13335329-6536473	5863747467220735744	9.94	3	0.6	5863747462890662144	12.0	1204	2.64 ± 0.39	2.69 ± 0.10	14.60	-	106.9 ± 37.7	$1.77^{+0.14}_{-0.13}$	0.00
13335329-6536473	5863747467220735744	9.94	3	0.6	5863747467220738432	11.1	1114	1.19 ± 0.06	3.59 ± 0.07	10.74	1.51	814.2 ± 204.7	$1.22^{+0.02}_{-0.02}$	0.00
13335481-6536414	5863747467220738432	9.75	2	0.8	5863747462890662144	1.3	137	1.45 ± 0.39	-0.90 ± 0.08	14.60	-	91.9 ± 31.0	$0.25^{+0.05}_{-0.05}$	99.75
13335481-6536414	5863747467220738432	9.75	2	0.8	5863747467220735744	11.1	1135	-1.19 ± 0.06	-3.59 ± 0.07	11.79	2.01	463.5 ± 118.3	$1.32^{+0.02}_{-0.02}$	0.00
13364090-4043359	6113000942074857216	8.49	8	0.8	6113000946373209216	4.6	538	-1.18 ± 0.03	-0.79 ± 0.02	14.19	2.67	289.2 ± 26.3	$0.42^{+0.01}_{-0.01}$	100.00
13442441-4706343	6106992866945163904	7.14	4	1.3	6106992866948449792	7.8	1097	-2.38 ± 0.09	0.10 ± 0.07	13.82	2.77	324.1 ± 67.2	$0.98^{+0.04}_{-0.04}$	69.80
13454424-4904500	6094572753539758976	7.42	5	1.3	6094572719180018432	24.1	3245	0.41 ± 0.15	-0.73 ± 0.13	9.10	0.59	1737.8 ± 90.8	$0.43^{+0.07}_{-0.07}$	99.75
13475054-4902056	6094529696485204864	7.17	23	1.0	6094529696485204736	19.0	2651	0.36 ± 0.07	0.89 ± 0.06	11.80	1.37	> 1250	$0.56^{+0.04}_{-0.03}$	100.00
13540743-6733449	5850443307764629376	7.44	18	1.1	5850443303440130816	28.0	3763	0.95 ± 0.01	-0.40 ± 0.02	12.40	1.55	842.3 ± 10.4	$0.69^{+0.01}_{-0.01}$	99.75
13540743-6733449	5850443307764629376	7.44	18	1.1	5850443303446183040	28.7	3861	1.27 ± 0.02	0.36 ± 0.02	13.66	2.08	555.1 ± 26.7	$0.97^{+0.01}_{-0.01}$	98.96
13552552-4706563	6095161370216796928	8.30	4	1.0	6095162843384927744	23.4	2824	0.46 ± 0.07	0.18 ± 0.05	15.10	3.22	137.2 ± 40.0	$0.34^{+0.04}_{-0.05}$	100.00
13562964-3839129	6114536929757358592	8.68	7	1.1	6114536929755100544	1.0	117	-0.57 ± 0.04	4.52 ± 0.05	11.97	-	735.9 ± 70.3	$0.48^{+0.00}_{-0.01}$	100.00
14004970-4236569	6109646679996671360	7.46	20	1.0	6109646679996673024	11.0	1468	0.85 ± 0.03	0.63 ± 0.04	13.23	2.15	680.8 ± 15.6	$0.47^{+0.01}_{-0.01}$	100.00
14213051-3845252	6116680904413813504	7.07	3	0.7	6116680908709624448	1.1	152	-0.82 ± 0.31	2.34 ± 0.30	12.41	1.63	556.6 ± 154.3	$0.44^{+0.05}_{-0.05}$	100.00
14270556-4714217	6092201450556437632	8.37	19	1.1	6092201450556434944	19.1	2285	0.34 ± 0.07	-0.40 ± 0.07	15.99	3.69	152.8 ± 7.4	$0.30^{+0.04}_{-0.04}$	100.00
14375022-5457411	5894194318558985984	8.62	17	1.1	5894194348576228992	59.7	6923	0.38 ± 0.02	0.37 ± 0.02	12.40	1.91	769.2 ± 17.4	$0.43^{+0.01}_{-0.01}$	99.75
14380350-4932023	5899359721077048064	7.80	6	1.0	5899359514918611456	32.0	4103	-2.15 ± 0.16	-1.20 ± 0.16	15.79	3.57	112.4 ± 28.0	$2.17^{+0.14}_{-0.13}$	0.00
14385440-4310223	6099803508307589632	7.64	3	1.2	6099826976008902016	30.2	3955	-0.16 ± 0.17	3.26 ± 0.16	15.05	3.14	120.9 ± 42.5	$2.64^{+0.13}_{-0.13}$	0.00
14413499-4700288	5905886387736675840	8.80	16	1.2	5905886215936891008	46.5	5286	0.33 ± 0.05	-0.57 ± 0.05	15.10	3.02	205.0 ± 8.8	$0.52^{+0.03}_{-0.04}$	99.75
14421590-4100183	6101758336902846208	8.47	15	1.0	6101758332601667712	4.4	521	1.53 ± 0.03	0.22 ± 0.03	11.84	1.56	883.5 ± 7.2	$0.35^{+0.01}_{-0.01}$	100.00
14584573-3315102	6204234706098895104	5.77	52	0.8	6204234706096290688	2.8	489	-1.61 ± 0.02	-1.49 ± 0.02	11.87	1.09	917.1 ± 5.1	$0.73^{+0.01}_{-0.01}$	100.00
14594473-3425465	6203845650778424960	8.66	7	1.1	6203845655074564864	0.9	104	4.57 ± 0.07	2.52 ± 0.08	11.53	1.33	871.5 ± 68.6	$0.50^{+0.01}_{-0.01}$	100.00
15022600-3405131	6203959484592343936	6.63	8	1.0	6203959488887357824	1.8	264	-0.46 ± 0.13	0.13 ± 0.11	15.00	-	248.7 ± 26.0	$0.12^{+0.03}_{-0.03}$	100.00
15085472-4303136	6003698907782693248	7.44	9	1.1	6003698873422956928	37.3	5011	-0.48 ± 0.03	-0.06 ± 0.02	9.40	0.65	1477.9 ± 71.4	$0.33^{+0.02}_{-0.02}$	99.00
15110450-3251304	6201456107071825536	7.24	3	0.7	6201456107071825792	4.5	626	1.73 ± 0.04	-1.24 ± 0.03	13.64	2.30	313.2 ± 92.5	$0.83^{+0.01}_{-0.01}$	100.00
15113968-3248560	6207460471351260160	7.05	1	0.4	6207460436991521280	48.6	6898	5.76 ± 0.08	-0.23 ± 0.06	12.94	2.35	294.4 ± 75.3	$9.25^{+0.12}_{-0.12}$	0.00
15113968-3248560	6207460471351260160	7.05	1	0.4	6207460471351260928	20.6	2920	-0.70 ± 0.11	-0.96 ± 0.08	16.92	3.35	39.8 ± 2.8	$1.55^{+0.12}_{-0.12}$	0.00
15124447-3116482	6210702308369949952	7.07	9	1.2	6210702415745896192	24.9	3513	-0.73 ± 0.03	-1.02 ± 0.03	13.98	2.45	404.6 ± 29.1	$0.94^{+0.02}_{-0.02}$	99.17
15135817-4629145	5903894175757504128	7.25	3	0.7	5903894175757506176	12.8	1762	0.16 ± 0.03	0.66 ± 0.02	13.32	2.15	365.2 ± 106.8	$0.43^{+0.01}_{-0.01}$	100.00
15152295-5441088	5886747291936159104	7.27	8	1.0	5886747291923626240	1.5	203	-3.22 ± 0.03	2.14 ± 0.04	13.32	-	509.4 ± 45.0	$0.70^{+0.01}_{-0.01}$	100.00
15171083-3434194	6200310519037175040	7.70	8	1.1	6200310484677437184	48.9	6351	-0.16 ± 0.04	-0.58 ± 0.03	12.92	2.02	576.3 ± 52.1	$0.55^{+0.03}_{-0.03}$	98.50
15171083-3434194	6200310519037175040	7.70	8	1.1	6200310514738629504	17.9	2330	-1.14 ± 0.04	-1.86 ± 0.03	7.97	0.23	1729.7 ± 58.5	$0.93^{+0.01}_{-0.01}$	98.75
15180123-4444269	6000349589207590016	8.30	44	0.8	6000349657912636928	2.4	288	0.59 ± 0.10	2.31 ± 0.09	15.68	1.91	238.3 ± 5.5	$0.54^{+0.02}_{-0.02}$	100.00
15182692-3738021	6007167351565715840	7.63	11	1.3	6007167179767020160	73.2	9597	1.17 ± 0.05	-1.92 ± 0.04	13.45	2.27	508.4 ± 28.6	$2.43^{+0.05}_{-0.05}$	0.00

Table B.1. (continued).

Target					Companion									
2MASS ID	*Gaia* EDR3 ID	ϖ (mas)	Age (Myr)	Mass ($M_\odot$)	*Gaia* EDR3 ID	ρ ($''$)	ρ (au)	$\Delta\mu_{\alpha*}$ (mas yr^{-1})	$\Delta\mu_\delta$ (mas yr^{-1})	G (mag)	$G_{BP}-G_{RP}$ (mag)	Mass (M_{Jup})	v_{proj}/v_{max}	p^C (%)
15185282-4050528	6004336074769756800	6.72	10	1.3	6004347825798261632	10.7	1592	-0.56 ± 0.06	-2.55 ± 0.05	14.39	2.64	365.0 ± 22.8	$1.36^{+0.03}_{-0.03}$	0.00
15191600-4056075	6004331775495542656	7.68	25	1.0	6004331779800414464	3.9	503	-0.82 ± 0.10	0.00 ± 0.11	16.42	2.70	148.0 ± 5.0	$0.25^{+0.03}_{-0.03}$	100.00
15215241-2842383	6213042069112745856	7.97	10	1.1	6213042073410590464	1.6	195	-2.08 ± 0.15	-2.12 ± 0.10	14.84	-	234.3 ± 18.0	$0.51^{+0.02}_{-0.02}$	100.00
15241147-3030582	6208136391829015936	7.71	18	1.1	6208136396122878976	17.4	2261	-0.10 ± 0.06	0.71 ± 0.04	15.21	2.96	239.7 ± 12.9	$0.43^{+0.02}_{-0.02}$	99.75
15241147-3030582	6208136391829015936	7.71	18	1.1	6208136396126956928	20.3	2625	0.02 ± 0.03	-0.50 ± 0.02	12.88	2.01	723.8 ± 21.0	$0.28^{+0.01}_{-0.01}$	100.00
15241303-3030572	6208136396126956928	7.65	1	0.4	6208136391829015936	20.3	2648	-0.02 ± 0.03	0.50 ± 0.02	10.59	1.11	745.8 ± 175.0	$0.36^{+0.01}_{-0.01}$	100.00
15241303-3030572	6208136396126956928	7.65	1	0.4	6208136396122878976	3.5	453	-0.12 ± 0.06	1.21 ± 0.04	15.21	2.96	85.8 ± 8.5	$0.55^{+0.02}_{-0.02}$	99.75
15293858-3546513	6013649964744749184	8.57	7	1.4	6013649969039127552	2.6	307	-2.00 ± 0.13	-0.45 ± 0.12	15.64	2.54	118.4 ± 22.0	$0.38^{+0.02}_{-0.02}$	100.00
15294727-3628374	6013480055841212416	6.12	5	1.3	6013480060137095296	1.7	273	-2.09 ± 0.13	0.51 ± 0.10	16.27	-	103.6 ± 29.2	$0.55^{+0.03}_{-0.03}$	100.00
15295661-3135446	6208566369594256768	8.33	9	0.9	6208566373892571136	1.7	209	5.02 ± 0.25	0.41 ± 0.22	14.81	-	213.6 ± 17.1	$0.94^{+0.05}_{-0.05}$	91.30
15312961-3021537	6209492506280547200	6.48	2	0.5	6209492506275602816	1.2	189	-1.21 ± 0.18	2.96 ± 0.13	14.34	-	209.8 ± 60.9	$0.91^{+0.04}_{-0.04}$	98.52
15342313-3300087	6014539542668216832	7.84	2	0.5	6014539645747431680	43.9	5596	0.08 ± 0.06	-0.35 ± 0.04	15.16	3.36	87.5 ± 29.1	$0.51^{+0.06}_{-0.06}$	99.75
15370214-3136398	6208381582919629568	7.95	8	1.5	6208381587215253504	4.7	587	0.90 ± 0.06	0.49 ± 0.04	11.79	-	878.5 ± 53.4	$0.23^{+0.01}_{-0.01}$	99.75
15370214-3136398	6208381582919629568	7.95	8	1.5	6208381587220236160	5.9	742	-1.12 ± 0.16	-0.62 ± 0.12	11.87	2.60	856.1 ± 54.7	$0.33^{+0.04}_{-0.04}$	99.75
15392776-3446171	6013399894569703040	6.54	2	0.7	6013399830146943104	6.4	973	-0.09 ± 0.04	-0.31 ± 0.03	13.89	3.09	265.5 ± 77.7	$0.18^{+0.02}_{-0.02}$	100.00
15394637-3451027	6013398451460692992	6.53	2	0.9	6013351520350805632	1.1	170	-1.53 ± 0.12	-1.54 ± 0.07	13.94	-	260.0 ± 75.2	$0.46^{+0.02}_{-0.02}$	100.00
15410679-2656263	6234377340635038848	8.58	29	1.0	6234377718592160384	6.3	733	-0.20 ± 0.10	-1.77 ± 0.06	16.12	3.07	161.7 ± 4.5	$0.59^{+0.02}_{-0.02}$	100.00
15440376-3311110	6015107302986648064	6.41	6	1.3	6015107302990748032	1.3	210	-6.25 ± 0.31	3.07 ± 0.21	15.11	-	214.5 ± 34.2	$1.45^{+0.06}_{-0.06}$	0.00
15444712-3811406	6009518657190466560	7.72	2	0.6	6009518657176115840	3.3	427	-1.76 ± 0.09	-3.22 ± 0.06	13.63	2.32	253.2 ± 73.3	$1.21^{+0.02}_{-0.02}$	0.00
15451286-3417305	6014696841553696768	6.55	1	1.6	6014696841553696896	2.8	430	1.18 ± 0.23	-1.51 ± 0.16	14.74	-	135.1 ± 34.1	$0.52^{+0.05}_{-0.05}$	99.75
15451286-3417305	6014696841553696768	6.55	1	1.6	6014696875913435520	49.6	7570	0.96 ± 0.18	0.42 ± 0.11	17.55	4.02	30.8 ± 3.6	$1.24^{+0.20}_{-0.20}$	11.50
15462958-5217239	5885915442658792576	7.31	22	1.0	5885915442658792448	1.6	218	2.09 ± 0.10	-0.64 ± 0.06	14.74	-	355.0 ± 11.4	$0.43^{+0.02}_{-0.02}$	100.00
15481299-2349523	6239880671209818880	9.23	6	0.5	6239880671208969856	29.4	3184	1.09 ± 0.62	0.55 ± 0.36	14.53	2.81	193.5 ± 33.9	$1.08^{+0.46}_{-0.42}$	42.80
15514535-2456513	6236477064249469312	6.42	13	1.0	6236477064249562624	2.4	369	0.84 ± 0.26	1.64 ± 0.15	16.77	1.93	111.3 ± 9.1	$0.60^{+0.06}_{-0.05}$	100.00
15545141-3154463	6039427503765943936	7.10	2	0.7	6039427503765943040	6.3	883	0.95 ± 0.22	0.04 ± 0.17	17.57	3.08	33.8 ± 3.6	$0.53^{+0.11}_{-0.12}$	100.00
15582054-1837252	6248340348034690688	7.20	9	1.5	6248340343736161664	5.6	783	0.25 ± 0.17	0.77 ± 0.09	15.54	2.65	176.8 ± 14.9	$0.28^{+0.04}_{-0.04}$	100.00
15591101-1850442	6247571617610119808	6.49	3	0.7	6247571583249729280	14.6	2256	-0.07 ± 0.05	0.42 ± 0.03	13.32	2.71	403.3 ± 113.8	$0.34^{+0.03}_{-0.03}$	100.00
16011070-4804438	5984404849554176896	8.02	18	1.0	5984404849554176256	15.3	1904	-0.20 ± 0.10	-0.21 ± 0.08	17.29	3.64	73.8 ± 4.4	$0.18^{+0.05}_{-0.05}$	100.00
16023814-2541389	6235806323497438592	8.94	5	0.7	6235806259081172736	31.7	3546	-0.05 ± 0.03	-0.11 ± 0.02	11.62	1.49	738.5 ± 99.0	$0.08^{+0.01}_{-0.01}$	99.25
16023910-2542078	6235806259081172736	8.98	13	0.8	6235806323497438592	31.7	3529	0.05 ± 0.03	0.11 ± 0.02	12.36	1.81	716.8 ± 23.9	$0.08^{+0.01}_{-0.01}$	99.00
16025123-2401574	6236273895118889472	6.92	6	1.0	6236273895118890112	7.2	1043	0.58 ± 0.09	0.20 ± 0.05	16.35	3.80	87.5 ± 21.4	$0.31^{+0.04}_{-0.04}$	100.00
16032367-1751422	6249905743355599232	6.00	1	0.3	6249905743349542784	2.5	424	2.01 ± 0.34	-1.64 ± 0.25	15.11	2.90	123.1 ± 34.2	$1.56^{+0.18}_{-0.18}$	0.12
16042165-2130284	6243393817024157184	6.91	2	1.4	6243393817024156288	16.2	2346	0.19 ± 0.05	0.95 ± 0.03	13.59	2.80	288.6 ± 86.5	$0.59^{+0.02}_{-0.02}$	99.50
16062354-1814187	6249074718717359744	6.23	1	0.7	6249074718725644288	0.6	100	0.15 ± 0.34	0.59 ± 0.20	12.21	1.75	459.1 ± 132.7	$0.12^{+0.04}_{-0.03}$	100.00
16065436-2416107	6242013410230303488	6.73	1	0.3	6242013414531686272	1.7	246	-2.67 ± 0.08	-1.74 ± 0.05	13.59	-	208.2 ± 70.3	$1.19^{+0.03}_{-0.03}$	0.00
16065795-2743094	6042124910722287744	6.49	6	2.0	6042124807643059968	31.2	4812	-1.97 ± 0.17	-1.73 ± 0.10	17.93	4.04	34.9 ± 5.3	$2.21^{+0.12}_{-0.12}$	0.00
16065795-2743094	6042124910722287744	6.49	6	2.0	6042124915024285440	1.5	228	-3.02 ± 0.37	-0.10 ± 0.21	11.78	0.85	957.4 ± 83.6	$0.46^{+0.06}_{-0.06}$	100.00
16073366-3759242	5998266426996208384	7.32	10	0.8	5998266426996209408	3.6	486	-1.18 ± 0.04	1.00 ± 0.03	14.68	2.66	286.1 ± 17.5	$0.51^{+0.01}_{-0.01}$	100.00
16080772-5041556	5983063479721274880	10.14	10	0.8	5983063479721275520	6.2	608	-1.03 ± 0.03	1.45 ± 0.03	13.57	2.98	352.5 ± 21.7	$0.46^{+0.01}_{-0.01}$	100.00
16081824-3844052	5997477080726175744	7.81	6	0.7	5997477080724660992	8.3	1066	0.23 ± 0.15	2.83 ± 0.10	16.59	3.25	63.6 ± 14.8	$1.53^{+0.05}_{-0.05}$	0.00
16083436-1911563	6248755585472315392	8.38	1	0.7	6248755684252562432	27.6	3300	1.68 ± 0.51	-0.46 ± 0.34	16.99	3.83	31.1 ± 4.8	$1.60^{+0.44}_{-0.44}$	8.29
16084340-2602168	6043486660173351552	7.28	5	1.7	6043486655875354112	13.5	1855	0.13 ± 0.33	-0.23 ± 0.21	18.71	4.01	24.8 ± 1.0	$0.21^{+0.12}_{-0.10}$	100.00
16085427-3906057	5997035351934438784	6.41	3	1.4	5997035317574700544	62.6	9761	1.50 ± 0.10	0.40 ± 0.07	16.15	3.52	70.8 ± 21.4	$2.23^{+0.14}_{-0.14}$	0.00
16085427-3906057	5997035351934438784	6.41	3	1.4	5997035416337166976	48.4	7542	-0.94 ± 0.43	0.99 ± 0.32	19.30	2.53	21.3 ± 4.1	$1.81^{+0.47}_{-0.45}$	3.17

Table B.1. (continued).

Target					Companion									
2MASS ID	*Gaia* EDR3 ID	ϖ (mas)	Age (Myr)	Mass ($M_\odot$)	*Gaia* EDR3 ID	ρ ($''$)	ρ (au)	$\Delta\mu_{\alpha*}$ (mas yr^{-1})	$\Delta\mu_\delta$ (mas yr^{-1})	G (mag)	$G_{BP}-G_{RP}$ (mag)	Mass (M_{Jup})	v_{proj}/v_{max}	p^C (%)
16085673-2033460	6243922063636859008	7.08	2	0.8	6243922029277120128	49.2	6955	-0.09 ± 0.08	-2.47 ± 0.06	14.49	3.29	174.4 ± 47.6	$3.34^{+0.08}_{-0.07}$	0.00
16090075-1908526	6245777283349430912	7.30	4	0.6	6245777283349431552	19.0	2597	0.06 ± 0.07	-0.23 ± 0.04	15.42	3.39	133.0 ± 38.5	$0.23^{+0.04}_{-0.04}$	100.00
16101171-3226360	6035794030167079808	6.28	1	0.7	6035794030168507264	1.3	211	-0.51 ± 0.08	-0.01 ± 0.05	12.10	1.66	478.1 ± 117.9	$0.12^{+0.02}_{-0.02}$	100.00
16101729-1910263	6245762538722565888	6.43	1	0.7	6245762543021965184	5.6	870	-1.35 ± 0.20	-1.27 ± 0.13	14.10	2.92	180.6 ± 53.7	$1.03^{+0.09}_{-0.09}$	38.69
16101918-2502301	6049748791208799488	6.30	1	0.4	6049748786908497408	4.9	777	1.29 ± 0.11	-0.67 ± 0.08	15.66	3.15	84.3 ± 8.5	$1.05^{+0.08}_{-0.07}$	26.17
16102174-1904067	6245781097280740864	7.48	4	0.5	6245781131640479360	4.6	615	-0.45 ± 0.12	0.72 ± 0.10	16.94	4.08	43.1 ± 5.8	$0.44^{+0.05}_{-0.05}$	100.00
16102653-2756293	6042235793900264448	18.45	2	0.3	6042235725180784768	24.6	1333	-1.00 ± 0.03	1.65 ± 0.02	13.15	2.47	95.4 ± 32.3	$0.69^{+0.01}_{-0.01}$	100.00
16104202-2101319	6243833724749589632	7.14	1	0.7	6243833724749589760	3.2	448	0.21 ± 0.11	1.26 ± 0.08	15.51	3.25	78.9 ± 12.5	$0.49^{+0.03}_{-0.03}$	100.00
16111534-1757214	6249000566108106112	7.39	2	0.4	6249001841715440512	40.5	5477	-1.21 ± 0.12	-0.93 ± 0.08	13.67	3.09	259.9 ± 74.7	$2.14^{+0.15}_{-0.15}$	0.00
16114387-2526350	6049537165279381632	7.11	7	1.1	6049532737170518016	32.9	4618	2.26 ± 0.11	-0.25 ± 0.07	15.49	3.47	167.6 ± 20.0	$2.18^{+0.10}_{-0.10}$	0.00
16114387-2526350	6049537165279381632	7.11	7	1.1	6049537169580902272	46.9	6597	-3.88 ± 0.16	3.52 ± 0.10	16.40	4.32	88.5 ± 16.5	$6.18^{+0.16}_{-0.16}$	0.00
16123916-1859284	6245821092014031616	7.42	10	1.1	6245821126373768832	19.1	2578	-0.09 ± 0.03	-3.57 ± 0.02	10.40	1.57	1261.8 ± 35.1	$1.81^{+0.01}_{-0.01}$	0.00
16124051-1859282	6245821126373768832	7.47	1	2.0	6245821092014031616	19.1	2559	0.09 ± 0.03	3.57 ± 0.02	12.99	2.33	265.4 ± 72.1	$1.81^{+0.01}_{-0.01}$	0.00
16125265-2319560	6242176829446854656	6.60	9	1.1	6242176653347275136	38.3	5799	1.07 ± 0.04	-0.23 ± 0.03	9.06	0.99	1567.9 ± 87.1	$0.88^{+0.03}_{-0.03}$	98.24
16135801-3618133	6022499010422921088	8.02	28	1.0	6022499006128860928	5.7	716	1.22 ± 0.03	0.80 ± 0.02	13.34	2.23	652.7 ± 7.5	$0.43^{+0.01}_{-0.01}$	99.75
16135801-3618133	6022499010422921088	8.02	28	1.0	6022499010440068864	7.5	931	2.39 ± 0.09	1.25 ± 0.05	15.51	-	225.7 ± 9.2	$1.05^{+0.03}_{-0.03}$	6.44
16140035-2108439	6243089247998315264	6.96	7	0.7	6243089217937775360	45.8	6582	-0.30 ± 0.05	-0.39 ± 0.04	15.53	3.14	168.2 ± 19.0	$0.70^{+0.06}_{-0.06}$	99.25
16145207-5026187	5935099415271699072	8.36	4	1.5	5935099415267651328	2.2	261	-3.57 ± 0.05	0.55 ± 0.04	11.42	-	792.0 ± 137.5	$0.52^{+0.01}_{-0.01}$	100.00
16153456-2242421	6242598526515737728	7.25	2	0.8	6242598526515738112	1.9	264	1.64 ± 0.10	0.36 ± 0.05	13.25	-	320.5 ± 91.2	$0.40^{+0.02}_{-0.02}$	100.00
16161423-2643148	6042418858284146688	8.26	5	0.9	6042418828224074752	71.2	8627	1.05 ± 0.12	1.39 ± 0.07	14.24	2.94	242.2 ± 39.7	$2.08^{+0.11}_{-0.11}$	0.00
16161423-2643148	6042418858284146688	8.26	5	0.9	6042418862581174016	2.5	304	-0.54 ± 0.05	1.54 ± 0.03	12.64	1.94	519.0 ± 75.7	$0.33^{+0.01}_{-0.01}$	100.00
16175569-3828132	5997311359393377280	9.39	8	0.6	5997311363710561280	6.8	721	-2.11 ± 0.10	1.44 ± 0.06	16.88	3.19	50.7 ± 10.1	$1.02^{+0.03}_{-0.03}$	25.66
16183723-2405226	6050056478369804288	6.45	33	1.0	6050056482664014976	4.5	692	-1.59 ± 0.09	1.49 ± 0.07	11.47	1.28	919.0 ± 8.9	$0.73^{+0.03}_{-0.03}$	100.00
16191217-2550383	6048571072519663872	6.47	5	1.2	6048571076818643968	1.3	207	-0.57 ± 0.13	2.45 ± 0.09	16.12	-	107.0 ± 29.8	$0.55^{+0.02}_{-0.02}$	100.00
16204468-2431384	6049266036882633856	6.02	10	1.6	6049266002522895232	33.4	5547	-1.57 ± 0.10	3.24 ± 0.07	16.24	3.80	155.2 ± 11.6	$3.79^{+0.08}_{-0.07}$	0.00
16204468-2431384	6049266036882633856	6.02	10	1.6	6049266414839756416	42.9	7126	-3.20 ± 0.09	3.44 ± 0.07	16.28	3.64	152.3 ± 11.7	$5.61^{+0.09}_{-0.09}$	0.00
16235484-3312370	6024816025017339392	7.78	4	0.7	6024816020718366464	42.6	5473	0.81 ± 0.49	-1.72 ± 0.38	7.46	0.06	2185.5 ± 311.4	$1.25^{+0.26}_{-0.25}$	15.45
16235484-3312370	6024816025017339392	7.78	4	0.7	6024816059387932416	45.5	5849	1.44 ± 0.49	-1.62 ± 0.38	7.00	-0.02	2273.4 ± 318.0	$1.45^{+0.28}_{-0.28}$	4.85
16240289-2524539	6048929792484158208	5.78	5	2.6	6048929792479889920	2.1	356	-5.93 ± 0.14	4.84 ± 0.11	13.50	-	500.4 ± 79.8	$1.60^{+0.03}_{-0.03}$	0.00
16250991-3047572	6037691855943122176	7.76	14	1.3	6037691855943131520	40.9	5267	9.89 ± 0.20	-0.41 ± 0.17	14.61	2.84	301.2 ± 19.3	$8.27^{+0.17}_{-0.17}$	0.00
16263591-3314481	6024849594490361856	6.73	5	1.3	6024849594490360320	5.6	839	3.39 ± 0.03	2.88 ± 0.02	13.50	2.05	432.2 ± 63.2	$1.65^{+0.01}_{-0.01}$	0.00
16265280-2343127	6050875614529786752	7.25	3	1.6	6050875618822791936	30.0	4137	-4.47 ± 0.49	-1.13 ± 0.41	19.05	-	21.1 ± 4.1	$3.63^{+0.38}_{-0.37}$	0.00
16265700-3032232	6037784004457590528	9.16	9	0.8	6037784004457597568	10.6	1158	0.04 ± 0.03	-1.25 ± 0.02	12.58	2.12	592.3 ± 44.2	$0.45^{+0.01}_{-0.01}$	100.00
16265700-3032232	6037784004457590528	9.16	9	0.8	6037784008760031872	9.3	1013	1.65 ± 0.03	-1.29 ± 0.03	11.13	1.45	1001.3 ± 23.0	$0.62^{+0.01}_{-0.01}$	99.75
16265763-3032279	6037784008760031872	9.20	1	0.5	6037784004457590528	9.3	1009	-1.65 ± 0.03	1.29 ± 0.03	11.64	1.66	406.6 ± 101.5	$0.87^{+0.01}_{-0.01}$	100.00
16265763-3032279	6037784008760031872	9.20	1	0.5	6037784004457597568	3.6	391	-1.61 ± 0.03	0.04 ± 0.02	12.58	2.12	260.3 ± 71.7	$0.45^{+0.01}_{-0.01}$	99.75
16272794-4542403	5942410686571895424	5.46	7	1.5	5942410682235163648	24.5	4495	-0.92 ± 0.03	-3.75 ± 0.03	13.48	1.87	596.2 ± 61.7	$3.71^{+0.03}_{-0.02}$	0.00
16303796-2954222	6031823178275372800	8.71	11	1.1	6031823173966757120	5.0	569	3.18 ± 0.05	-0.68 ± 0.04	14.86	1.69	208.6 ± 12.0	$0.88^{+0.01}_{-0.01}$	100.00
16310436-2404330	6050627747672189312	7.37	1	0.9	6050627782031927296	13.1	1771	-2.34 ± 0.16	0.13 ± 0.12	13.02	2.33	266.6 ± 76.8	$1.40^{+0.10}_{-0.09}$	0.01
16320058-2530287	6045791575844270208	7.13	5	0.7	6045791953801392128	14.2	1998	-0.87 ± 0.02	-0.25 ± 0.02	12.66	1.81	591.3 ± 83.7	$0.57^{+0.01}_{-0.01}$	100.00
16320160-2530253	6045791953801392128	7.15	3	0.8	6045791575844270208	14.2	1994	0.87 ± 0.02	0.25 ± 0.02	12.47	1.72	537.2 ± 139.6	$0.55^{+0.01}_{-0.01}$	100.00
16345314-2518167	6047289699098449920	6.94	7	1.4	6047289699098450944	10.2	1465	-0.25 ± 0.13	0.86 ± 0.10	14.83	2.81	245.6 ± 33.7	$0.44^{+0.05}_{-0.05}$	99.75
16345314-2518167	6047289699098449920	6.94	7	1.4	6047289733458188032	44.4	6402	0.36 ± 0.14	1.57 ± 0.10	15.12	2.96	205.1 ± 25.0	$1.66^{+0.11}_{-0.11}$	0.00
16430140-4405275	5967552634824947456	5.19	16	1.2	5967552634824945152	10.8	2075	-0.29 ± 0.12	-0.43 ± 0.10	17.09	2.71	135.4 ± 8.9	$0.45^{+0.09}_{-0.09}$	100.00
16452615-2503169	6046749289143173504	6.93	1	1.1	6046749319188591104	48.1	6932	-0.04 ± 0.04	0.02 ± 0.03	14.39	2.90	150.5 ± 39.3	$0.07^{+0.04}_{-0.03}$	99.25
16473710-2014268	4130416623473262720	9.48	11	1.0	4130416726552477440	22.1	2335	0.40 ± 0.10	-0.68 ± 0.07	14.57	2.58	223.9 ± 14.7	$0.41^{+0.04}_{-0.04}$	100.00

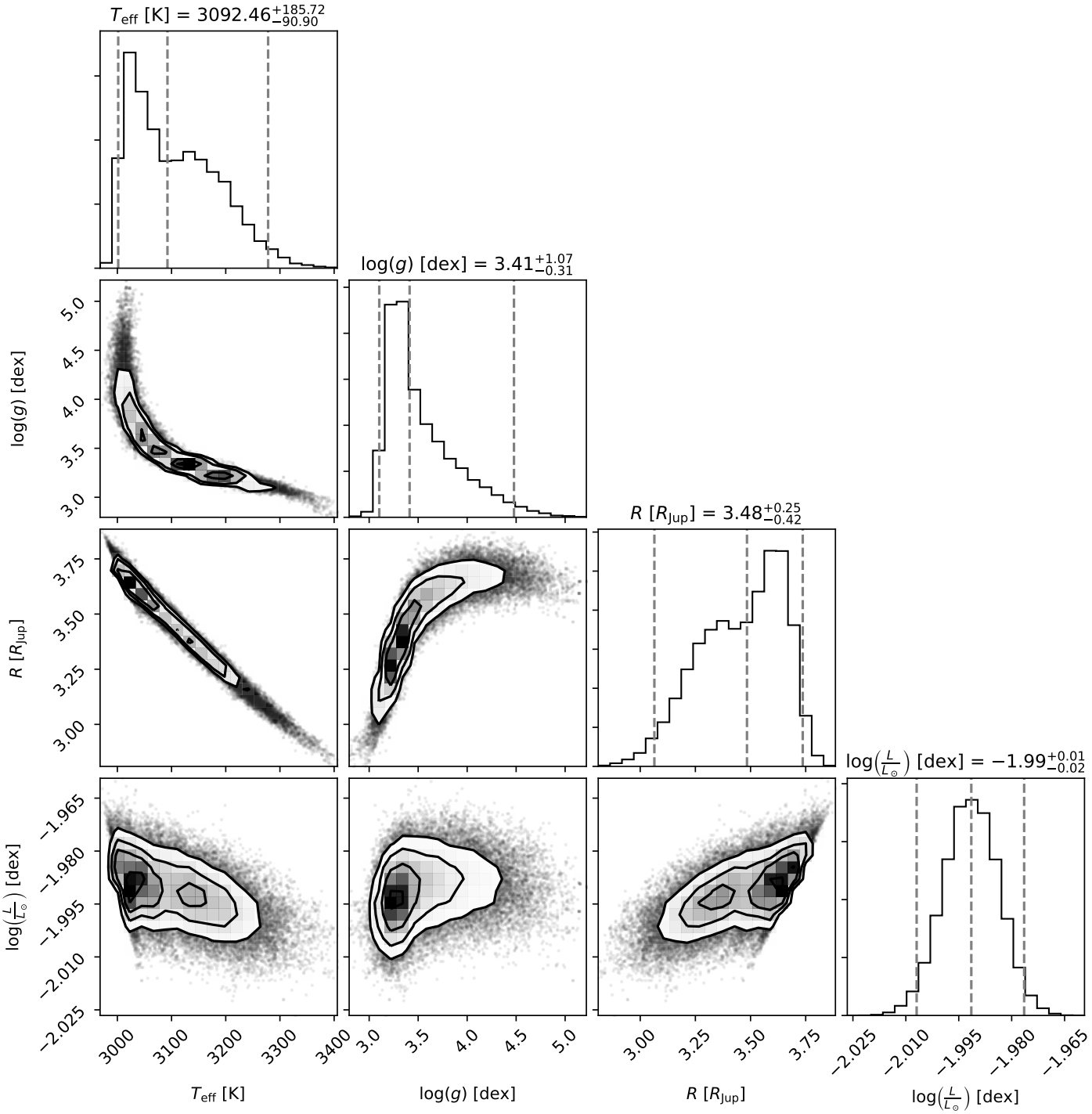

Fig. C.1. Posterior distribution of the MCMC-based fit to the SED of TYC 8252-533-1 B. The blue, dashed lines represent the 2.5th, 50th, and 97.5th percentiles of the marginalized distributions.